Numerical modeling of temperature and flow fields associated with subduction of oceanic plates in central Japan and Mexico - considerations on the relationship between…

末永，伸明

(Degree)
博士（理学）

(Date of Degree)
2016-03-25

(Date of Publication)
2017-03-01

(Resource Type)
doctoral thesis

(Report Number)
甲第6611号

(URL)
https://hdl.handle.net/20.500.14094/D1006611

博士論文

Numerical modeling of temperature and flow fields associated with subduction of oceanic plates in central Japan and Mexico - considerations on the relationship between calculated temperature fields and occurrences of interplate earthquakes

中部日本とメキシコにおけるプレートの沈み込みに伴う温度場・流れ場の数値モデリング ～プレート間地震との関連性の考察～

平成 28 年 1 月

神戸大学大学院理学研究科

末永　伸明

Contents

Abstract

In this study, to investigate generation mechanisms of megathrust earthquakes, low-frequency earthquakes (LFEs), non-volcanic tremors (NVTs), and slow slip events (SSEs), we performed numerical simulations of temperature and mantle flow associated with subduction of oceanic plates in central Japan and southern Mexico. The distribution of LFEs overlaps with that of NVTs in Japan. The origin of LFTs is considered to be related to the dehydration from the subducting plate, because the source of NVTs has mobility, and NVTs continue for long duration. P-waves and S-waves of NVTs are not well defined, and occasionally observed a distinguished seismic waveform called LFEs. So, LFEs is also considered to occur when hydrous minerals in an oceanic crust of the subducting plate takes place phase transformations and supplies water to the plate boundary because of concentration of hypocenters of LFEs at the plate boundary. Therefore, we estimated temperature distributions at the plate boundaries, and water contents dehydrated from hydrous minerals within the subducting plates in the two regions.

In part I, we constructed a 2-D box-type thermal convection model in the region covering from the eastern Kii Peninsula to the western Tokai district. Since National Research Institute for Earth Science and Disaster Prevention (NIED) has set up a dense High Sensitivity Seismograph Network Japan (Hi-net) for recent years, detectability toward earthquakes has developed dramatically, and it became possible to obtain detailed data about microearthquakes such as LFEs. LFEs occur in a belt-like form from the western part of Shikoku to the southern part of Nagano prefecture. However, a seismic gap of LFEs exists around Ise Bay, central Japan. There are no active volcanoes in these regions, because the oceanic Philippine Sea (PHS) plate is subducting at a low angle, and the subducting plate does not reach the depth of about 110 km, where partial melting of the slab is considered to take place. So, the LFTs there is not considered to be volcanic origin. In this study, we set up three profiles passing through the eastern part of the Kii Peninsula and the Lake Hamana, where many LFEs occur, and around Ise Bay, where there is a seismic gap of LFEs. In our model,, we considered frictional heating on the surface of subducting plate and effect of a temperature variation due to uplift and subsidence rate of the crust during the Quaternary period in the energy equation. We also adopted complex subduction history of the PHS plate in our model, referring to the recent researches to assign realistic spatiotemporal changing temperature boundary condition. Then, we calculated spatiotemporal change of temperature field associated with subduction of the PHS plate at each time step of the numerical simulations. As a result, the most suitable value of the pore pressure ratio at

the plate boundary was estimated to be 0.97. The temperatures of the upper surface of the PHS plate, where many LFEs occur and a seismic gap exists around the Ise Bay, were both estimated to be between 440°C and 480°C. We traced a temperature-pressure path of each profile on the phase diagram of hydrous MORB by using a calculated temperature distribution. The location where dehydration of hydrous MORB occurred in the oceanic crust did not necessarily coincide with high activity regions of LFEs in our modeling. However, along the respective profiles, hydrous MORB was transformed from blueschist to greenschist in the oceanic crust near the regions. In addition, several normal fault type earthquakes were identified within the subducting PHS plate near the seismic gap. This indicates that a tensile stress acting upon near the upper surface of the subducting PHS plate in the east-northeast-west-southwest direction may be the cause of the seismic gap. We concluded that the seismic gap of LFEs may not be caused by temperatures and dehydration processes, but caused by the state of the stress in this region.

In part II, constructing 2-D box-type thermal convection model in the Tokai district, we investigated the relationships among temperature, dehydration, and a seismogenic zone of a megathrust earthquake, and occurrence of deep LFEs and a SSE there. In the Tokai district, the PHS plate is subducting beneath the Amurian plate at about 5.5 cm/yr in the northwest direction. The so-called Tokai earthquake is expected to occur soon there. Inversion analyses of geodetic data during an interseismic period indicate strong interplate coupling at the shallow part of the plate boundary. A strongly coupled region for an expected megathrust Tokai earthquake was identified based on temperature conditions at the plate boundary. A long-term SSE was identified beneath Lake Hamana of the plate interface from 2000 to 2005. In this region, we set up three profiles passing through the Tokai district. We considered the subduction history of the PHS plate during the period from the Middle Miocene to the present day. Besides, we set up thin heat conductive layer on the plate interface, whose depth is ranging from 32 km, which is the depth of the continental Moho, to 60 km, to express the slab-mantle decoupling layer. In our results, the depth range of the seismogenic zone for the megathrust earthquake was estimated to be ranging from 8 to 22 km, narrowing toward the east. Temperatures of the upper surface of the PHS plate, where the Tokai SSE occurred, were estimated to be ranging from 350°C to 410°C. Therefore, the Tokai SSE is considered to have occurred at the transition zone between unstable and stable slidings. Temperatures of the upper surface of the PHS plate, where LFEs occur, were estimated to be ranging from 450°C to 500°C. In addition, hydrous MORB was transformed from blueschist into greenschist near the region where the Tokai SSE

occurred, and dehydration of the oceanic crust was estimated there. Therefore, LFEs is considered to occur near the down-dip limit of the transition zone.

In part III, we simulated temperature and flow fields, and dehydrated water content from the subducting plate in southern Mexico, using a 3-D parallelepiped thermal convection model. We investigated relationships among temperature, dehydration, and occurrences of interplate seismic events. Firstly, we investigated parameter dependency on temperature fields and heat flow. As a result, we found that pore pressure ratio, the thickness of the continental crust, and subducting velocity were predominant model parameters. Secondly, we determined a most suitable model, varying these unknown model parameters by comparing calculated heat flow with observed one. Optimal values of pore pressure ratio and the thickness of the continental crust were estimated to be 0.96 and 40 km, respectively. In the most suitable model, interplate temperature of the seismogenic zone was estimated to be ranging from 100°C to 400°C. Interplate temperature where SSEs and NVTs occurred in southern Mexico were estimated to be ranging from 480°C to 680°C, and from 630°C to 830°C, respectively. The region where the dehydrated water content became maximum was consistent well with the region where SSEs and NVTs occurred in our modeling. Comparing our results with interplate temperature and dehydration process where interpate seismic events such as LFEs and SSEs occurred estimated in Parts Ⅰ and Ⅱ, interplate temperature where these seismic events occurred in southern Mexico is about 150 – 200°C higher than that estimated in central Japan. This difference is mainly because estimated frictional heating on plate interface, which depends on value of pore pressure ratio is higher than that estimated in central Japan. However, as a common feature among them, dehydration from the subducting plate estimated to be maximum near the region where above-mentioned interplate seismic events occurred.

Part Ⅰ

Two-dimensional thermal modeling associated with subduction of the Philippine Sea plate in central Japan, and its relationship to the occurrence of interplate earthquakes

1. Introduction

In central Japan, the oceanic Philippine Sea (PHS) plate is subducting beneath the continental Amurian (AM) plate with low dip angles of 5° to 20° along the Nankai Trough, and deep tremors take place near the plate boundary (e.g., Obara, 2002) (Fig. 1-1). Generation mechanisms of the deep tremors have been considered to be related to dehydration from the subducting PHS plate, because they have mobility, and continue for a long duration up to 2 to 3 weeks, and the belt-like form distribution of epicenters of the deep tremors is almost parallel to the strike of the trough axis (Obara, 2002). Distinguished seismic waveforms, which are considered to be S-waves, have been identified in the continuous waveforms of the deep tremors, which are referred to as deep low-frequency earthquakes (LFEs) (Katsumata and Kamaya, 2003). The distribution of LFEs overlaps with that of the deep tremors. LFEs take place when phase transformations of hydrous minerals in the oceanic crust of the subducting plate occur, and dehydrated water has been considered to be supplied to the plate boundary from the fact that hypocenters of LFEs are concentrated at the plate boundary (e.g., Katsumata and Kamaya, 2003). Shelly et al. (2006) inferred that LFEs or deep tremor occur at the plate boundary, and high fluid pressure there has relationship with the occurrence of LFEs or deep tremors in western Shikoku. Ide et al. (2007) analyzed the P-wave first-motions and S waveforms of deep tremors in Shikoku. They suggested that deep tremors have the focal mechanism of low-angle thrust fault type, so LFEs are considered to be generated on the plate interface.

As for previous thermal modeling studies, Hyndman et al. (1995) combined the calculated temperature fields with experimental data for clay minerals, and estimated the seismogenic zone thermally on the plate boundary in southwest Japan. Wang et al. (1995) introduced frictional heating terms in the energy equation in their 2-D model, and indicated that it plays a significant role in increasing the interplate temperature in southwest Japan. Seno and Yamasaki (2003) inferred that serpentinisation of the tip of

the mantle wedge, which is caused by shallow dehydration of the subducting PHS plate, may have a relationship with the occurrence of deep tremors in the Tokai district of central Japan. Yoshioka and Murakami (2007) estimated temperatures on the plate boundary where many LFEs occur in southwest Japan, using a 3-D thermal convection model. By taking three profiles passing through the southern part of Kyushu, western part of Shikoku, and the Kii Peninsula, Yoshioka et al. (2008) performed numerical simulations using a 2-D thermal convection model, and calculated temperature fields beneath southwest Japan. On the basis of a phase diagram of hydrous MORB, they inferred the amount of water that was considered to cause LFEs. Wada and Wang (2009) calculated temperature fields along the circum Pacific regions, and estimated the depth of peak crustal dehydration to range from 40 km to 47 km in regions where the young and warm plate is subducting, such as southwest Japan. Gao and Wang (2014) indicated that the fault strength of megathrust earthquakes has a relationship with the mode of slip, either creeping or stick-slip, and the creeping megathrust is stronger than the stick-slip. Because fault heat dissipation is different between the two modes, they proposed that thermal observations may be useful for predicting earthquakes.

A seismic gap of LFEs exists beneath the Ise Bay, central Japan, where the PHS plate is bending upward (Fig. 1-1). The dip angle there is approximately 5°, which is less than that of the neighbouring regions with a high level of LFE activity. This suggests that there is a possible difference in temperature, dehydration processes, and the state of stress between the regions with the seismic gap of LFEs and those with a high level of LFE activity.

To determine the cause of the spatial difference in LFE activity, we performed numerical simulations of temperature fields associated with subduction of the PHS plate, using a 2-D thermal convection model developed by Yoshioka et al. (2013). We set up three profiles passing through the Ise Bay where the seismic gap exists (profile B-B'), the eastern part of the Kii Peninsula (profile A-A'), and the Lake Hamana (profile C-C') where many LFEs occur. All of the three profiles were taken in the across-arc directions (Fig.1-1). We also estimated the dehydration processes of each profile, using a phase diagram of hydrous MORB in an oceanic crust by Omori et al. (2009).

2. Data

2.1. Heat flow data

When numerical simulations are performed, it is necessary to investigate whether the calculated temperature structures are valid. Therefore, we evaluated the validity of the

obtained temperature fields by comparing the calculated heat flow with the observed one. As heat flow data, we used Bottom Simulating Reflectors (BSRs) (Ashi et al., 1999; 2002), a marine heat probe and land borehole (Tanaka et al., 2004; Yamano, 2004), and Hi-net observation wells (Matsumoto, 2007) (Fig. 1-2(a)). The spatial distribution of the observed heat flow is shown in Fig. 1-2(b). Areas where the heat flow exceeded more than 150 $\mathrm{mW/m^2}$ were identified near Mt. Hakusan and the Hida mountain range (Fig. 1-2(b)) because of their underground magmatism. In the fore arc, heat flow values are less than 60 $\mathrm{mW/m^2}$. The heat flow in and around the seismic gap was lower than that in the neighbouring regions with high activity of LFEs.

2.2. Uplift and subsidence rates during the Quaternary period

We incorporated the effect of temperature variation due to uplift and subsidence rates of the crust in the energy equation, which will be described later. The amount of uplift and subsidence of the crust in the Quaternary period was obtained from the Quaternary tectonic map of Japan (Research Group for the Quaternary tectonic map, 1968). We converted the amount of vertical displacement U into uplift and subsidence rates v_e, following an empirical relationship proposed by Yoshikawa (1974):

$$v_e = 2\times10^{-6}U - 0.37 \tag{1-1}$$

In general, the larger the uplift rate is, the larger the erosion rate is, assuming that uplift and subsidence rates are equal to erosion and sedimentation rates, respectively. Yoshioka et al. (2013) addressed the importance of using erosion and sedimentation rates to fit the observed heat flow data with a spatially short wavelength of heat flow data on land in southwest Japan. We also incorporated the effect into our model.

The spatial distributions of uplift and subsidence rates during the Quaternary period are shown in Fig. 1-3(a), and the rates along the three profiles are shown in Fig. 1-3(b), (c), and (d). Although regions with large subsidence rates exist in and around the Osaka and Nobi plains, an uplifted region has been dominant over the Japanese islands during the Quaternary period. In particular, there is a large uplifted region around the Hida mountain range, where the amount of uplift is over 1500 m, and the uplift rate exceeds 3 mm/year.

3. Governing equations

We used a momentum equation and an energy equation as governing equations to calculate temperature fields. We treated them as a coupled problem, and solved the

equations using a 2-D finite difference method. Following Andrews (1972), the momentum equation for mantle convection can be expressed as

$$\frac{\partial^2}{\partial x \partial z}\left(4\eta\frac{\partial^2\psi}{\partial x\partial z}\right)+\left(\frac{\partial^2}{\partial z^2}-\frac{\partial^2}{\partial x^2}\right)\left[\eta\left(\frac{\partial^2}{\partial z^2}-\frac{\partial^2}{\partial x^2}\right)\psi\right]=-\frac{\partial}{\partial x}\left(\rho_0 g\,\alpha\, T\right), \tag{1-2}$$

where x and z are the horizontal distance and depth, respectively, η is viscosity, ψ is stream function, ρ_0 is the standard density of the mantle, g is the acceleration of gravity, α is thermal expansivity, and T is temperature.

Following Burkett and Billen (2010), we used viscosity, which was represented by a composite of diffusion creep and dislocation creep:

$$\eta=\frac{\eta_{diff}\eta_{disl}}{\eta_{diff}+\eta_{disl}} \tag{1-3}$$

with

$$\eta_{diff,disl}=\left(\frac{d^p}{AC_{OH}^r}\right)^{\frac{1}{n}}\dot{\varepsilon}^{\frac{1-n}{n}}\exp\left(\frac{E+P_{lc}V}{nRT}\right), \tag{1-4}$$

where η_{diff} and η_{disl} are the viscosities of diffusion and dislocation creeps, respectively, d is grain size, p is grain index, A is coefficient, C_{OH} is water content, r is the water content index, n is the stress index, $\dot{\varepsilon}$ is the second invariant of strain rate tensor, E is activation energy, P_{lc} is lithostatic pressure defined by the depth gradient of compressibility, and V is activation volume, and R is the gas constant.

The energy equation can be expressed as

$$\rho C_p\left(\frac{\partial T}{\partial t}+\mathbf{V}\cdot\nabla T\right)=$$

$$k\nabla^2 T+v\,\rho_0 g\,\alpha\, T+4\eta\left(\frac{\partial^2\psi}{\partial x\partial z}\right)^2+\eta\left(\frac{\partial^2\psi}{\partial x^2}-\frac{\partial^2\psi}{\partial z^2}\right)^2+H_r+\tau\dot{\varepsilon}'+v_e(x)\frac{\partial T}{\partial z}, \tag{1-5}$$

where ρ is density, C_p is specific heat at constant pressure, t is time, $\mathbf{V}$ is a flow velocity vector, k is thermal conductivity, v is a vertical component of flow velocity, H_r is heat generation by a radioactive element, τ is shear stress, $\dot{\varepsilon}'$ is the strain rate

at the plate boundary layer, and $v_e(x)$ is the erosion and sedimentation rates. $\dot{\varepsilon}'$ can be expressed as

$$\dot{\varepsilon}' = \frac{v_s}{w}, \tag{1-6}$$

where v_s is the subducting velocity of an oceanic plate, and w is the thickness of the plate boundary deforming zone. On the left hand side of Eq. (1-5), the first term is temperature variation term with respect to time, and the second is an advection term. On the right hand side of Eq. (1-5), the first term is a conduction term, the second is an adiabatic compression term, the third and fourth are viscous dissipation terms, the fifth is a radioactive heating term, the sixth is a frictional heating term at the plate boundary, and the seventh is a temperature variation term due to erosion and sedimentation rates of the crust. The sixth and seventh terms are described in detail in Yoshioka et al. (2013).
Assuming that density is only dependent on temperature, following Andrews (1972),

$$\rho = \rho_0(1-\alpha T), \tag{1-7}$$

Regarding the fifth term of the right hand side of Eq. (1-5), Furukawa (1995) inferred that radioactive heat H_r is inversely proportional to the depth where the radioactive element has accumulated. The radioactive heat in the continental crust can be expressed as

$$H_r = H_0 \exp\left(-\frac{z}{z_H}\right), \tag{1-8}$$

where H_0 is radioactive heat rate per unit volume, and Z_H is the constant depth (10 km). We assumed that the radioactive element also exists in the accretionary prism, and used the same equation when we calculated its radioactive heat.

4. Model

Following Yoshioka et al. (2013), we constructed a 2-D box-type thermal convection model to calculate temperature fields associated with subduction of the PHS plate. A horizontal distance of 800 km and a depth of 400 km were taken as the model domain. The grid intervals for stream functions and temperatures were set to be 10 km and 2 km, respectively, and the stream function was evaluated at the same grid spacing for the temperature field by bi-cubic spline interpolation at each time step. We set the upper

crust, lower crust, accretionary prism, PHS plate, and mantle in the model domain, as shown in Fig. 1-4 schematically. We treated the upper and lower crusts and the accretionary prism as the conductive regions, and other regions were set to be fluid materials. The PHS plate was set to subduct along a prescribed guide with an imposed subducting velocity. Following Nakajima and Hasegawa (2007), we used isodepth contours of the upper surface of the PHS plate when we set the geometry of the prescribed guide for the oceanic plate.

The initial condition in the model domain was a steady state without mantle flows. Following Yoshioka and Sanshadokoro (2002), the temperature distribution for the half-space cooling model can be expressed as

$$T = T_0 erf\left(\frac{z}{2\sqrt{\frac{kt'}{\rho C_p}}}\right). \tag{1-9}$$

When $z \geq z_0$, considering the adiabatic compression, Eq. (1-9) becomes

$$T = T_0 erf\left(\frac{z}{2\sqrt{\frac{kt'}{\rho C_p}}}\right)\exp\left[\frac{g\alpha}{C_p}(z - z_0)\right], \tag{1-10}$$

where T_0 is a potential temperature, t' is the age of the continental plate, and z_0 is the depth below which the effect of adiabatic compression is considered. The depth z_0 is treated as one of uncertain parameters for fitting the calculated heat flow to the observed one. The values of the model parameters are given in Table 1-1.

As a boundary condition for temperature fields in the model domain, the surface temperature was set to be 0°C. Adiabatic conditions were given for the left and bottom boundaries, and the time-dependent temperature distribution determined by the variable age of the PHS plate was given at the right boundary. As a boundary condition for flow fields, the normal stress was set to be zero for the left, right, and bottom boundaries.

To determine the time-dependent temperature distribution at the right boundary, we considered the subduction history of the PHS plate during the period from the Middle Miocene to the present day based on Kimura et al. (2014). They revised and united several theories of the subduction history of the PHS plate. Because the Japan Sea spread to the northwest at ~17 Ma, southwest Japan initiated a migration with a clockwise rotation. The proto-Izu arc moved eastward, and arrived near its present position at ~11 Ma. Then, the PHS plate might then have stopped subduction at the time,

which is considered to be the end of magmatic activity in southwest Japan. The PHS plate initiated subduction at ~6 Ma when there was a resurgence of volcanic activity in the north of southwest Japan. Recent ocean drilling in the Nankai Trough subduction zone has revealed that the age when the accretionary prism there initiated to grow was about 6 Ma (Saffer et al., 2009). Then, direction of the PHS plate motion is considered to have changed at approximately 3 Ma to its current direction, which is considered from formation age of the Kurotaki inconformity (Takahashi, 2006) or formation age of the Lake Baikal, which is a subsidence part of the Baikal rift zone where the northwestern rim of the AM plate is adjacent to the Eurasian plate. Lake Baikal, which is considered as a part of the trench originally was apart from the sea because of the development of the normal fault around there at approximately 3 Ma (Mats, 1993). Therefore, the relative plate motion was considered to change at 3 Ma when the AM plate was apart from the Eurasian plate. Subduction velocity of the PHS plate along each profile during the period from 3 Ma to the present is estimated by using parameters of an Euler pole between the PHS plate and the AM plate (Demets et al., 2010). Values of the model parameters for the past plate motion, considering such subduction history of the PHS plate, are given in Table 1-2. History of the subduction velocity and the slab thickness of the PHS plate are shown in Fig. 1-5.

5. Results and Discussion

5.1. Comparison between observed and calculated heat flows

The calculated heat flow was obtained, using the temperature distribution associated with subduction of the PHS plate. We compared the calculated heat flow with the observed one to evaluate the validity of the calculated temperature distributions. We evaluated the validity data using the following equation:

$$S = \frac{1}{N}\left[\sum_{i=1}^{N}(O_i - C_i)^2\right]^{\frac{1}{2}}, \tag{1-11}$$

where O_i and C_i are the observed and calculated heat flow values, respectively, N is the total number of data points from the BSRs, the land borehole, marine heat probe, and Hi-net borehole. We applied Eq. (1-11) at distances ranging from 0 km to 200 km from the Nankai Trough for the three profiles together. The calculated heat flow was dependent on the values of model parameters. Among them, the pore pressure ratio λ, radioactive heat generation per unit volume in the accretionary prism H_0, and the

depth z_0 in Eq. (1-10) are the most uncertain parameters. λ can be expressed as

$$\lambda = \frac{p_f - p_d}{p_l - p_d}, \tag{1-12}$$

where p_f is the pore pressure, p_d is the pressure at the Earth's surface, and p_l is the lithostatic pressure (e.g., Wang et al., 1995). Assuming that λ, H_0, and z_0 are free parameters, we attempted to determine their optimal values on the basis of Eq. (1-11), using a grid search. As a result, we found that the values of Eq. (1-11) were more changeable for the pore pressure ratio λ than radioactive heat generation H_0 and the depth z_0. Therefore, the former tends to be determined uniquely, but the latter is difficult to determine. The optimal values of λ, H_0, and z_0 for the three profiles were estimated to be 0.97, 3.0 $\mu W/m^3$, and 100 km, respectively. Contours of S values in Eq. (1-11) determined by combinations of three uncertain parameters are shown in Fig. 1-6. Yoshioka et al. (2013), Seno (2009), and Yoshioka et al. (2015) estimated the pore pressure ratio to be 0.95 and 0.98 in southwest Japan, and 0.98 in the Kanto district of central Japan, respectively. Hamamoto et al. (2011) calculated the 2-D temperature field associated with subduction of the PHS plate beneath the Kii Peninsula, and estimated the effective friction coefficient μ' and radioactive heat generation in the accretionary prism H_0 by fitting calculated heat flow to observed one. They estimated μ' and H_0 as 0.05 and 2.0 $\mu W/m^3$, respectively. They considered the lithostatic pressure P_l as the normal stress σ_n, and expressed the shear stress as

$$\tau = \mu' \sigma_n = \mu' P_l = \mu' \rho g z. \tag{1-13}$$

In this study, following Byerlee's (1978) friction law, shear stress τ on a plate interface for the brittle regime was expressed as

$$\tau = 0.85\sigma_n(1-\lambda) \ \left(\sigma_n(1-\lambda) \le 200MPa\right). \tag{1-14}$$

Comparing Eq. (1-13) with Eq. (1-14), when the effective frictional coefficient μ' is 0.05, the pore pressure ratio λ in Hamamoto et al. (2011) ranges from 0.94 to 0.95.

Fig. 1-7 shows a comparison between the observed and calculated heat flows for

the three profiles, for which Eq. (1-11) was minimized. The observed heat flow was explained well by our model except for the heat flow on land in profile A. The calculated heat flow for frictional heating with a value of 0.97 of λ at the plate boundary was approximately 15 $\mathrm{mW/m^2}$ larger than that without frictional heating at a horizontal distance of up to approximately 140 km from the trough axis in profile B (Fig. 1-7(b)). With regard to the two free parameters λ and H_0 on the calculated heat flow, H_0 in the accretionary prism was related to heat flow at distances between 0 km and 90 km. If a value of 1.0 $\mu\mathrm{W/m^3}$ was used instead of 3.0 $\mu\mathrm{W/m^3}$ there, the heat flow in this region was lowered by approximately 5 $\mathrm{mW/m^2}$. λ had a significant influence on frictional heating at the plate boundary, and its contribution to heat flow was larger than that of radioactive heating. The horizontal distances where heat flow rises most in the respective figures were situated above the region where the shear stress at the plate boundary was maximum, corresponding to the transition from a brittle to ductile regime. Frictional heating affected heat flow values at horizontal distances between 0 km and 220 km, 0 km and 250 km, and 0 km and 190 km from the trough axis in profiles A, B, and C, respectively.

5.2. Comparison of cross-sectional temperature distributions and temperature distributions on the upper surface of the PHS plate

Fig. 1-8 shows the calculated cross-sectional temperature distributions at present for the three profiles. Fig. 1-9 shows the spatially interpolated temperature distributions of the upper surface of the subducting PHS plate at present obtained from the three profiles, and the distribution of epicenters of LFEs determined by the Japan Meteorological Agency during the period from October 1, 1997 to February 28, 2015. Following Hyndman et al. (1995), we estimated the seismogenic zone for potential future megathrust earthquakes, which is thought to be controlled by temperatures. The temperature range of 150–350°C corresponds to the seismogenic zone. The thermally estimated seismogenic zone was at depth range from 6 km to 21 km, and became slightly wider near profile B than near profiles A and C. The depth of the up-dip limit of the seismogenic zone was consistent with Yoshioka and Murakami (2007). The depth of the down-dip limit of the seismogenic zone estimated in this study was slightly deeper than that estimated in Yoshioka and Murakami (2007). This discrepancy may be caused by the difference in the estimated pore pressure ratio on the plate interface, the used geometry model of the PHS plate, and the assumed subduction history of the PHS plate. Liu et al. (2010) estimated the seismogenic zone geodetically from the slip-deficit distribution obtained from an inversion analysis of GPS data on land. Comparing the

up-dip and down-dip limits of the seismogenic zone with those obtained in this study, they were almost identical around the three profiles.

We used unified hypocenter data for LFEs, and excluded data with standard errors in the hypocenter depths more than 10 km. In this study, we did not relocate hypocenters of LFEs. However, when deep tremors are relocated, they occur near Nagoya where few hypocenters are plotted in Fig. 1-1 (e.g., Obara and Hirose, 2006). However, there certainly exists a seismic gap around the Ise Bay in these previous study. So, we set profile B to pass through its seismic gap with reference to these studies.

As a result, we found that almost all of the LFEs occurred near the plate boundary at horizontal distances of 140 km to 170 km from the trough axis in profiles A and C, and their depths ranged from 30 km to 40 km. A comparison of the temperature distributions on the upper plate boundary indicated that temperatures where the LFE activity was high ranged from 440°C to 480°C at the above-described at horizontal distances in profile A and C, which is consistent with Yoshioka and Murakami (2007). So, temperature condition of the region where activity of LFEs is high is considered to be consistent with that of transition zone from unstable to stable sliding (Hyndman et al., 1995). On the other hand, temperatures on the upper surface of the slab around the seismic gap of LFEs ranged from 500°C to 520°C at depths of about 30 km in profile B, which was about 30–50°C higher than the temperatures in profiles A and C. This indicates that temperature difference in the upper surface of the PHS plate between the high activity and gap regions of LFEs is not so large.

5.3. Comparison of the cross-sectional water content distributions in the oceanic crust

Here, we consider dehydration from the oceanic crust of the PHS plate. We assumed that MORB consists of hydrous minerals in the oceanic crust, and investigated the dehydration process along each profile. To determine the temperature and depth dependent water content in hydrous MORB, we used phase diagram by Omori et al. (2009).

Figs. 1-10(a), (b), and (c) show vertical cross sections of the water content distributions of hydrous MORB in the oceanic crust for the three profiles. Distinct dehydration occurred when a certain mineral of hydrous MORB transforms into another mineral, which are accompanied by variation in the temperature-depth conditions within the oceanic crust. The areas of the dehydration from the blueschist to the greenschist phase tansformation in profiles A and B were far from hypocentre and the

corresponding gap of LFEs, respectively. We also investigated the V_p/V_s ratio obtained by seismic tomography (Matsubara and Obara, 2011) along the three profiles (Fig. 1-11). The results showed that the area where blueschist transforms into greenschist in profile C corresponds well with the area with a high V_p/V_s ratio, with high activity of LFEs. However, areas with high V_p/V_s ratio are rare in profiles A and B. Therefore, we suggest that the temperature conditions near the plate interface are more important than the dehydration of hydrous MORB in the oceanic crust for occurrence of LFEs, and
LFEs occur where temperature range of the plate interface is corresponding to the transition zone from unstable to stable sliding.

5.4. The state of stress in and around the seismic gap of LFEs

By investigating the centroid moment tensor solutions in central Japan using F-net observation data provided by the National Research Institute for Earth Science and Disaster Prevention (NIED) during the period from October 1, 1997 to February 28, 2015, several normal fault type earthquakes with T-axes oriented in the east-northeast-west-southwest direction were identified in the upper part of the subducting PHS plate near Nagoya, passing through profile B, where the PHS plate is bending upward (Fig. 1-12(a)). At depths ranging from 10 km to 20 km, corresponding to the lower part of the continental crust, several reverse fault earthquakes were identified only near Tsushima (Fig. 1-12(a)) where the PHS plate is bending upward most. On the other hand, low-angle thrust type very low-frequency earthquakes (VLFEs) with P-axes oriented in the northwestward convergence direction of the PHS plate occurred at the plate boundary in the belt-like LFE occurring region (Ito et al., 2007). Therefore, a tensile stress in the east-northeast-west-southwest direction is expected to be acting where the seismic gap of LFEs appears. Therefore, the state of stress in this area is different from that in the neighboring areas with high activity of LFEs.

In this study, we assume that the compressive stress acting upon the PHS plate in the east-northwast-west-southwest direction is the cause of the upward bending of the PHS plate. We treated it as a problem of deformation of an elastic plate in a viscous fluid. Following Turcotte and Schubert (2002), the amplitude of the upper surface of the PHS plate w along profile D (Fig. 1-12(a)) can be expressed as

$$w = A\cos\left(\frac{2\pi y}{\Lambda}\right), \tag{1-15}$$

where A is the coefficient, y is the horizontal coordinate, and Λ is the wavelength of the shape of the PHS plate along profile D. By curve fitting of Eq. (1-15) to the observed geometry, we obtained the wavelength Λ to be 340 km. The wavelength Λ can be also expressed as follows (Turcotte and Schubert, 2002):

$$\Lambda = \pi h\left(\frac{E}{\sigma(1-\nu)^2}\right)^{\frac{1}{2}}, \tag{1-16}$$

where h is plate thickness (35 km) (Fig. 1-12(b)), E is Young's modulus, σ is compressive stress along profile D, and ν is Poisson's ratio. Following PREM (Dziewonski and Anderson, 1981), E and ν are assumed to be 1.11×10^5 MPa and 0.255 at a depth of 30 km, respectively. Substituting the value of the wavelength Λ into Eq. (1-16), we obtained the compressive stress σ to be 1250 MPa. If this is the case, shear fracture would occur by the decrease of fracture strength (Seno et al., 2001).

As for difference of temperature condition and dehydration process of hydrous MORB between the seismic gap and the high active areas of LFEs, there are little difference of temperature on the plate interface between them at depth range from 30km to 40 km (Fig. 1-9), and there are no distinct dehydration along profiles A and B at depth range from 30km to 40 km (Figs. 1-10(a), and (b)) despite the difference of frequency of occurrence of LFEs between them. From these analyses and consideration, the seismic gap of LFEs beneath the Ise Bay may have relationship with the state of stress because the high compressive stress would cause shear fracture of the PHS plate where the PHS plate is bending upward most.

6. Conclusions

In this study, we performed numerical simulations to investigate the occurrence mechanisms of shallow to deep interplate earthquakes in central Japan, using a 2-D box-type thermal convection model, and calculated the temperature distributions associated with subduction of the PHS plate along the three profiles. In addition, using a phase diagram of hydrous MORB, we examined the dehydration process associated with subduction of the PHS plate. The significant results obtained in this study can be summarized as follows:

(1) The depth range of the thermally estimated seismogenic zone at the plate boundary ranged from 6 km to 21 km in central Japan. It was slightly wider along profile B,

which passed through the seismic gap of LFEs than the other two profiles A and C.

(2) The temperature range of the upper surface of the subducting PHS plate, where many LFEs occur, was about 440–480°C along profiles A and C, whereas it was approximately 500–520°C in the seismic gap of LFEs along profile B. So, there are little differences of temperatures on the plate interface between them. Therefore, temperatures both in high activity of LFEs and the seismic gap were consistent with that of transition zone from unstable to stable sliding.

(3) The temperature-depth conditions in areas where many LFEs occur corresponded to the phase transformation from blueschist to greenschist of hydrous MORB in the oceanic crust in profile C. However, dehydration of hydrous MORB was not expected near high activity areas of LFEs in profile A and B. These results are consistent with distributions of V_p / V_s ratio obtained from seismic tomography.

(4) Shear fracture of the PHS plate may occur beneath the Ise Bay by the high compressive stress in the northeast-east-southwest-west direction. This may be the reason why LFEs do not occur there.

Acknowledgments

We thank Junichi Nakajima for providing geometry data of the upper surface of the PHS plate. We also thank Japan Meteorological Agency and National Research Institute for Earth Science and Disaster Prevention (NIED) for providing data of hypocenters of LFEs and centroid moment tensor solutions, respectively. All the figures were created by using the Generic Mapping Tools (GMT) developed by Wessel and Smith (1998).

References

Akaike, H., 1980. Likelihood and the Bayes procedure. Bayesian Statistic (eds. J. M. Bernardo, M. H. Degroot, D. V. Lindley and A. F. M. Smith), Valencia University Press, Spain.

Andrews, D.J., 1972. Numerical simulation of sea-floor spreading. J. Geophys. Res. 77, 6470-6472.

Ashi, J., Tokuyama, H., and Taira, A., 2002. Distribution of the methane hydrate BSRs and its implication for the prism growth in the Nankai Trough, Marine Geology 3110,1-15.

Ashi, J., Tokuyama, H., Ujiie, Y., and Taira, A., 1999. Heat flow estimation from gas hydrate BSRs in theNankai Trough, Implications for the thermal structure of the Shikoku Basin. Suppl. EOS Trans., AGU.80 (46), T12A-02.

Byerlee, J., D., 1978. Friction of Rocks. Pure and Applied Geophysics 116 (4-5), 615–626.

Burkett, E.R. and Billen, M.I., 2010. Three-dimentionality of slab detachment due to ridge-trench collision: Laterally simultaneous boundinage versus tear propagation. Geochem. Geophys. Geosyst. 11, doi:10.1029/2010GC003286.

DeMets, C., Gordon, R. G., and Argus, D. F., 2010. Geologically current plate motions. Geophys. J. Int. 181, 1-80.

Dziewonski, A., and Anderson, D., 1981. Preliminary reference earth model. Physics of the Earth and Planetary Interiors 25, 297–356.

Furukawa, Y., 1995. Temperature structure in the crust of the Japan arc and the thermal effects of subduction. In: M.L. Gupta & M. Yamano, Editors, Terrestrial Heat flow and Geothermal Energy in Asia, Oxford & IBH Publishing Co. Pvt. Ltd., New Delhi. 213-219.

Gao, X., and Wang, K., 2014. Strength of stick-slip and creeping subduction megathrusts from heat flow observations. Science 345, 1038-1041.

Hamamoto, H., Goto, S., Kinoshita, M., Fujino, K., and Wang, K., 2011. Heat flow distribution and thermal structure of the Nankai subduction zone off the Kii Peninsula. Geochem. Geophys. Geosyst. 12, doi:10.1029/2011GC003623.

Hirose, F., Nakajima, J., and Hasegawa, A., 2008. Three-dimensional seismic velocity structure and configuration of the Philippine Sea slab in southwestern Japan estimated by double-difference tomography. J. Geophys. Res. 113, B09315.

Honda, S., 1997. Mantle dymanics II—mechanics, in Iwanami-koza. Earth and Planetary Science 10 Dynamics of the Earth's interior, Iwanami-Shoten, Tokyo. pp. 73–121 (in Japanese).

Hyndman, R., Wang, K., and Yamano, M., 1995. Thermal constraints on the seismogenic protion of the southwestern Japan subduction thrust. J. Geophys. Res. 100,15373-15392.

Ide, S., D. R. Shelly, amd G. C. Beroza, 2007. The mechanism of deep low frequency earthquakes: Further evidence that deep non-volcanic tremor is generated by shear slip on the plate interface. Geophys. Res. Lett. 34, L03308, doi:10.1029/2006GL028890.

Ito, Y., Obara, K., Shiomi, K., Sekine, S., and Hirose, H., 2007. Slow earthquakes coincident with episodic tremors and slow slip events, Science, 315, 503–506.

Katsumata, A. and Kamaya, N., 2003. Low-frequency continuous tremor around the Moho discontinuity away from volcanoes in the southwest Japan. Geophys. Res. Lett. 30, 1020, doi: 10.1029/2002GRL015981.

Kimura, G., Hashimoto, Y., Kitamura, Y., Yamaguchi, A., and Koge, H., 2014. Middle Miocene swift migration of the TTT triple junction and rapid 4 crustal growth in SW Japan. Tectonics 33, 1219-1238.

Liu, Z., Owen S., Dong D., Lundgren P., Webb F., Hetland E., and Simons M., 2010. Integration of transient strain events with models of plate coupling and areas of great earthquakes in southwest Japan, Geophys. J. Int. 181, 1292-1312.

Mats, V. D., 1993. The structure and development of the Baikal rift depression. Earth-Sci. Rev. 34, 81-118.

Matsubara, M. and Obara, K., 2011. The 2011 Off the Pacific Coast of Tohoku earthquake related to a strong velocity gradient with the Pacific plate. Earth Planets Space 63, 663-667.

Matsumoto, T., 2007. Terrestrial heat flow anomaly at non-volcanic area in Southwest Japan based on the NIED Hi-net. Japan Geoscience Union Meeting 2010. T154-001 (in Japanese).

Nakajima, J. and Hasegawa, A., 2007. Subduction of the Phlippine Sea plate beneath southwestern Japan: Slab geometry and its relationship to arc Magmatism. J. Geophys. Res. 112, B08306.

Obara, K., 2002. Nonvolcanic deep tremor associated with subduction in southwest Japan. Science 296, 1679-1681.

Obara, K., and Hirose, H., 2006. Non-volcanic deep low-frequency tremors accompanying slow slips in the southwest Japan subduction zone. Tectonophysics 417, 33-51.

Omori, S., Kita, S., Maruyama, S., and Santosh, M., 2009. Pressure-temperature conditions of ongoing regional metamorphism beneath the Japanese Islands. Gondwana Res. 16, 458-469.

Research Group for the Quaternary Tectonic Map, 1968. Quaternary Tectonic Map of Japan. Quaternaly research 7, 182-187 (in Japanese).

Saffer, D., McNeill, L., Araki, E., Byrne, T., Eguchi, N., Toczko, S., Takahashi, K., and the Expedition 319 Scientists, 2009. NanTroSEIZE Stage 2: NanTroSEIZE riser/riserless observatory. IODP Prel. Rept. 319.

Seno, T., 2009. Determination of the pore fluid pressure ratio at seismogenic megathrusts in subduction zones: Implications for strength of asperities and Andean-type mountain building. J. Geophys. Res. 114, B05405.

Seno, T., and Yamasaki, T., 2003. Low-frequency tremors, intraslab and interplate earthquakes in Southwest Japan - from a viewpoint of slab dehydration. Geophys. Res. Lett. 30, doi: 10.1029/2003GL018349.

Seno, T., Zhao, D., Kobayashi, Y., and Nakamura, M., 2001. Dehydration of serpentinized slab mantle: Seismic evidence from southwest Japan. Earth Planet. Space 53, 867-871.

Shelly, D. R., Beroza, D. C., and Ide, S., 2006. Non-volcanic tremor and low-frequency earthquake swarms. Nature 446, 305-307.

Takahashi, M., 2006. Tectonic Development of the Japanese Islands Controlled by Philippine Sea Plate Motion. Journal of Geography 115, 116-123 (in Japanese).

Takenaka, S., Sanshadokoro, H., and Yoshioka, S., 1999. Velocity anomalies and spatial distributions of physical properties in horizontally lying slabs beneath the Northwestern Pacific region. Phys. Earth Planet. Inter. 112, 137-157.

Tanaka, A., Yamano, M., Yano, Y., and Sasada, M., 2004. Geothermal gradient and heat flow data in and around Japan, digital geoscience map DGN P-5. Geological Survey of Japan.

Turcotte, D., and Schubert, G., 2002. Geodynamics: Second Edition. Cambridge University Press, New York, 249-254.

Wada, I. and Wang, K., 2009. Common depth of slab-mante decoupling: Reconciling diversity and uniformity of subduction zones. Geochem. Geophys. Geosys. 10, doi:10.1029/2009GC002570.

Wang, K., Hyndman, R.D., and Yamano, M., 1995. Thermal regime of the Southwest Japan subduction zone: effects of age history of the subducting plate. Tectonophysics 248, 53-69.

Wessel, P., and Smith, W.H.F., 1998. New, improved version of the generic mapping tools released. EOS Trans. AGU 79, 579.

Yamano, M., 2004. Heat Flow Data in and around Japan, Digital Geoscience Map DGM P-5. Geological Survey of Japan.

Yoshikawa, T. 1974. denudation and tectonic movement in contemporary Japan. Bull. Dept. Geogr., Univ. Tokyo 6, 1-14.

Yoshioka, S., Ji, Y., and Matsumoto, T., 2015. 3-D thermal modeling associated with subduction of the Philippine Sea plate in southwest Japan. Central Asian tectonics and Western Pacific Geodynamics international workshop, Wuhan.

Yoshioka, S. and Murakami, K., 2007. Temperature distribution of the upper surface of the subducted Philippine Sea plate along the Nankai Trough, southwest Japan, from a three-dimentional subduction model: relation to large interpolate and low-frequency earthquakes. Geophys. J. Int. 171, 302-315.

Yoshioka, S. and Sanshadokoro, H., 2002. Numerical simulations of the deformation and dynamics horizontally lying slabs. Geophys. J. Int. 151, 69-82.

Yoshioka, S., Suminokura, Y., Matsumoto, T., and Nakajima, J., 2013. Two-dimensional thermal modeling of subduction of the Philippine Sea plate beneath southwest Japan. Journal of Geodynamics 608, 1094-1108.

Yoshioka, S., Toda, M., and Nakajima, J., 2008. Regionality of deep low-frequency earthquakes associated with subduction of the Phillippine Sea plate along the Nankai Trough, southwest Japan. Earth Planet. Sci. Lett. 272, 189-198.

Table 1-1. Values of model parameters to calculatie temperature fields

Parameters to calculate temperature fields			
$C_p\ (\mathrm{Jkg^{-1}K^{-1}})$	specific heat at constant pressure	1.046 (1)	
$\alpha\ (\mathrm{K^{-1}})$	thermal expansivity	2.0×10^{-5} (2)	
$T_0\ (^\circ\mathrm{C})$	potential temperature	1350 (3)	
$\rho_0\ (\mathrm{kgm^{-3}})$	standard density of the mantle	3400 (1)	
Parameters to calculate viscosity (4)		diffusion creep	dislocation creep
n	stress index	1.0	3.5
$A\ (\mathrm{s^{-1}Pa^{-n}\mu m^{p}C_{OH}{}^{-r}})$	coefficient	1.0	9.5×10^{-20}
$E\ (\mathrm{kJmol^{-1}})$	activation energy	335	480
$V\ (\mathrm{m^3mol^{-1}})$	activation volume	4.0×10^{-6}	11×10^{-6}
$d\ (\mu\mathrm{m})$	grain size	10000	—
p	grain index	3.0	—
$C_{OH}\ (\mathrm{ppm})$	water content	1000	1000
r	water content index	1.0	1.2

(1) Yoshioka and Sanshadokoro (2002); (2) Honda (1997); (3) Takenaka at al. (1999); (4) Burkett and Billen (2010)

Table 1-2. Values of model parameters used to determine the age and subduction velocity of the PHS plate

Period （Ma）	Subduction velocity [vertical component] （cm/yr）	Subduction velocity [horizontal component] （cm/yr）	Migration length [direction parallel to the trough axis] (km)	Subduction velocity （cm/yr）	Azimuth
15–14	3.68	6.32	63.18	7.31	N25.5° E
14–13	3.68	6.32	126.36	7.31	N25.5° E
13–12	2.52	6.86	194.99	7.31	N35.6° E
12–11	1.28	7.20	266.97	7.31	N45.7° E
11–10	0.00	7.31	340.07	7.31	N55.7° E
10–9	0.00	7.31	413.17	7.31	N55.7° E
9–8	0.00	7.31	486.27	7.31	N55.7° E
8–7	0.00	7.31	559.37	7.31	N55.7° E
7–6	2.36	4.44	603.77	5.03	N22.7° E
6–5	4.17	2.81	631.86	5.03	N0.3° W
5–4	5.00	0.52	637.05	5.03	N28.3° W
4–3	4.66	-1.89	618.13	5.03	N56.4° W
3–2	5.04	-2.43	593.86	5.59	N60.0° W
2–1	5.04	-2.43	569.59	5.59	N60.0° W
1–0	5.04	-2.43	545.32	5.59	N60.0° W

Part Ⅱ

Relationships among temperature, dehydration of the subducting Philippine Sea plate, and the occurrence of a megathrust earthquake, low-frequency earthquakes, and a slow slip event in the Tokai district, central Japan

1. Introduction

In the Tokai district, central Japan, the Philippine Sea (PHS) plate is subducting beneath the Amurian (AM) plate at about 5.5 cm/yr in the northwest direction along the Sagami Trough (Demets et al., 2010) (Fig. 2-1). The so-called M-8 class Tokai earthquake is expected to occur at the shallow part of the plate boundary in the near future (e.g., Ishibashi, 1980). Inversion analyses of geodetic data during an interseismic period indicate strong interplate coupling at the shallow part of the plate boundary (e.g., Yoshioka et al., 1993; Sagiya, 1999; Ohta et al., 2004; Liu et al., 2010). A long-term slow slip event (SSE) was identified beneath Lake Hamana of the plate interface from 2000 to 2005 (Ozawa et al., 2001, 2002; Miyazaki et al., 2006). According to Miyazaki et al. (2006), the Tokai SSE had two slow subevents. The first initiated in the outheast of the slipped region during the period from late June 2000 to early 2001. The second initiated in the northeast during the period from early 2001 to November 2002. The cumulative moment magnitude reached 6.8 in November 2002. Furthermore, non-volcanic deep low-frequency earthquakes (LFEs) are distributed in a belt-like form from the western part of Shikoku to the southern part of Nagano Prefecture, which are almost parallel to the strike of the subducting PHS plate in southwest Japan (e.g., Obara, 2002). For hypocenter data of the LFEs, we used unified data from the Japan Meteorological Agency (JMA) during the period from October 1, 1997 to February 28, 2015 (Fig. 2-1(a)). We excluded data that had a standard error of hypocenter depths over 10 km, taking poorly determined hypocenters due to the lack of observed data into account. Katsumata and Kamaya (2003) claimed that the fluid came from the subducting PHS plate by dehydration when chlorite was transformed into amphibole at a temperature of about 600 ° C at a depth range of 30-50 km, which has a relationship with the occurrence of LFEs. Based on two dimensional thermal modeling, Seno and Yamasaki (2003) inferred that serpentinization of the tip of the mantle wedge was

produced by dehydration of the subducting PHS plate in the Tokai district. They estimated that the temperature for the occurrence of LFEs ranges from about 350 °C to 450 °C there. Therefore, different types of earthquakes can be identified from shallow to deep portions of the plate boundary in the Tokai district.

On the other hand, Hyndman and Wang (1993) estimated an up-dip limit of a seismogenic zone on the plate boundary from experimental data of clay minerals. They estimated that temperature range of 100-150 °C on the plate boundary corresponds to the up-dip limit when clay minerals dehydrate and unstable sliding is possible by velocity weaking. Quartz or feldspar in the subducting plate causes plastic deformation at temperature range of 350-400 °C , which corresponds to the down-dip limit of the seismogenic zone because slip mode transfers from unstable to stable sliding by velocity strengthing. The temperature range of the transition zone from unstable to stable sliding was estimated between 350 °C and 450 °C.

In this study, we performed numerical simulations of the subducting PHS plate in the Tokai district using a 2D box-type thermal convection model to elucidate the relationships among temperature, dehydration associated with subduction of the PHS plate, and the occurrence of SSE and LFEs and to estimate the seismogenic zone for the future megathrust earthquake. We set up three profiles, which are almost parallel to the plate convergent direction of the PHS plate in the Tokai district. We used observed heat flow data to evaluate the validity of the calculated thermal structures. Because of dense observation points of Hi-net and BSRs, we were able to compare the calculated heat flows with observed ones in detail, which enabled us to elucidate correct thermal structures from shallow to deep portions of the plate boundary. Besides, we adopted complex subduction history of the PHS plate in our model, referring to the recent studies (e.g., Kimura et al., 2014) to assign realistic spatiotemporal changing temperature boundary condition. Therefore, we were able to calculate spatiotemporal change of temperature field associated with subduction of the PHS plate at each time step of the numerical simulations.

2. Governing equations and model setting

As governing equations, we used momentum and energy equations to calculate the temperature and flow fields. We solved the equations as a coupled problem, using a 2D finite difference method. The momentum equation for mantle convection and the energy equation are shown in Eqs. (1-2) and (1-5), respectively. As for a frictional heating term at the plate boundary in Eq. (1-5), shear stress in the brittle regime is shown in Eq. (1-14), and that in the ductile regime is following Caristan (1982);

$$\tau_d = \frac{1}{2} A^{-\frac{1}{n}} \dot{\varepsilon}^{\frac{1}{n}} \exp\left(\frac{E}{nRT}\right) \tag{2-1}$$

where A is coefficient, n is index, $\dot{\varepsilon}$ is the shear strain rate, E is the activation energy, R is gas constant, and T is temperature, respectively. Density is only dependent on temperature, as shown in Eq. (1-7). The composite equation of viscosity between diffusion and dislocation creep is shown in Eq. (1-4), and the generalized equation of viscosity is shown in Eq. (1-3).

In the model domain, we defined the upper crust, the lower crust, the accretionary prism, the down-going slab, and the mantle (Fig. 2-2). The upper crust, the lower crust, and the accretionary prism were assumed to be conductive, and other regions were defined as fluid materials. The PHS plate was considered to subduct along a prescribed guide at a defined subduction velocity. Following Wada and Wang (2009), we set up thin heat conductive layer on the plate interface, whose depth is ranging from 32 km, which is the depth of the base of the continental lower crust, to 60 km, to express the slab-mantle decoupling layer. The grid intervals for stream functions and temperatures were set to be 10 km and 2 km, respectively. To define the shape of the upper surface of the subducting PHS plate, we used the results of seismic tomography and seismic refraction surveys in the Tokai district (Kodaira et al., 2004; Nakajima and Hasegawa, 2007; Hirose et al., 2008; Kato et al., 2010).

The initial condition for flow fields in the 2D box-type model domain was steady state without mantle flow. We adopted the 1D half-space cooling model as the initial temperature distribution, taking account of the adiabatic compression as shown in Eqs. (1-9) and (1-10). The values of model parameters are given in Table 2-1.

As a boundary condition for the temperature fields, the surface temperature was set to be 0°C. The adiabatic condition was given for the left and bottom boundaries, and the time-dependent temperature distribution determined by the variable ages of the PHS plate was given at the right boundary. As a boundary condition for the flow fields, normal stress was set to be zero for the left, right, and bottom boundaries.

As for the temperature condition and subducting velocity at the right boundary, we considered the following spatiotemporal change in the plate motion of the PHS plate: We assumed that the PHS plate initiated subduction at 15 Ma from the Sagami Trough in the north-northwest direction at a subduction velocity of 4.0 cm/yr (Wang et al., 1995). This age was determined by the formation age of the Setouchi volcanic belt (Tatsumi, 2006). The PHS plate moved while rotating clockwise during the period from

15 Ma to 11 Ma. Then, the direction of motion of the PHS plate became to be perpendicular to the direction of profiles in our model at 11 Ma. The PHS plate initiated subduction at 7 Ma again when there was a resurgence of volcanic activity in the north of southwest Japan. Since then, we assumed that the convergence rate of the plate motion of the PHS plate with respect to the Eurasian (EU) plate was 4.8-5.0 cm/yr in the northwest direction in the Tokai district (Demets et al., 2010). Considering the separation of the Amurian (AM) plate from the Eurasian plate at 3 Ma (Jolivet et al., 1989; Takahashi, 2006), the convergence rate of the plate motion of the PHS plate with respect to the AM plate changed to 5.3–5.4 cm/yr (Demets et al., 2010). Time-dependent temperature at the right boundary with temporal change of the age of the PHS plate can be expressed as

$$T = T_0 erf\left(\frac{z}{2\sqrt{\frac{kt''}{\rho C_p}}}\right). \tag{2-2}$$

When $z \geq z_0$, taking account of the adiabatic compression, Eq. (2-2) becomes

$$T = T_0 erf\left(\frac{z}{2\sqrt{\frac{kt''}{\rho C_p}}}\right)\exp\left[\frac{g\alpha}{C_p}\left(z - z_0^{'}\right)\right], \tag{2-3}$$

where $z_0^{'}$ is the depth below which the effect of adiabatic compression is taken into account, and t''(Myr) is the age of the PHS plate at the right boundary. Temporal changing of t'' is determined as follows:

$$t'' = \left(t_{calc} + \frac{\left|X - \int_0^t v_s(t)dt\right|}{v_r}\right)\times 10^{-6}, \tag{2-4}$$

where t_{calc} (yr) is elapsed time since the initiation of subduction of the PHS plate, $|X|$ (cm) is the distance between the fossil ridge (the Kinan Seamount Chain; Fig. 2-1(b)) axis at 15 Ma and starting point of each profile on the Sagami Trough, $v_s(t)$ (cm/yr) is temporal migration rate of the PHS plate during the period from 15 Ma to the present whose direction is projected onto perpendicular to each profile, and v_r is spreading rate of the Shikoku Basin, which was determined to be 3.12 cm/yr, referring to Shiono

(1988). Following Yoshii (1975), the spatiotemporal changing thickness of the subducting PHS plate H (km) was given as follows:

$$H = 7.5\sqrt{t''}. \quad (2\text{-}5)$$

3. Results and discussion

3.1. Determination of unknown parameters

To evaluate the validity of the estimated thermal structures, we compared calculated heat flows with observed ones. For heat flow data, we used Bottom Simulating Reflectors (BSRs) (9 et al., 1999; 2002), observation wells of Hi-net (Matsumoto, 2007), and land borehole and marine heat probes (Tanaka et al., 2004; Yamano, 2004).

In our previous study (Suenaga et al., 2015), we treated pore pressure ratio λ, radioactive heat generation per unit volume in the accretionary prism H_0, and the depth z_0' in Eq. (1-10) as uncertain parameters to determine the most suitable thermal structures in central Japan, respectively. In this study, we treated λ and z_0' as free parameters, taking account of the regional difference between central Japan and the Tokai district, and redetermined their optimal values (Fig. 2-3). As for H_0 in the accretionary prism, we assumed the value of 3.0 $\mu W/m^2$, which was obtained in Suenaga et al. (2015). This is because heat flow data, especially BSRs, are poorly available in the marine areas in the Tokai district, which are important to determine H_0 in the accretionary prism with limited shorter length. The Root Mean Square values in Fig. 2-3 were calculated same as Eq. (1-11). We adopted Eq. (1-11) at distances ranging from 0 km to 250 km from the Sagami Trough for the profiles B and C together. As a result, the optimal values of λ and z_0 were estimated to be 0.97 and 40.0 km, respectively. Fig. 2-4 shows observed and calculated heat flows at present for the two profiles, for which Eq. (1-11) was minimized. As for profile A, we used the same calculated heat flows as Suenaga et al. (2015), which was also determined to minimize Eq. (1-11), using the above-described three unknown parameters.

3.2. Temperature distributions of the upper surface of the PHS slab, and its relationship to the megathrust future earthquake, the SSE, and LFEs

Fig. 2-5 shows the calculated cross-sectional temperature distributions at present for the three profiles in Fig. 2-1(a). Figure 2-6 shows temperature distribution of the upper surface of the subducting PHS plate obtained by interpolating the slab surface temperatures for profiles A, B, and C. The depth range of the thermally estimated seismogenic zone, corresponding to temperatures of 150-350 °C, is between 8 and 22 km in the Tokai district (Fig. 2-6). From the figure, we find that the thermally estimated seismogenic zone becomes gradually narrower toward the east. Ohta et al. (2004) estimated the slip-deficit rate distributions at the plate boundary by applying an inversion analysis using GEONET during the interseismic period from April 1, 1997 to April 30, 2000. They estimated that the depth range of the strongly coupled region ranges from 10 to 25 km in the Tokai district. The strongly coupled region was also estimated from the seismicity pattern around the plate interface whose depth on the upper surface of the PHS plate was ranging from 10 to 30 km (Matsumura, 1997). As a common feature among the three model results, the seismogenic zone becomes narrower toward the east. However, the up-dip and down-dip depths of the thermally estimated seismogenic zone in this study is slightly shallower than that estimated by the other two models. One possible reason for the difference in depth is that the geometry of the upper surface of the PHS plate adopted in this study is different from those used in the previous studies.

Miyazaki et al. (2006) investigated the slip rate of the Tokai SSE during the period from January 1, 2000 to November 30, 2002, using GEONET. The region where the cumulative slip rate during the period exceeds 10 cm (Fig. 2-1(a)) is treated as the region where the Tokai SSE occurred in this study. Temperatures on the plate boundary beneath Lake Hamana, near which the Tokai SSE occurred, were estimated to range from 350 °C to 450 °C, corresponding to the temperature range of the transition zone from unstable to stable sliding (Hyndman et al., 1995).

The obtained temperatures for the region where LFEs occur were ranging from 450 °C to 500 °C, which is almost the same as those estimated in our previous study in central Japan (Suenaga et al., 2015). Therefore, LFEs are considered to occur near the down-dip limit of the transition zone.

3.3. Dehydration from the subducting PHS plate

Figs. 2-7 (a), (b), and (c) shows the calculated spatial distributions of water content in

the oceanic crust of the subducting PHS plate at present for the three profiles. In this study, we assumed that the thickness of the oceanic crust is 7 km, and hydrous mid ocean ridge basalt (MORB) consists of hydrous minerals, and investigated the dehydration process along each profile. To calculate temperature and depth dependent water content in hydrous MORB, we used a phase diagram obtained by Omori et al. (2009).

In the region where the SSE occurred along profiles A and B, hydrous MORB is being transformed from blueschist to greenschist metamorphic phases. However, its phase transformation along profile B occurred only at the surface of the oceanic crust, so its dehydration is not so large compared with that along profile A.

In the region where LFEs occur, hydrous MORB in the oceanic crust is transformed from blueshist to greenschist phases along profiles A. On the other hand, no transformations were identified near the region where many LFEs occur along profiles B and C.

We compared the results of the calculated spatial distributions of water content with those of V_p/V_s ratio obtained by seismic tomography (Matsubara and Obara, 2011). The results showed that the region where the phase transformation from blueshist to greenschist occurs along profile A (Fig. 2-1(a)) corresponds well to the region with high V_p/V_s ratio (Fig. 2-8 (a)). On the other hand, high V_p/V_s ratio region were not identified near the plate boundary along profiles B and C (Figs. 2-8(b) and (c)), which are consistent with our results (Figs. 2-7(b) and (c)). Therefore, occurrence of LFEs is considered to be not controlled by dehydration process, but temperature condition at the plate boundary.

4. Conclusions

In this study, we performed 2D numerical simulations to investigate the temperature field and dehydration processes around the strongly coupled region for the anticipated megathrust Tokai earthquake, the regions where the SSE and LFEs occur in the Tokai district. The significant results obtained in this study are summarized as follows:

1. The depth range of the thermally estimated seismogenic zone for the future megathrust earthquake on the upper surface of the PHS plate in the Tokai district is from 8 to 22 km, and the region becomes narrower toward the east.
2. Temperatures for the region where the Tokai SSE occurred at the plate boundary

range from 350 °C to 450 °C, and dehydration associated with the phase transformation from blueschist to greenschist metamorphic phases in the hydrous MORB is expected there as well. However, its dehydration is considered to be not so large on the basis of distributions of V_p/V_s ratio obtained from the seismic tomography. Therefore, temperature condition plays a more significant role than that of dehydration process for the occurrence of SSE.

3. Temperatures for the region where LFEs occur at the plate boundary range from 450 °C to 500 °C. Therefore, LFEs is considered to occur near the down-dip limit of the transition zone.

Acknowledgments

We thank J. Nakajima for providing geometry data of the upper surface of the subducting PHS plate. We also thank M. Matsubara and K. Obara for allowing us to use data of 3D seismic wave velocity structures. All of the data for LFE hypocenters were taken from the Japan Meteorological Agency. All of the figures were created using the Generic Mapping Tools (GMT) developed by Wessel and Smith (1998).

References

Ashi, J., Tokuyama, H., and Taira, A., 2002. Distribution of the methane hydrate BSRs and its implication for the prism growth in the Nankai Trough, Marine Geology 3110,1-15.

Ashi, J., Tokuyama, H., Ujiie, Y., and Taira, A., 1999. Heat flow estimation from gas hydrate BSRs in theNankai Trough, Implications for the thermal structure of the Shikoku Basin. Suppl. EOS Trans., AGU.80 (46), T12A-02.

Burkett, E.R. and Billen, M.I., 2010. Three-dimentionality of slab detachment due to ridge-trench collision: Laterally simultaneous boundinage versus tear propagation. Geochem. Geophys. Geosyst. 11, doi:10.1029/2010GC003286.

Caristan, Y., 1982. The transition from high temperature creep to fracture in maryland diabase. J. Geophys. Res. 87, 6781-6790.

DeMets, C., Gordon, R. G., and Argus, D. F., 2010. Geologically current plate motions. Geophys. J. Int. 181, 1-80.

Hirose, F., Nakajima, J., and Hasegawa, A., 2008. Three-dimensional seismic velocity structure and configuration of the Philippine Sea slab in southwestern Japan estimated by double-difference tomography. J. Geophys. Res. 113, B09315.

Hyndman, R., and Wang K., 1993. Thermal constraints on the zone of possible major thrust earthquake failure on the Cascadia margin. J. Geophys. Res. 98, 2039–2060.

Hyndman, R., Wang, K., and Yamano, M., 1995. Thermal constraints on the seismogenic protion of the southwestern Japan subduction thrust. J. Geophys. Res. 100, 15373-15392.

Ishibashi, K., 1980. Specification of a soon-to-occur seismic faulting in the Tokai district, central Japan, based upon seismotectonics, in Earthquake Prediction. An International Review, Maurice Ewing Series 4, edited by D. W. Simpson and P. G. Richards, 297-332, AGU.

Jolivet, L., Huchon, P., and Rangin, C., 1989. Tectonic setting of Western Pacific marginal basins. Tectonophysics 160, 23–47.

Kato, A., Iidaka, T., Ikuta, R., Yoshida, Y., Katsumata, K., Iwasaki, T., Sakai, S., Thurber, C., Tsumura, N., Yamaoka, K., Watanabe, T., Kunimoto, T., Yamazaki, F., Okubo, M., Suzuki, S., and Hirata, N., 2010. Variations of fluid pressure within the subducting oceanic crust and slow earthquakes. Geophys. Res. Lett. 37, doi:10.1029/2010GL043723.

Katsumata, A. and Kamaya, N., 2003. Low-frequency continuous tremor around the Moho discontinuity away from volcanoes in the southwest Japan. Geophys. Res.

Lett. 30, 1020, doi: 10.1029/2002GRL015981.

Kimura, G., Hashimoto, Y., Kitamura, Y., Yamaguchi, A., and Koge, H., 2014. Middle Miocene swift migration of the TTT triple junction and rapid 4 crustal growth in SW Japan. Tectonics 33, 1219-1238.

Kodaira, S., Iidaka, T., Kato, A., Park, J., Iwasaki, T., and Kaneda, Y., 2004. High pore fluid pressure may cause silent slip in the Nankai trough. Science 304, doi:10.1126/science.1096535 .

Liu, Z., Owen S., Dong D., Lundgren P., Webb F., Hetland E., and Simons M., 2010. Integration of transient strain events with models of plate coupling and areas of great earthquakes in southwest Japan, Geophys. J. Int. 181, 1292-1312.

Matsubara, M. and Obara, K., 2011. The 2011 Off the Pacific Coast of Tohoku earthquake related to a strong velocity gradient with the Pacific plate. Earth Planets Space 63, 663-667.

Matsumoto, T., 2007. Terrestrial heat flow anomaly at non-volcanic area in Southwest Japan based on the NIED Hi-net. Japan Geoscience Union Meeting 2010. T154-001 (in Japanese).

Matsumura, S., 1997. Focal zone of a future Tokai earthquake inferred from the seismicity pattern around the plate interface. Tectonophysics 273, 271-291.

Miyazaki, S., Segall, P., McGuire, J. J., Kato, T., and Hatanaka, Y., 2006. Spatial and temporal evolution of stress and slip rate during the 2000 Tokai slow earthquake. J. Geophys. Res. 111, B03409, doi:10.1029/2004JB003426.

Nakajima, J. and Hasegawa, A., 2007. Subduction of the Phlippine Sea plate beneath southwestern Japan: Slab geometry and its relationship to arc Magmatism. J. Geophys. Res. 112, B08306.

Obara, K., 2002. Nonvolcanic deep tremor associated with subduction in southwest Japan. Science 296, 1679-1681.

Ohta, Y., Kimata, F., and Sagiya, T., 2004. Reexamination of the interpolate coupling in the Tokai region, central Japan, based on the GPS data in 1997-2002. Geophys. Res. Lett. 31, doi:10.1029/2004GL021404.

Omori, S., Kita, S., Maruyama, S., and Santosh, M., 2009. Pressure-temperature conditions of ongoing regional metamorphism beneath the Japanese Islands. Gondwana Res. 16, 458-469.

Ozawa, S., Murakami, M., and Tada, T., 2001. Time dependent inversion study of the slow thrust event in the Nankai trough subduction zone, southwestern Japan. J. Geophys. Res. 106(1) , 787-802.

Ozawa, S., Murakami, M., Kaidzu, M., Tada, T., Sagiya, T., Hatanaka, Y., Yarai, H.,and Nishimura, T., 2002. Detection and monitoring of ongoing aseismic slip in the Tokai region, central Japan. Science 298, 1009-1012.

Sagiya, T., 1999. Interplate coupling in the Tokai district, Central Japan, deduced from continuous GPS data. Geophys. Res. Lett. 26, 2315-2318.

Seno, T., and Yamasaki, T., 2003. Low-frequency tremors, intraslab and interplate earthquakes in Southwest Japan - from a viewpoint of slab dehydration. Geophys. Res. Lett. 30, doi:10.1029/2003GL018349.

Shiono, K., 1988. Seismicity of the SW Japan arc—subduction of the young Shikoku Basin. Modern Geology 12, 449-464.

Suenaga, N., Yoshioka, S., and Matsumoto, T., 2015. Two-dimensional thermal modeling associated with subduction of the Philippine Sea plate in central Japan, and its relationship to the occurrence of interplate earthquakes. Submitted to Journal of geodynamics.

Takahashi, M., 2006. Tectonic development of the Japanese islands controlled by Philippine Sea plate motion. Journal of Geography 115, 116-123 (in Japanese).

Tanaka, A., Yamano, M., Yano, Y., and Sasada, M., 2004. Geothermal gradient and heat flow data in and around Japan, digital geoscience map DGN P-5. Geological Survey of Japan.

Tatsumi, Y., 2006. High-Mg Andesites in the Setouchi Volcanic Belt, Southwestern Japan: Analogy to Archean Magmatism and Continental Crust Formation. Annu. Rev. Earth. Planet. Sci. 34, 467-499.

Wada, I. and Wang, K., 2009. Common depth of slab-mante decoupling: Reconciling diversity and uniformity of subduction zones. Geochem. Geophys. Geosys. 10, doi:10.1029/2009GC002570.

Wang, K., Hyndman, R.D., and Yamano, M., 1995. Thermal regime of the Southwest Japan subduction zone: effects of age history of the subducting plate. Tectonophysics 248, 53-69.

Wessel, P., and Smith, W.H.F., 1998. New, improved version of the generic mapping tools released. EOS Trans. AGU 79, 579.

Yamano, M., 2004. Heat Flow Data in and around Japan, Digital Geoscience Map DGM P-5. Geological Survey of Japan.

Yoshii, T., 1975. Regionality of group velocities of Rayleigh waves in the Pacific and thickening of the plate, Earth Planet. Sci. Lett., 25, 305–312.

Yoshikawa, T. 1974. Denudation and tectonic movement in contemporary Japan. Bull. Dept. Geogr., Univ. Tokyo 6, 1-14.

Yoshioka, S. and Sanshadokoro, H., 2002. Numerical simulations of the deformation and dynamics horizontally lying slabs. Geophys. J. Int. 151, 69-82.

Yoshioka, S., Suminokura, Y., Matsumoto, T., and Nakajima, J., 2013. Two-dimensional thermal modeling of subduction of the Philippine Sea plate beneath southwest Japan. Tectonophysics 608, 1094-1108.

Yoshioka, S., Yabuki, T., Sagiya, T., Tada, T., and Matsu'ura, M., 1993. Interplate coupling and relative plate motion in the Tokai district, Central Japan, deduced from geodetic data inversion using ABIC. Geophys. J. Int. 113, 607-623.

Table 2-1. Values of model parameters

Parameters to calculate temperature fields			
ρ_0 $(\mathrm{kgm^{-3}})$	standard density of the mantle	3400 (1)	
g $(\mathrm{ms^{-2}})$	acceleration of gravity	9.8	
α $(\mathrm{K^{-1}})$	thermal expansivity	2.0×10^{-5} (2)	
C_p $(\mathrm{Jkg^{-1}K^{-1}})$	specific heat at constant pressure	1.046 (1)	
w (km)	thickness of the plate boundary	0.5 (3)	
H_0 $(\mu\mathrm{Wm^{-3}})$	heat generation per unit volume	accretionary prism: 3.0	upper crust: 1.9 (3)
T_0 $(^\circ\mathrm{C})$	potential temperature	1350 (4)	
z_0 (km)	depth below which the effect of adiabatic compression is taken into account at the initial temperature distribution	60	

Parameters to calculate viscosity (5)		diffusion creep	Dislocation creep
d $(\mu\mathrm{m})$	grain size	10000	—
p	grain index	3.0	—
A $(\mathrm{s^{-1}Pa^{-n}\mu m^{p}C_{OH}{}^{-r}})$	coefficient	1.0	9.5×10^{-20}
C_{OH} (ppm)	water content	1000	1000
r	water content index	1.0	1.2
n	stress index	1.0	3.5
E $(\mathrm{kJmol^{-1}})$	activation energy	335	480
V $(\mathrm{m^3mol^{-1}})$	activation volume	4.0×10^{-6}	11×10^{-6}
R $(\mathrm{JK^{-1}mol^{-1}})$	gas constant	8.3	

(1) Yoshioka and Sanshadokoro (2002); (2) Honda (1997); (3) Wang et al. (1995); (4) Takenaka at al. (1999); (5) Burkett and Billen (2010)

Part Ⅲ

Three-dimensional thermal modeling associated with subduction of the Cocos plate beneath southern Mexico, and its relation to the occurrence of interplate seismic events

1.Introduction

In the Pacific side of Mexico, the Cocos plate is subducting beneath the North American plate along the Middle American Trench at the convergence rate of about 6.5 cm/yr (e.g., Demets et al., 2010). In this region, M-8 class megathrust earthquakes such as the 1985 Michoacan earthquake (M8.0) have occurred. The guerrero seismic gap exists along the coastal region, and a megathrust earthquake has been considered to occur there in the near future (Fig. 3-1) (e.g., Suarez and Albini, 2009). Besides, interplate seismic events such as slow slip events (SSEs) and non-volcanic tremors (NVTs) are also observed in southern Mexico (e.g., Payero et al., 2008). In this region, so-called the "flat slab" exists adjacent to the Trans-Mexican volcanic Belt (TMVB), which is a 1000 km long Neogene continental arc. Recent seismic surveys in the Mexico subduction zone (MASE and VEOX) elucidated seismic velocity structures along the two profiles in detail (e.g., Jodicke et al., 2006; Payero et al., 2008), and these data are useful to estimate temperature fields in southern Mexico in association with subduction of the Cocos plate by numerical simulation.

In this region, Currie et al. (2002) estimated seismogenic zone of southern Mexico by performing two-dimensional steady state thermal modeling. Up-dip limit of the seismogenic zone where smectite clays transform to illite and chlorite (100 -150°C) was estimated to be located 15-20 km landward of the Middle American Trench in their numerical simulation. Down-dip limit of the seismogenic zone where quartzo-feldspathic rocks initiate to change its slip mode from velocity weaking to velocity strengthening (320-350°C) was estimated to be located 90-110 km from the trench. They inferred that introduction of frictional heating in numerical simulation is necessary to fit thermally estimated seismogenic zone with observed rapture areas of megathrust earthquakes in southern Mexico. They determined pore pressure ratio of 0.94 for best fitting to observed hea flow data. Wada and Wang (2009) performed

two-dimensional thermal modeling near the northern Mexico, and determined that back-arc heat flow there became 72 $\mathrm{mW/m^2}$, and maximum decoupling depth at the plate interface became about 40 km there. Manea and Manea (2011b) also performed two-dimensional thermal modeling near the Guerrero gap, and suggested that the sediment layers dehydrates about three-quarters of water content above the flat slab at a horizontal distance of about 300 km from the Middle American Trench, and its region corresponds with the region where NVTs occur. Rosas et al. (2015) performed three-dimensional steady-state thermal modeling to investigate flow pattern in the mantle wedge accompanied with geometry variation of the Cocos plate. They also considered hydrothermal circulation in an aquifer in the subducting oceanic crust, and suggested that the effect of hydrothermal circulation reduces interplate temperature in the shallow region. However, three-dimensional unsteady-state realistic thermal modeling, which has temporal variation has not been performed in southern Mexico yet.

In this study, we constructed a three-dimensional thermal convection model in southern Mexico to elucidate relationship among calculated temperature structures, calculated dehydrated water content from the subducting Cocos plate, and above-mentioned interplate seismic events. We used heat flow data of observed Global Heat Flow Database (GHFD) (Jessop et al., 1976) and those estimated from Curie point depths (Manea and Manea, 2011a) to evaluate the validity of the calculated thermal structures.

2. Governing equations

In this study, we used anelastic liquid approximation. As governing equations, we used mass conservation, momentum, and energy equations to calculate the temperature and flow fields. Mass conservation equation can be written by

$$\nabla \cdot \left[\rho_s(z)\mathbf{v}\right] = 0 \,, \tag{3-1}$$

where $\rho_s(z)$ and $\mathbf{v}$ are fluid density and flow velocity vectors, respectively. Subscript denotes adiabatic state. Following Yoshioka and Murakami (2007), the momentum equation can be written as follows:

$$-\frac{\partial P}{\partial x_i} + \frac{\partial \tau_{ij}}{\partial x_j} + Ra\,\alpha(T - T_s)\delta_{i3} = 0 \,, \tag{3-2}$$

where P is pressure deviation from hydrostatic pressure, τ_{ij} is a stress tensor, R_a is

Rayleigh number, α is thermal expansivity, T is temperature, and δ_{ij} is the Kronecher's Delta, respectively. T_s can be written by

$$\frac{dT_s}{dx_3} = Di_z T_s. \tag{3-3}$$

Dissipation number Di_z is given by

$$D_{iz} = \frac{g\alpha D}{C_p}, \tag{3-4}$$

where g is gravity acceleration, D is thickness of the model , and C_p is specific heat at constant pressure, respectively. Viscosity in the model domain is calculated, using Eqs. (1-3) and (1-4). The energy equation is expressed as

$$\rho c_p(\frac{\partial \mathrm{T}}{\partial t} + \mathbf{v}\cdot\nabla T) = k\nabla^2 T + \eta(\nabla v)^2 + \rho g\alpha T v + H_r\rho + Q_f, \tag{3-5}$$

where t is time, k is thermal conductivity, v is a vertical component of flow velocity, H_r is heat generation by a radioactive element, Q_f is frictional heating, respectively. Density ρ is dependent only on temperature, as shown in Eq. (1-7). Frictional heating Q_f can be written by

$$Q_f = Min(\tau_b, \tau_d)\frac{v_t}{w}, \tag{3-6}$$

where τ_b and τ_d are shear stress at the plate boundary in the brittle and ductile regime, respectively, v_t is subducting velocity and w is thickness of plate boundary deforming zone. Shear stress τ_b in the brittle regime (Byerlee, 1978) is written by

$$\tau_b = 0.85\sigma_n(1-\lambda) \ \left(\sigma_n(1-\lambda) \le 200MPa\right), \tag{3-7}$$

$$\tau_b = 50 + 0.6\sigma_n(1-\lambda) \ \ \left(\sigma_n(1-\lambda) \ge 200MPa\right), \tag{3-8}$$

where σ_n is normal stress, and λ is pore pressure ratio. Shear stress in the ductile

regime (Caristan, 1982) can be written by

$$\tau_d = \frac{1}{2} A^{-\frac{1}{n}} \dot{\varepsilon}^{\frac{1}{n}} \exp\left(\frac{E'}{nRT}\right), \tag{3-9}$$

where A is coefficient, $\dot{\varepsilon}$ is the shear strain rate, and E' is the activation energy.

3. Model

Following Ji and Yoshioka (2015), we constructed a 3-D thermal convection model to calculate temperature and flow fields associated with subduction of the Cocos plate. The sizes of the model are 600 km, 600 km, and 300 km in the x-, y-, and z-axis directions, respectively. Number of grids used are 62×62×62 in the model, which are enough for numerical precision. As for the boundaries condition of flow fields, we applied permeable conditions at the boundary of +x, -x, +y, -y, and +z, respectively (Fig. 3-2). Permeable condition can be written as follows:

$$\sigma_{ii} = 0 \qquad (i = x, y, z) \quad , \tag{3-10}$$

where σ_{ii} is normal stress. As for the boundary conditions of temperature fields, we applied adiabatic condition at the boundary of +x, +y, -y, and +z, respectively, the temperature condition of –x is determined by initial temperature condition, and temperature of –z is fixed temperature (0 °C). The initial temperature condition in the model is determined by plate cooling model (Turcotte and Schubert, 2002):

$$T = T_0 + (T_1 - T_0)\left[\frac{z}{d_l} + \frac{2}{\pi}\sum_{n=1}^{\infty}\frac{1}{n}\exp\left(-\frac{\kappa n^2 \pi^2 t}{{d_l}^2}\right)\sin\left(\frac{n\pi z}{d_l}\right)\right], \tag{3-11}$$

where T_0 and T_1 are the surface and the basal temperature of the model, respectively, z is depth, d_l is depth, at which mantle temperature reaches T_1, n is index, κ is thermal diffusivity, and t is the age of the Cocos plate. We used model RT1 (Grose, 2012), in which values of T_1 and d_l were given as 1402 °C and 134.9 km, respectively.

In this study, we evaluated the validity of the estimated thermal structures, by comparing calculated heat flows with observed ones. For heat flow data, we used Global Heat Flow Database (GHFD) (Jessop et al., 1976) and those estimated from Curie point depths of isotherms of 580°C, corresponding to depths, at which the magnet loses its strength (Manea and Manea, 2011a). The root mean square values between observed and calculated ones were estimated as follows:

$$S = \frac{1}{M+N}\left[\sum_{i=1}^{M+N}(O_i - C_i)^2\right]^{\frac{1}{2}}, \tag{3-12}$$

where O_i and C_i are the observed and calculated heat flow values, respectively, M and N are the total number of data points of GHFD and those estimated from Curie point depths, respectively.

We performed numerical simulation during the period from 15 Ma to the present. As for the age of the Cocos plate at the trench, it was given as follows;

$$t_{trench} = t_{ini} + t_{calc} \ , \tag{3-13}$$

where t_{ini} is initial age of the Cocos plate at the trench, corresponding to the present age of the Cocos plate minus calculation period (15 Myr), and t_{calc} is calculation time. The shape of the subducting Cocos plate is defined by Pardo and Suarez, 1995; Pérez-Campos et al., 2008; Yang et al., 2009; Melgar and Pérez-Campos, 2011.

4. Results and discussion

4-1. Parameter dependency

To evaluate parameter dependency in our numerical simulation, we performed several numerical simulations, and compared temperature, flow fields, dehydrated water content, and heat flow among them.

First, to investigate parameter dependency in the numerical simulation, we determined model parameters of the standard model as follows:

The present age of the Cocos plate at the Middle American Trench: 15.0 Myr

Pore pressure ratio: 1.00

Continental crust thickness: 32 km (upper crust: 16 km, lower crust: 16 km)

Subducting velocity at the Middle American Trench: 5.5cm/yr~6.8cm/yr (Demets et

al., 2010).

When we estimated the dehydration processes within the subducting Cocos plate, we used a phase diagram of harzburgite, which is one of the dominant minerals in the upper mantle (Hacker et al., 2003), and hydrous MORB in an oceanic crust of the Cocos plate (Omori et al., 2009).

Then, we varied values of the above-described parameters to investigate influence on the interplate temperature, flow fields in the mantle wedge, dehydrated water content, and heat flow. The interplate temperature, flow fields, dehydration process, and heat flow for the standard model are shown in Figs. 3-3 (a), (b), (c), and (d), respectively.

4-1-1. Parameter dependency on the age of the Cocos plate

As for the age of the subducting Cocos plate at the trench, the present age of the worldwide ocean floor has been investigated well (Muller et al., 2008), and we determined the age of the Cocos plate using Eq. (3-13). However, to construct more realistic model, subduction history of the Cocos plate from the past to the present should be considered.

As a previous study of subduction history of the Cocos plate, Manea et al. (2013) suggested that the Cocos plate had been formed apart from the Farallon plate, which was caused by the East Pacific Rise at approximately 23 Ma. Then, the Cocos plate has moved and rotated between the East Pacific rise and the Middle American Trench (Meschede and Barckhausen, 2000). In this study, we have not yet introduced the effect of the plate motion in our numerical simulations. So, we just investigated its dependency on temperature and flow fields.

We changed the age of the Cocos plate at the Middle American Trench from 15 Myr to 30 Myr. The interplate temperature, flow fields, dehydrated water content, and heat flow of this model are shown in Figs. 3-4 (a), (b), (c), and (d), respectively. Comparing the latter model with the standard model, interplate temperature (Fig. 3-4 (a)) was almost unchanged. Flow fields in the mantle wedge (Fig. 3-4 (b)) were the same flow pattern as those of the standard model. Dehydrated water content (Fig. 3-4 (c)) also did not change so much between them. The region where dehydrated water content is over 3 wt% is ranging from the horizontal distance of 250 km to 340 km from the trench. Heat flow distributions between the two models were almost the same.

4-1-2. Parameter dependency in frictional heating on the plate interface

As for pore pressure ratio, which is used to calculate shear stress at the plate boundary, it is predominant parameter for frictional heating. As described in part Ⅰ and Ⅱ,

interplate temperature was remarkably affected by frictional heating. So, in this section, we investigated its dependency on temperature and flow fields.

We changed pore pressure ratio in Eq. (3-7) and (3-8) from 1.00 to 0.95. The interplate temperature, flow fields, dehydrated water content, and heat flow of the latter model are shown in Figs. 3-5 (a), (b), (c), and (d), respectively. Interplate temperature near the flat slab became about 100 – 150 $^{\circ}$C higher than that of the standard model (Fig. 3-5 (a)). Flow fields in the mantle wedge (Fig. 3-5 (b)) did not change so much as compared with those of the standard model. The dehydrated water content changed about twice in amount because of the increase in the interplate temperature. The region where dehydrated water content is over 3 wt% is ranging from the horizontal distance of 90 km to 360 km from the trench. Heat flow in the flat slab region was about 10mW/ m^2 higher than that of standard model.

4-1-3. Parameter dependency on the thickness of the North American plate

However the thickness of the continental crust is uneven in southern Mexico (e.g., Ferrari et al., 2011), it is difficult to introduce such a uneven shape of the continental crust in our model because of the technical problem of calculation of flow fields. So, we investigated its dependency to temperature and flow fields. We changed the thickness of the continental crust from 32 km to 50 km (upper crust: 25 km, lower crust: 25 km). The interplate temperature, flow fields, dehydrated water content, and heat flow of the latter model are shown in Figs. 3-6 (a), (b), (c), and (d), respectively. Interplate temperature near the flat slab of this model became lower than that of the standard model slightly. Flow velocity vectors in the mantle wedge changed a little. However, flow pattern there was the same as that for the standard model. Dehydrated water content for this model was almost the same as that of the standard model. The region where dehydrated water content is over 3 wt% is ranging from the horizontal distance of 250 km to 340 km from the trench. Heat flow beyond the flat slab region was about 5 mW/ m^2 lower than that of standard model.

4-1-4. Parameter dependency on subducting velocity of the Cocos plate

As described in section 4-1-1, subduction history of the Cocos plate has been discussed in previous study. The past subducting velocity of the Cocos plate might differ from the present one. So, here we investigated its dependency on temperature and flow fields.

We changed subducting velocity at the Middle American Trench from 5.5~ 6.8 cm/yr (Demets et al., 2010) to half of those at each grid in numerical calculation. Temperature,

flow fields, dehydrated water content, and heat flow of this model are shown in Figs. 3-7 (a), (b), (c), and (d), respectively. Interplate temperature near the flat slab region became about 30-50 ˚C lower than that of the standard model in the shallow region ranging from 0 km to 200km in the horizontal distance from the trench. It seems that flow in the mantle wedge became weak because of the slow subducting velocity, and hot mantle materials had not include in the shallow region ranging from 0 km to 200km in the horizontal distance from the trench.

4-2. Most suitable model

In section 4-1, we confirmed parameter dependency for several parameters. The predominant parameters to temperature fields and heat flow among them were pore pressure ratio λ, thickness of the continental crust, and subducting velocity of the Cocos plate, but subducting velocity at the present can be determined uniquely, using Euler parameters (e.g., Demets et al., 2010). Therefore, we took pore pressure ratio λ and the thickness of the continental crust as unknown parameters to determine most suitable model.

In the most suitable model, the subducting velocities along the Middle American Trench were given, referring to Demets et al. (2010), which range from 5.5 cm/yr to 6.8 cm/yr in the model region. The age of the Cocos plate at the Middle American Trench was given, referring to Manea and Manea (2011b), and set to be 14.0 Myr in the western region of the Orozco fracture zone (longitude: 101.7° W, latitude:16.85° N), and 17 Myr in the eastern region.

In this study, we used heat flow data to evaluate calculated temperature structures, using Eq. (3-12). Value range of pore pressure ratio (Fig. 3-8) was determined based on heat flow in the shallow region whose depth is ranging from 0 km to 32 km, corresponding to the thickness of the continental crust in the standard model. Currie et al. (2002) estimated pore pressure ratio of 0.94 in Mexico, using a 2D thermal convection model of subduction of the Cocos plate. However, when we used pore pressure ratio of 0.94 in our model, calculated heat flow became too high as compared with observed data of GHFD. Value range of the thickness of the Cocos plate was determined, referring to Ferrari et al. (2011). The thickness of the North American plate near the Mexico city in the TMVB is over 50 km, and it became thinner as going to the coast. It was less than 25 km near the coastline in our model region. Then, we determined most suitable value for pore pressure ratio and the thickness of the continental crust as 0.96 and 40 km in southern Mexico to minimize S value in Eq. (3-12) (Fig. 3-8). Comparison of heat flow between estimated one from the Curie point

depths of isotherms of 580 ˚C and calculated one of most suitable model is shown in Fig. 3-9. Comparison of heat flow between observed data of GHFD and calculated one is shown in Fig. 3-10. When we calculate Eq. (3-12), we excluded observed data of over 90 mW/m^2, because these high heat flow region (e.g., Fig. 3-9 (a)) may be affected by underground magmatism, which is not considered in our modeling.

Interplate temperature of the most suitable model together with rapture areas of past megathrust earthquakes in southern Mexico are shown in Fig. 3-11. Interplate temperature of the up-dip and the down-dip limits of the seismogenic zone were estimated to be ranging approximately 100 ˚C and 400 ˚C, respectively. The temperature range (Fig. 3-11) is somewhat larger than that of 100-150 ˚C to 350 ˚C by Hyndman and Wang (1993) in other subduction zones, which was estimated from laboratory experiments of phase transformation of minerals within the subducting plate. As one possible reason for its difference, interplate temperature or heat flow may be affected by hydrothermal circulation of dehydrated water, whose effect was indicated in southern Mexico (e.g., Manea and Manea, 2011b).

As for SSE occurring region, we followed Radiguet et al. (2012). The regions where cumulative slip during the last three SSEs in southern Mexico, in which occurred from 2001 to 2002, 2006, and from 2009 to 2010, respectively, are shown in Fig. 3-11. We took the region where cumulative slip during the last three SSEs exceeds 30 cm as a SSEs occurring region. Interplate temperature at the plate boundary there is ranging from about 480 ˚C to 680 ˚C.

Interplate temperature on the flat slab where NVTs occur above there (Payero et al., 2008) is ranging from 630 ˚C to 830 ˚C. These temperature ranges were about 100 ˚C higher than those of Rosas et al. (2015). They introduced hydrothermal circulation effect in their three-dimensional thermal modeling in southern Mexico by solving Nusselt number, and suggested that its effect reduces interpolate temperature as much as 100 ˚C.

Distributions of water content of MORB at the plate boundary and dehydrated water content within the subducting plate are shown in Figs. 3-12 (a) and (b), respectively. Major dehydration whose dehydrated water content is over 3 % initiates near the region where NVTs occur, and dehydration appears to continue as far as the flat slab exists (Fig. 3-12 (b)). About a half of water content near the flat slab region was dehydrated in the Cocos plate (Fig. 3-12 (b)). This is consistent with previous results of Manea and Manea (2011b).

Comparing our results with interplate temperature and dehydration process where interpate seismic events such as LFEs and SSEs occurred estimated in Parts Ⅰ and Ⅱ,

interplate temperature where these seismic events occurred in southern Mexico is about 150 - 200°C higher than that estimated in central Japan. This difference is mainly because estimated frictional heating on plate interface, which depends on value of pore pressure ratio is higher than that estimated in central Japan. However, as a common feature among them, dehydration from the subducting plate estimated to be maximum near the region where above-mentioned interplate seismic events occurred.

5. Conclusions

In this study, we performed three-dimensional thermal modeling in southern Mexico to investigate the occurrence mechanisms of interplate seismic events there. In addition, using a phase diagram of harzburgite and hydrous MORB, we examined the dehydration process associated with subduction of the Cocos plate. The significant results obtained in this study can be summarized as follows:

(1) The most predominant value to influence on interplate temperature is pore pressure ratio. When pore pressure ratio is set to be 0.95, interplate temperature in shallow region is about 100 - 150 °C higher than that of the model with pore pressure ratio of 1.00.
(2) Interplate temperature of the seismogenic zone in southern Mexco was estimated to be ranging from 100 °C to 400 °C.
(3) Interplate temperature where SSEs occur was estimated to be ranging from 480 °C to 680 °C.
(4) Interplate temperature where NVTs occur was estimated to be ranging from 630 °C to 830 °C.
(5) About a half of water content was estimated to be dehydrated within the subducting Cocos plate near the flat slab region.

Acknowledgments

We thank M. Manea and V. Manea for providing geometry data of the upper surface of the subducting Cocos plate, data of curie point depth distributions in southern Mexico, and data for NVT hypocenters in Guerrero.

References

Byerlee, J., D., 1978. Friction of Rocks. Pure and Applied Geophysics 116 (4-5), 615–626.

Caristan, Y., 1982. The transition from high temperature creep to fracture in maryland diabase. J. Geophys. Res. 87, 6781-6790.

Currie, C., Hyndman, R., Wang, K., and Kostoglodov, V., 2002. Thermal models of the Mexico subduction zone: Implications for the megathrust seismogenic zone. Journal of Geophys. Res. 107, NO. B12, 2370, doi:10.1029/2001JB000886.

DeMets, C., Gordon, R. G., and Argus, D. F., 2010. Geologically current plate motions. Geophys. J. Int. 181, 1-80.

Ferrari, L., Orozco-Esquivel, T., Manea, V., and Manea, M., 2011. The dynamic history of the Trans-Mexican Volcanic Belt and the Mexico subduction zone. Tectonophysics 522-523, 122-149.

Hacker, B., Peacock, S., Abers, G., and Holloway, S., 2003. Are intermediate-depth earthquakes in subducting slabs linked to metamorphic dehydration reactions? J. Geophys. Res. 108, doi:10.1029/2001JB001129.

Jessop, A., Hobart, M., Sclater, J., 1976. The world heat flow data-1975. Geothermal series number 5, Ottawa, Canada.

Ji, Y. and Yoshioka S., 2015. Effects of slab geometry and obliquity on the interplate thermal regime associated with the subduction of three-dimensionally curved oceanic plates. Geoscience Frontiers 6, 61-78.

Jodicke, H., Jording, A., Ferrari, L., Arzate, J., Mezger, K., and Rupke, L., 2006. Fluid release from the subducted Cocos plate and partial meltingof the crust deduced from magnetotelluric studies in southern Mexico:Implications for the generation of volcanism and subduction dynamics. J. Geophys. Res. 111, B08102, doi:10.1029/2005JB003739.

Manea, M., and Manea, V., 2011a. Curie Point Depth Estimates and Correlation with Subduction in Mexico. Pure and Applied Geophysics 168, 1489-1499.

Manea, V., and Manea, M., 2011b. Flat-slab thermal structure and evolution beneath central Mexico. Pure and Applied Geophysics 168, 1475-1487.

Manea, V., Manea, M., and Ferrari, L, 2013. A geodynamical perspective on the subduction of Cocos and Rivera plates beneath Mexico and Central America. Tectonophysics 609, 56-81.

Melgar, D., Pérez-Campos, X., 2011. Imaging the Moho and subducted oceanic crust at the Isthmus of Tehuantepec, Mexico, from receiver functions. Pure and Applied Geophysics 168, 1449–1460. doi:10.1007/s00024-010-0199-5.

Mechede, M., and Barckhausen, U., 2000. Plate tectonic evolution of the Cocos-Nazca spreading center. Proceedings of the Ocean Drilling Program, Scientific Results 170.

Müller, R.D., M. Sdrolias, C. Gaina, and W.R. Roest 2008. Age, spreading rates and spreading symmetry of the world's ocean crust, Geochem. Geophys. Geosyst., 9, Q04006, doi:10.1029/2007GC001743.

Omori, S., Kita, S., Maruyama, S., and Santosh, M., 2009. Pressure-temperature conditions of ongoing regional metamorphism beneath the Japanese Islands. Gondwana Res. 16, 458-469.

Pardo, M., and Suárez, G., 1995. Shape of the subducted Rivera and Cocos plate in southern Mexico: seismic and tectonic implications. Journal of Geophys. Res. 100, 12, 357–12 , 373. doi:10.1029/95JB00919..

Payero, S., Kostoglodov, V., Shapiro, N., Mikumo, T., Iglesias, A., Perez-Campos, X., and Clayton, R., 2008. Nonvolcanic tremor observed in the Mexican subduction zone. Geophys. Res. Lett. Solid Earth 35, doi:10.1029/2007GL032877.

Pérez-Campos, X., Kim, Y., Husker, A., Davis, P.M., Clayton, R.W., Iglesias, A., Pacheco, J.F., Singh, S.K., Manea, V.C., and Gurnis, M., 2008. Horizontal subduction and truncation of the Cocos Plate beneath central Mexico. Geophysical Research Letters 35, L18303. doi:10.1029/2008GL035127.

Radiguet, M., Cotton, F., Vergnolle, M., Campillo, M., Walpersdorf, A., Cotte, N., and Kostoglodov, V., 2012. Slow slip events and strain accumulation in the Guerrero gap, Mexico. Journal of Geophys. Res. 117, doi:10.1029/2011JB008801.

Suarez,G., and Albini, P., 2009. Evidence for Great Tsunamigenic Earthquakes (M 8.6) along the Mexican Subduction Zone. Bulletin of the Seismological Society of America 99, No. 2A, 892–896.

Turcotte, D., and Schubert, G., 2002. Geodynamics: Second Edition. Cambridge University Press, New York, 249-254.

Wada, I. and Wang, K., 2009. Common depth of slab-mante decoupling: Reconciling diversity and uniformity of subduction zones. Geochem. Geophys. Geosys. 10, doi:10.1029/2009GC002570.

Yang, T., Grand, S.P.,Wilson, D., Guzmán-Speziale, M., Gómez-González, J. M., Domínguez-Reyes, T., and Ni, J., 2009. Seismic structure beneath the Rivera subduction zone from finite-frequency seismic tomography. Journal of Geophys. Res. 114, B01302.doi:10.1029/2008JB005830.

Yoshioka, S. and Murakami, K., 2007. Temperature distribution of the upper surface of the subducted Philippine Sea plate along the Nankai Trough, southwest Japan,

from a three-dimentional subduction model: relation to large interpolate and low-frequency earthquakes. Geophys. J. Int. 171, 302-315.

Figures (Part Ⅰ～Ⅲ)

Figures (Part Ⅰ)

(Figure 1-1 ～ Figure 1-12)

Figure 1-1

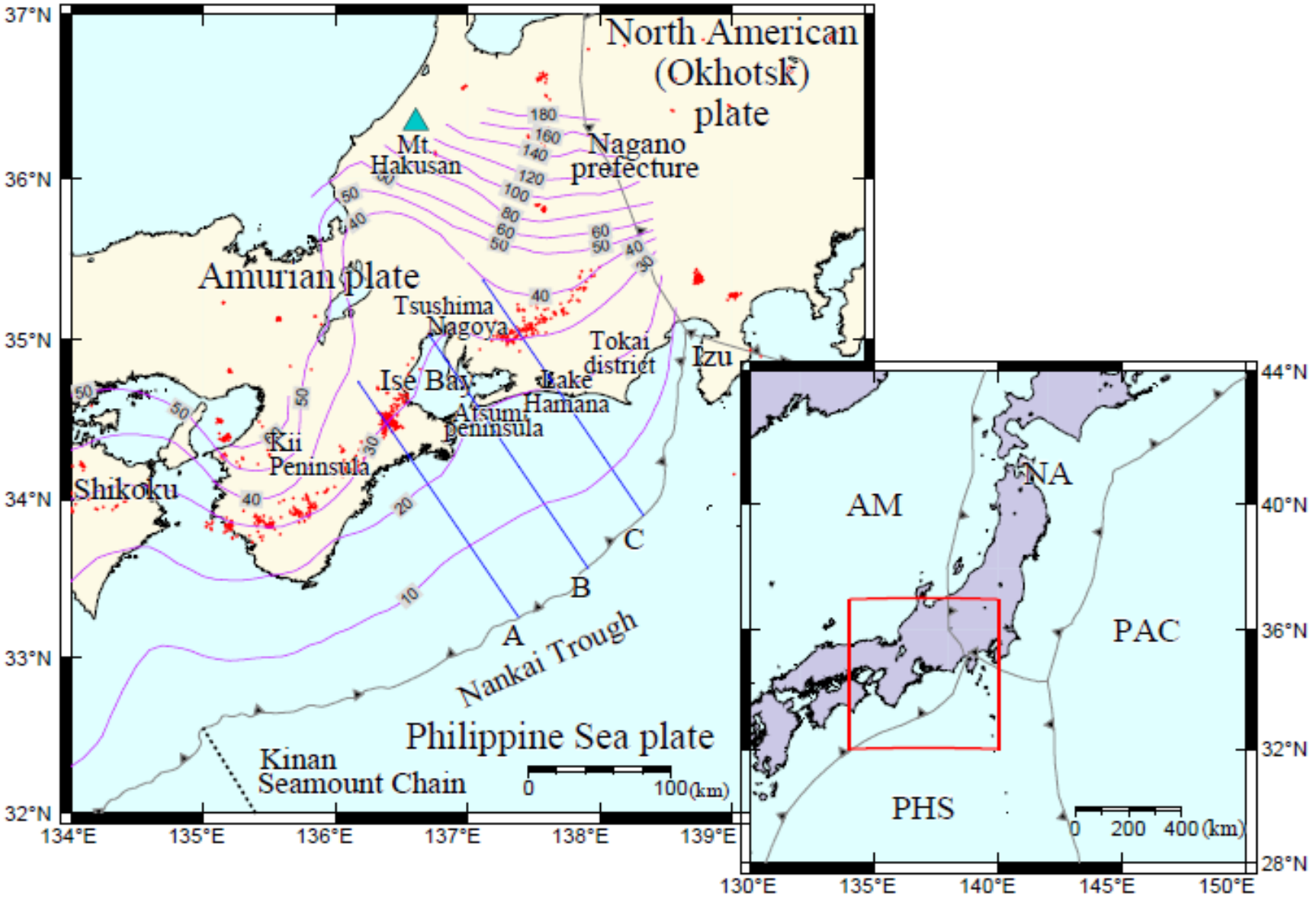
North American (Okhotsk) plate
Amurian plate
Philippine Sea plate
Mt. Hakusan
Nagano prefecture
Tsushima
Nagoya
Tokai district
Izu
Ise Bay
Lake Hamana
Atsumi peninsula
Kii Peninsula
Shikoku
Nankai Trough
A
B
C
Kinan Seamount Chain
0 100(km)
AM
NA
PAC
PHS
0 200 400(km)
37°N
36°N
35°N
34°N
33°N
32°N
134°E
135°E
136°E
137°E
138°E
139°E
44°N
40°N
36°N
32°N
28°N
130°E
135°E
140°E
145°E
150°E

Figure 1-2

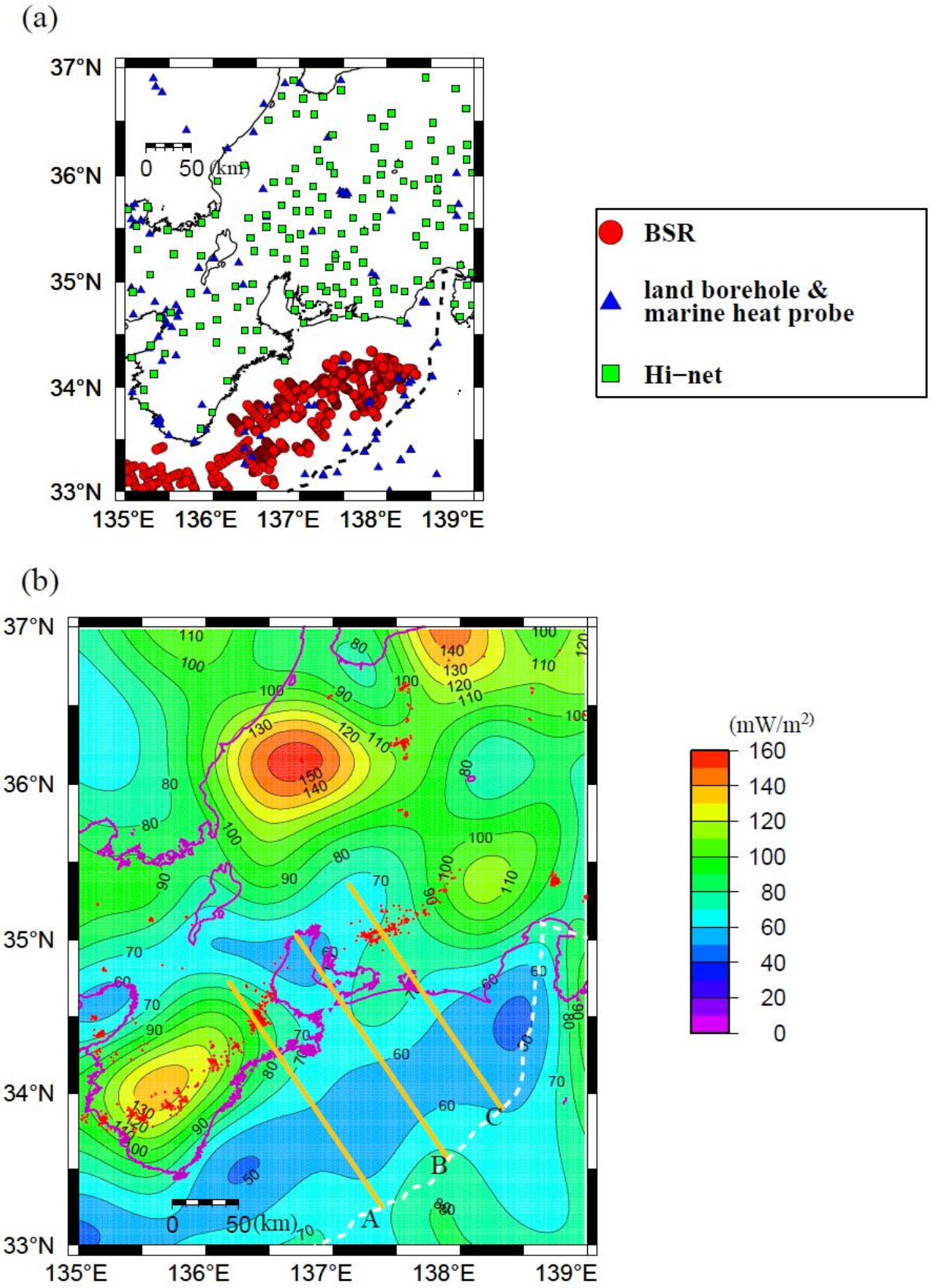
(a)
37°N
36°N
35°N
34°N
33°N
135°E
136°E
137°E
138°E
139°E
0
50 (km)
BSR
land borehole &
marine heat probe
Hi−net
(b)
37°N
36°N
35°N
34°N
33°N
135°E
136°E
137°E
138°E
139°E
0
50 (km)
A
B
C
(mW/m2)
160
140
120
100
80
60
40
20
0

Figure 1-3

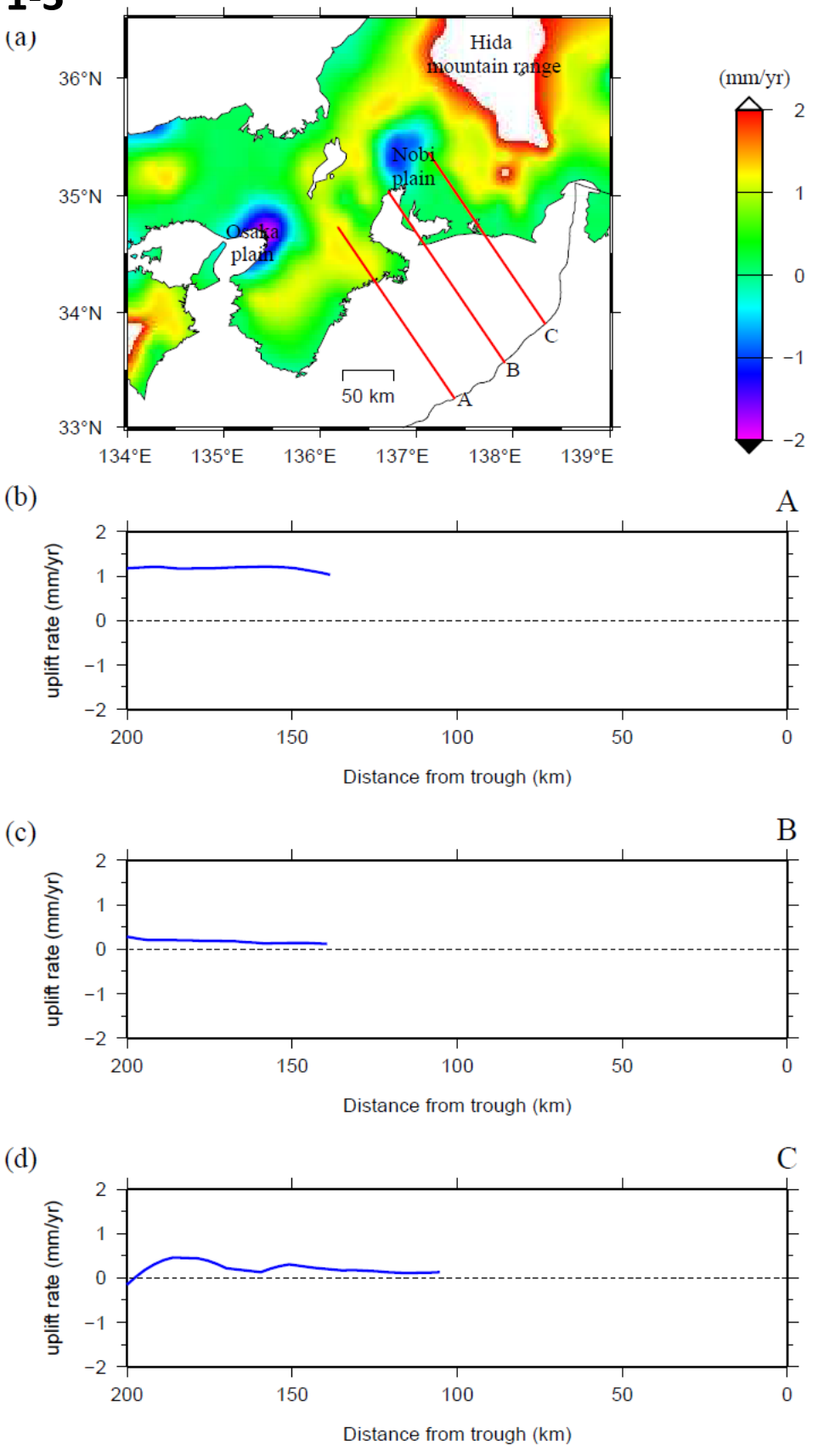
(a)
Hida
mountain range
Nobi
plain
Osaka
plain
36°N
35°N
34°N
33°N
134°E
135°E
136°E
137°E
138°E
139°E
50 km
A
B
C
(mm/yr)
2
1
0
−1
−2
(b)
A
uplift rate (mm/yr)
Distance from trough (km)
(c)
B
uplift rate (mm/yr)
Distance from trough (km)
(d)
C
uplift rate (mm/yr)
Distance from trough (km)

Figure 1-4

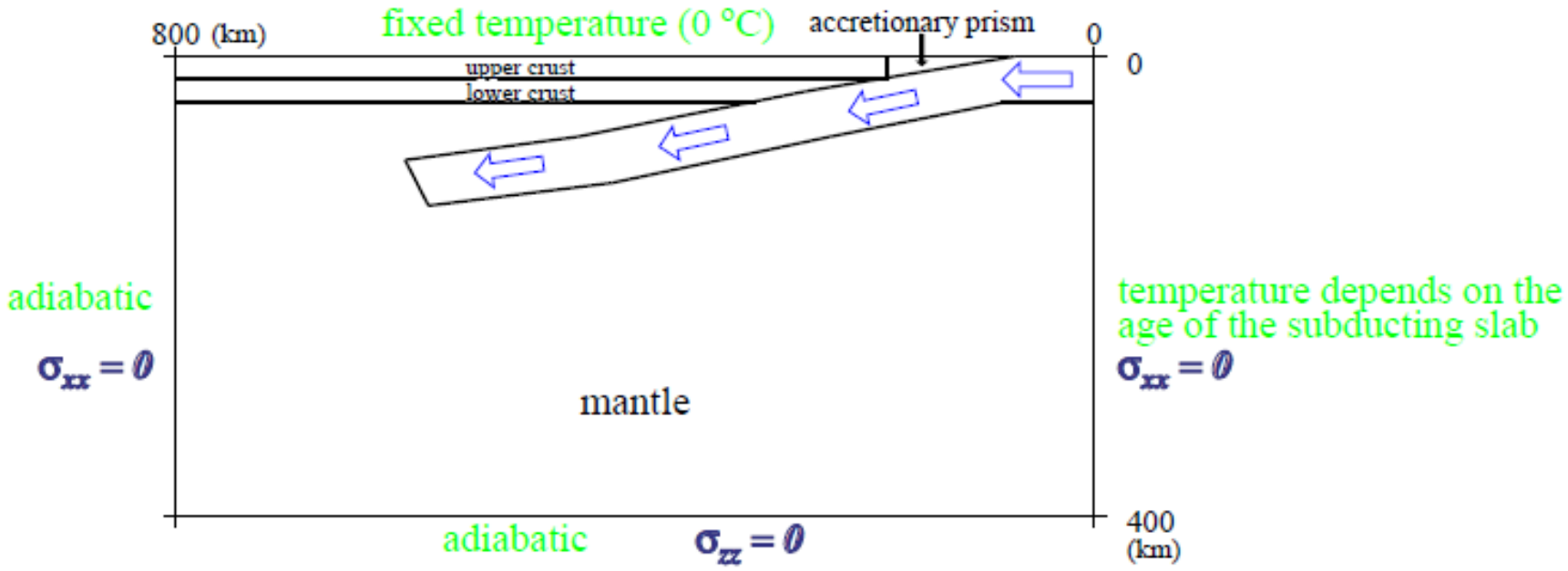
800 (km)
fixed temperature (0 °C)
accretionary prism
0
0
upper crust
lower crust
adiabatic
$\sigma_{xx} = 0$
temperature depends on the age of the subducting slab
$\sigma_{xx} = 0$
mantle
adiabatic
$\sigma_{zz} = 0$
400 (km)

Figure 1-5

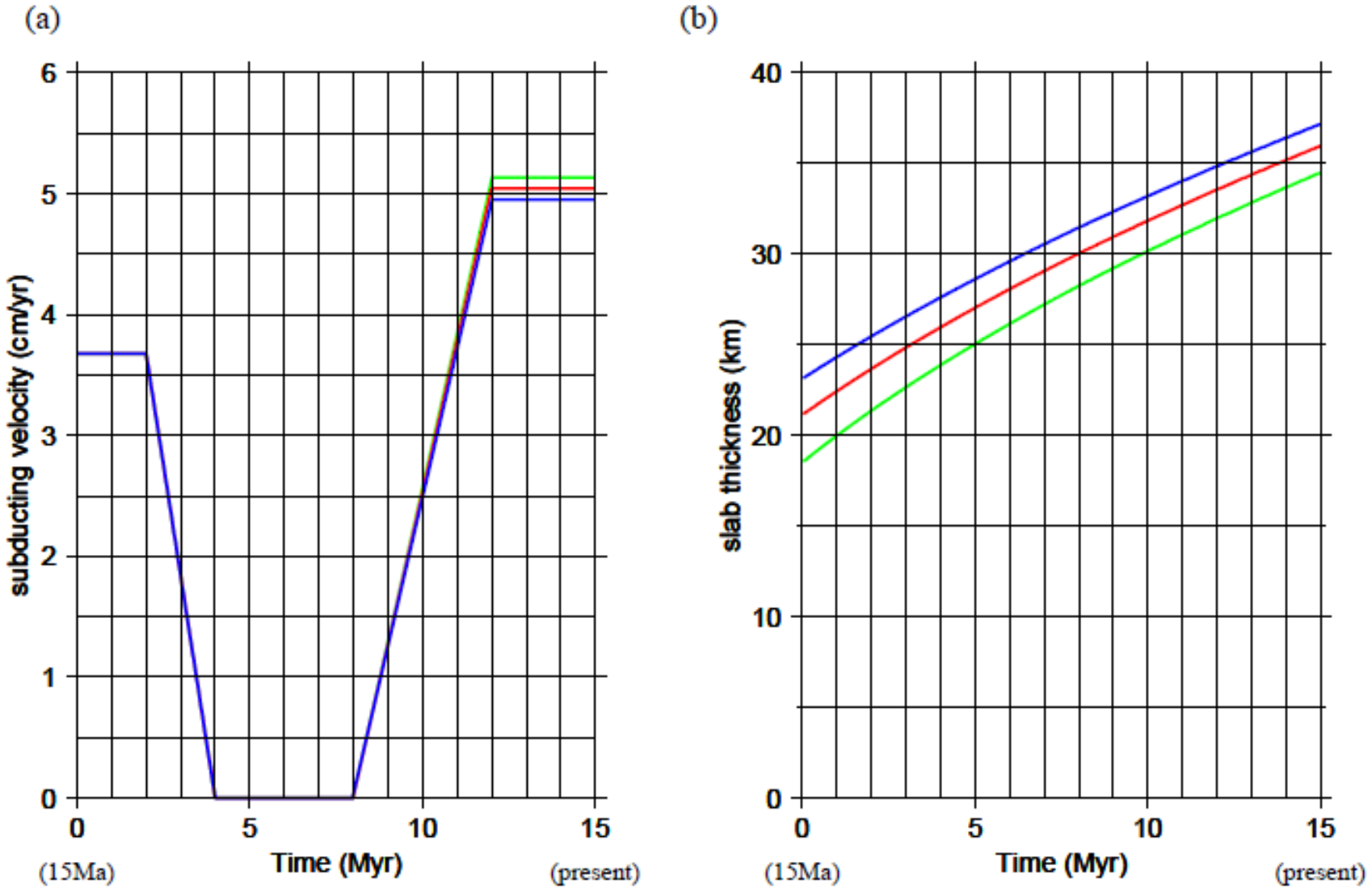
(a)
subducting velocity (cm/yr)
0
1
2
3
4
5
6
0
5
10
15
(15Ma)
Time (Myr)
(present)
(b)
slab thickness (km)
0
10
20
30
40
0
5
10
15
(15Ma)
Time (Myr)
(present)

Figure 1-6

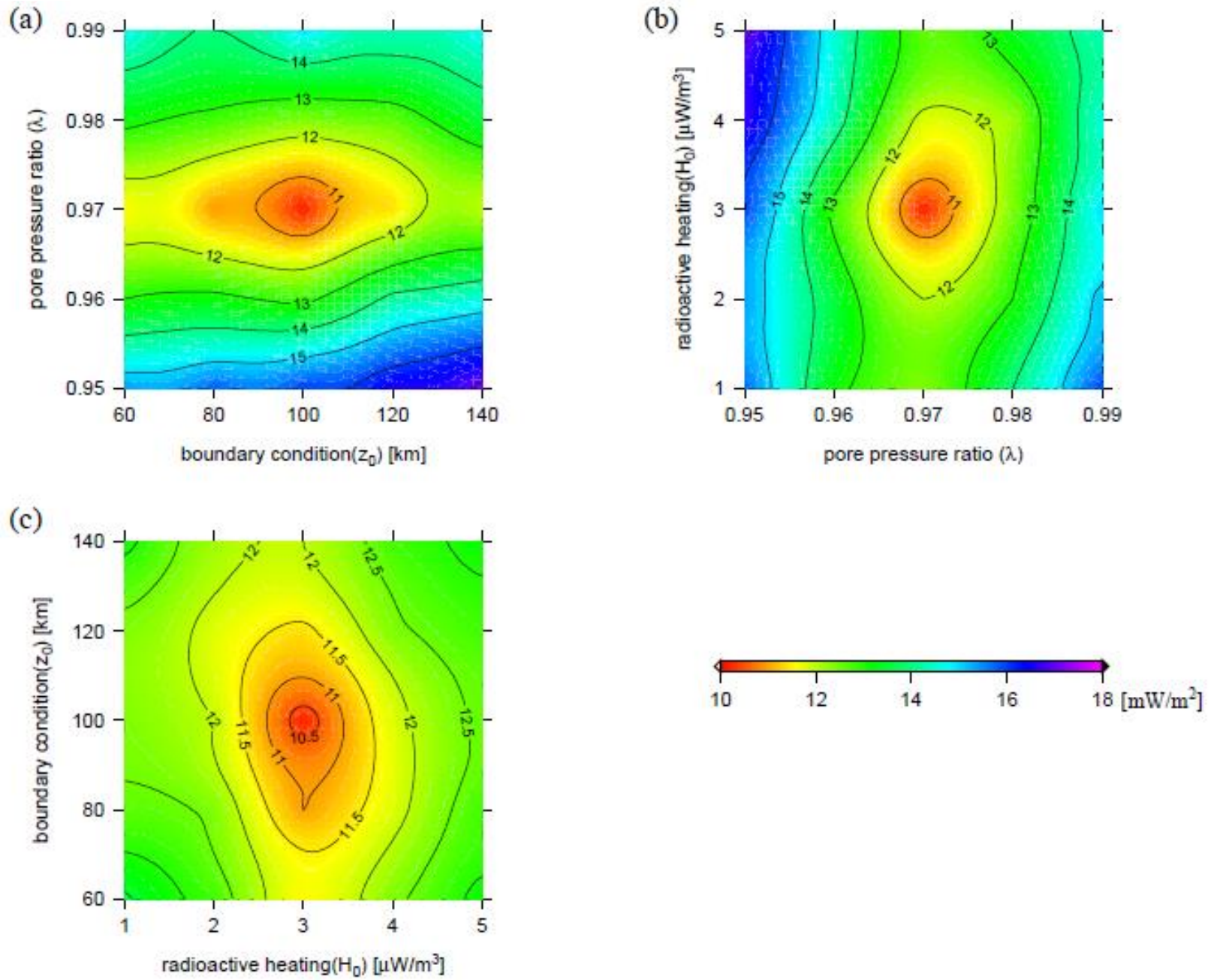
(a)
pore pressure ratio (λ)
boundary condition(z_0) [km]
(b)
radioactive heating(H_0) [μW/m^3]
pore pressure ratio (λ)
(c)
boundary condition(z_0) [km]
radioactive heating(H_0) [μW/m^3]
10 12 14 16 18 [mW/m^2]

Figure 1-7

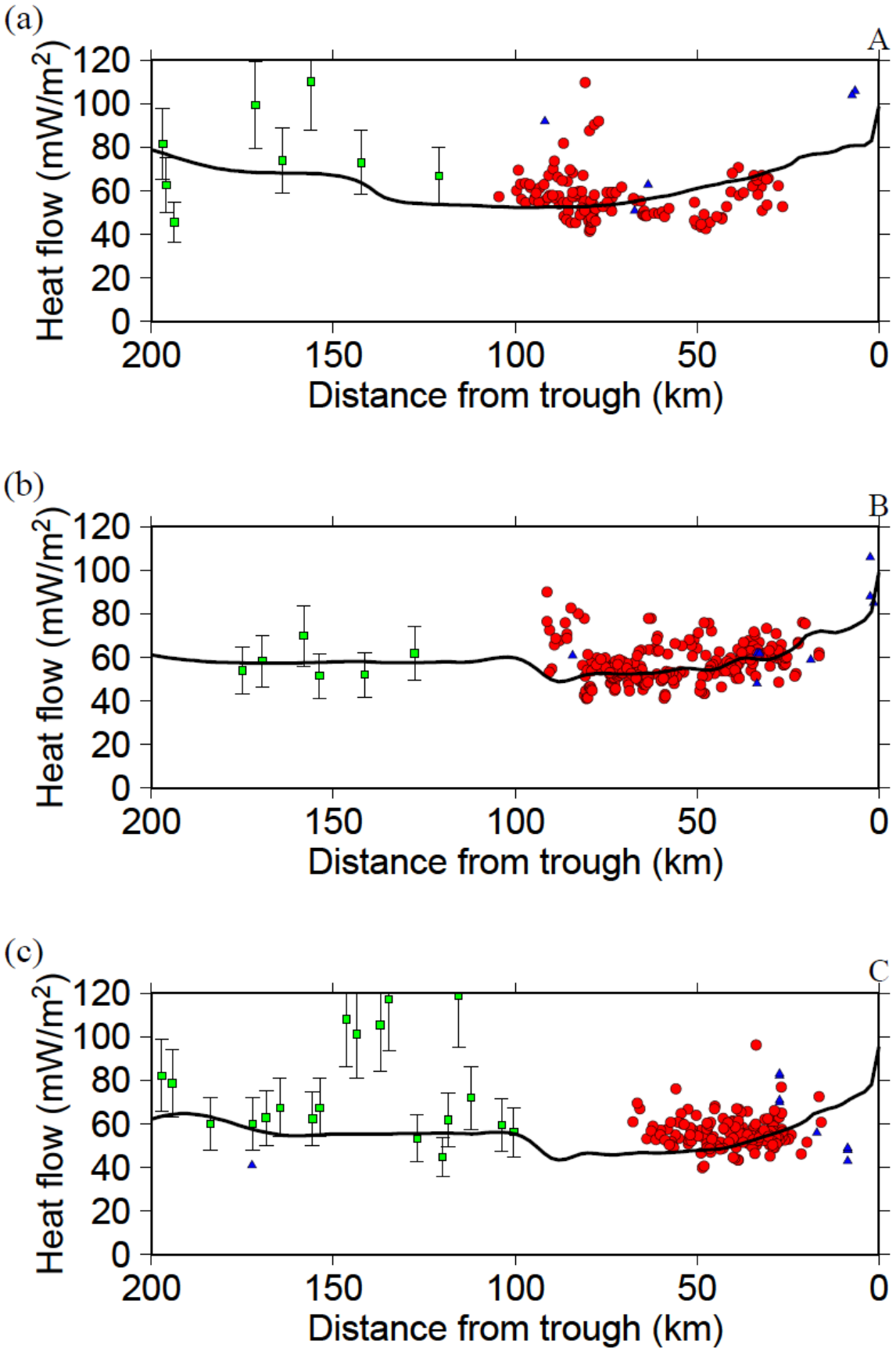
(a)
A
Heat flow (mW/m²)
120
100
80
60
40
20
0
200
150
100
50
0
Distance from trough (km)
(b)
B
Heat flow (mW/m²)
120
100
80
60
40
20
0
200
150
100
50
0
Distance from trough (km)
(c)
C
Heat flow (mW/m²)
120
100
80
60
40
20
0
200
150
100
50
0
Distance from trough (km)

Figure 1-8

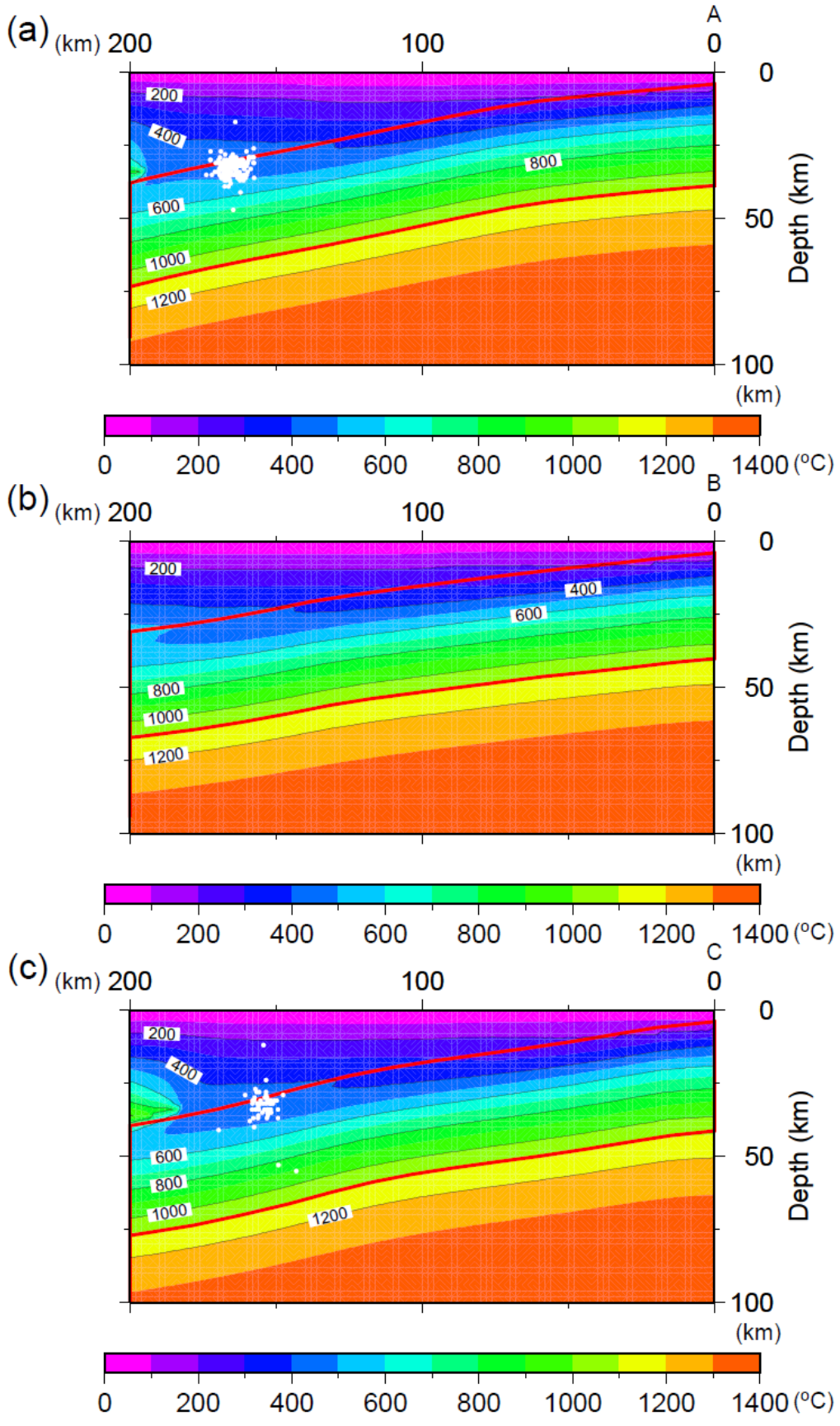
(a)
(km) 200
100
A
0
0
50
100
Depth (km)
(km)
200
400
600
800
1000
1200
0
200
400
600
800
1000
1200
1400
(°C)
(b)
(km) 200
100
B
0
0
50
100
Depth (km)
(km)
200
400
600
800
1000
1200
0
200
400
600
800
1000
1200
1400
(°C)
(c)
(km) 200
100
C
0
0
50
100
Depth (km)
(km)
200
400
600
800
1000
1200
0
200
400
600
800
1000
1200
1400
(°C)

Figure 1-9

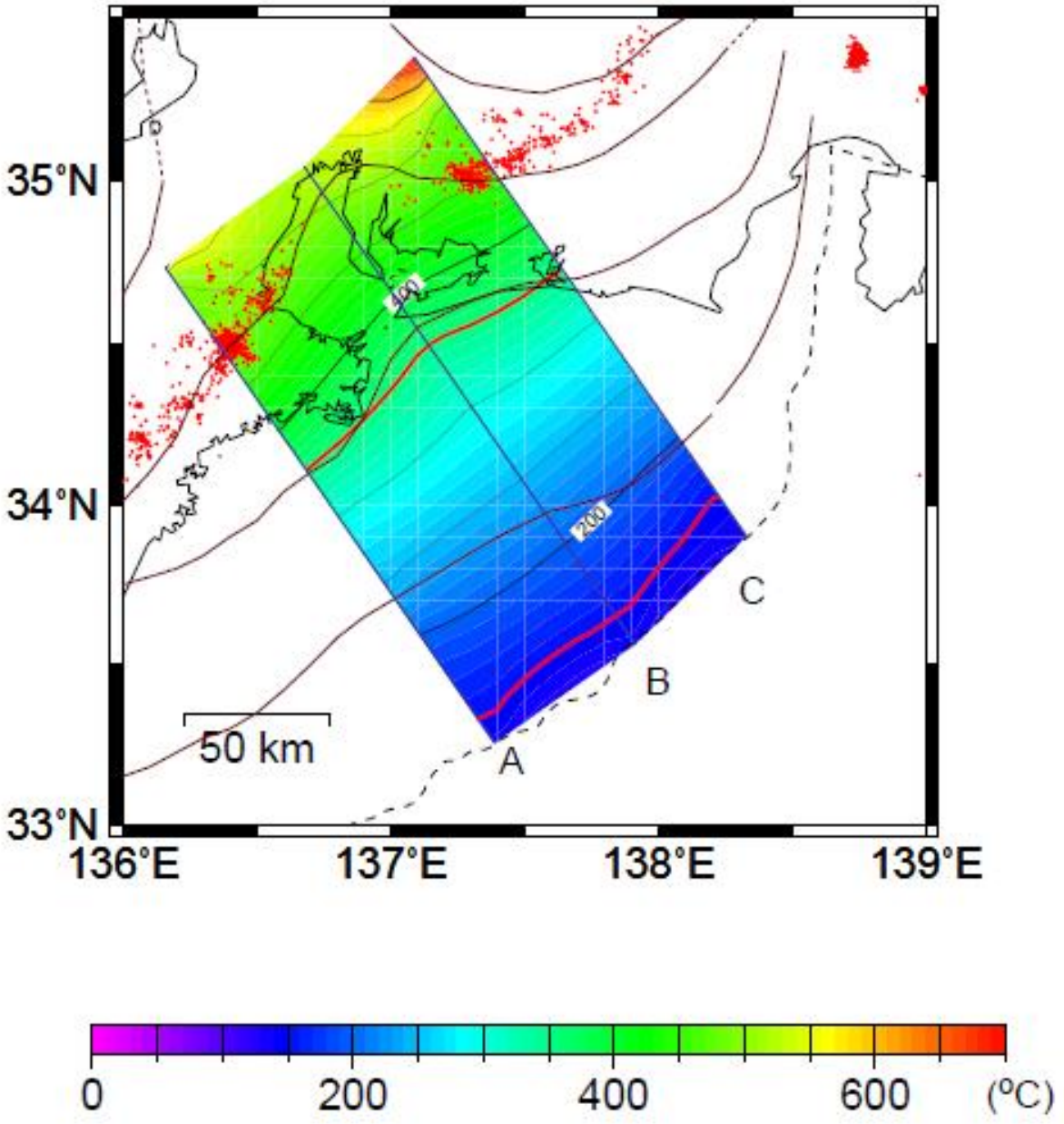

Figure 1-10

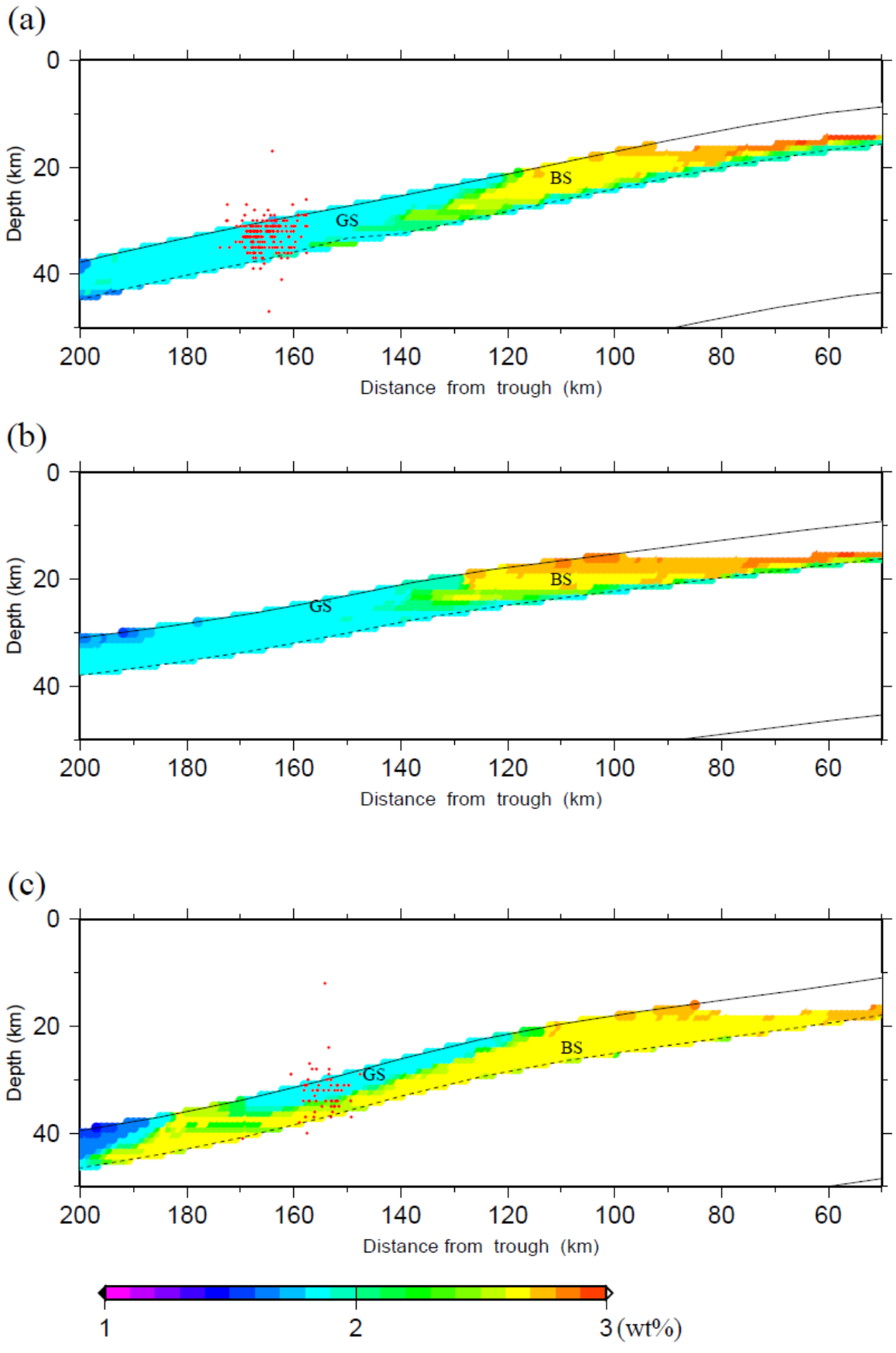
(a)
Depth (km)
0
20
40
GS
BS
200
180
160
140
120
100
80
60
Distance from trough (km)
(b)
Depth (km)
0
20
40
GS
BS
200
180
160
140
120
100
80
60
Distance from trough (km)
(c)
Depth (km)
0
20
40
GS
BS
200
180
160
140
120
100
80
60
Distance from trough (km)
1
2
3 (wt%)

Figure 1-11

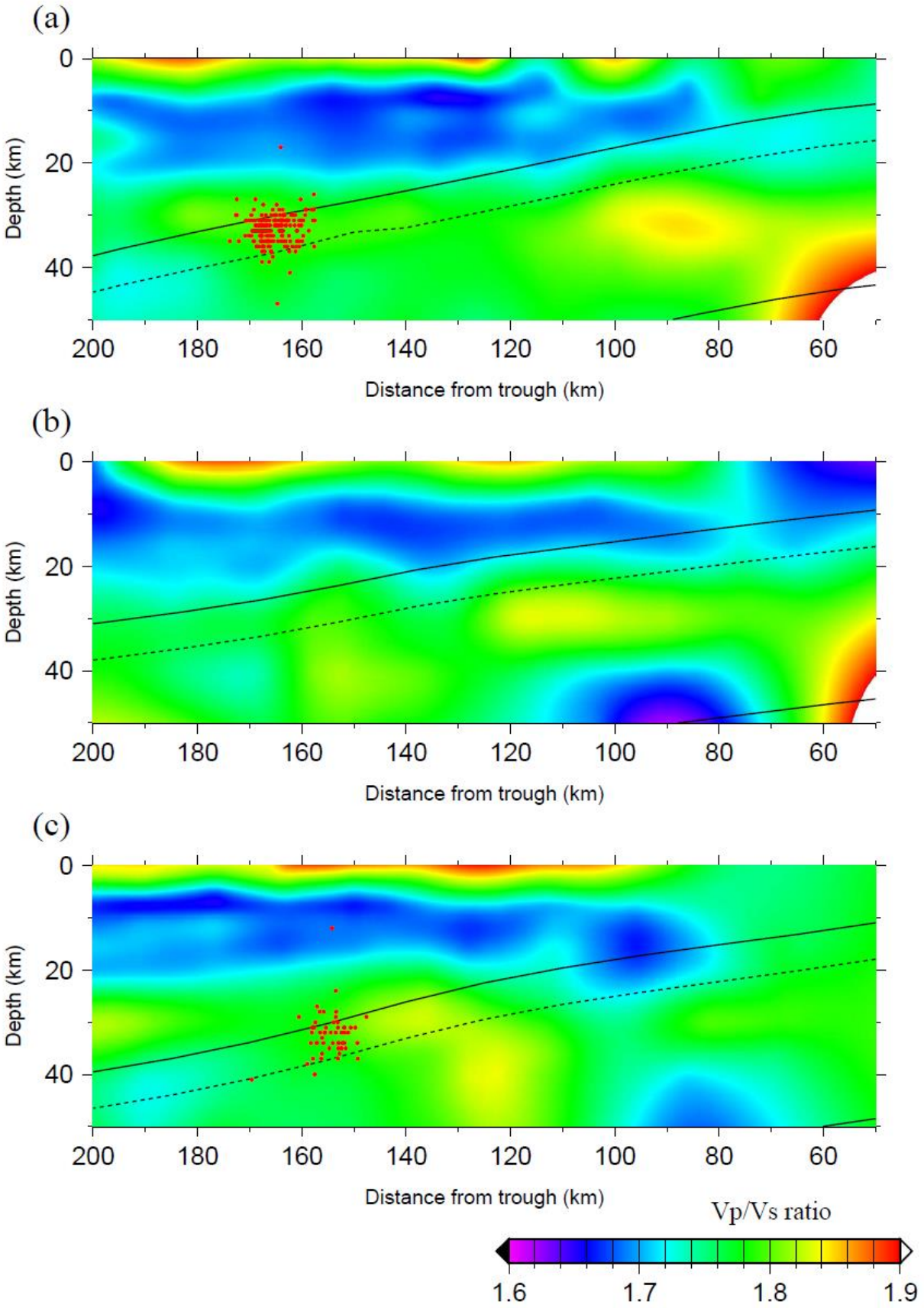
(a)
0
20
40
Depth (km)
200
180
160
140
120
100
80
60
Distance from trough (km)
(b)
0
20
40
Depth (km)
200
180
160
140
120
100
80
60
Distance from trough (km)
(c)
0
20
40
Depth (km)
200
180
160
140
120
100
80
60
Distance from trough (km)
Vp/Vs ratio
1.6
1.7
1.8
1.9

Figure 1-12

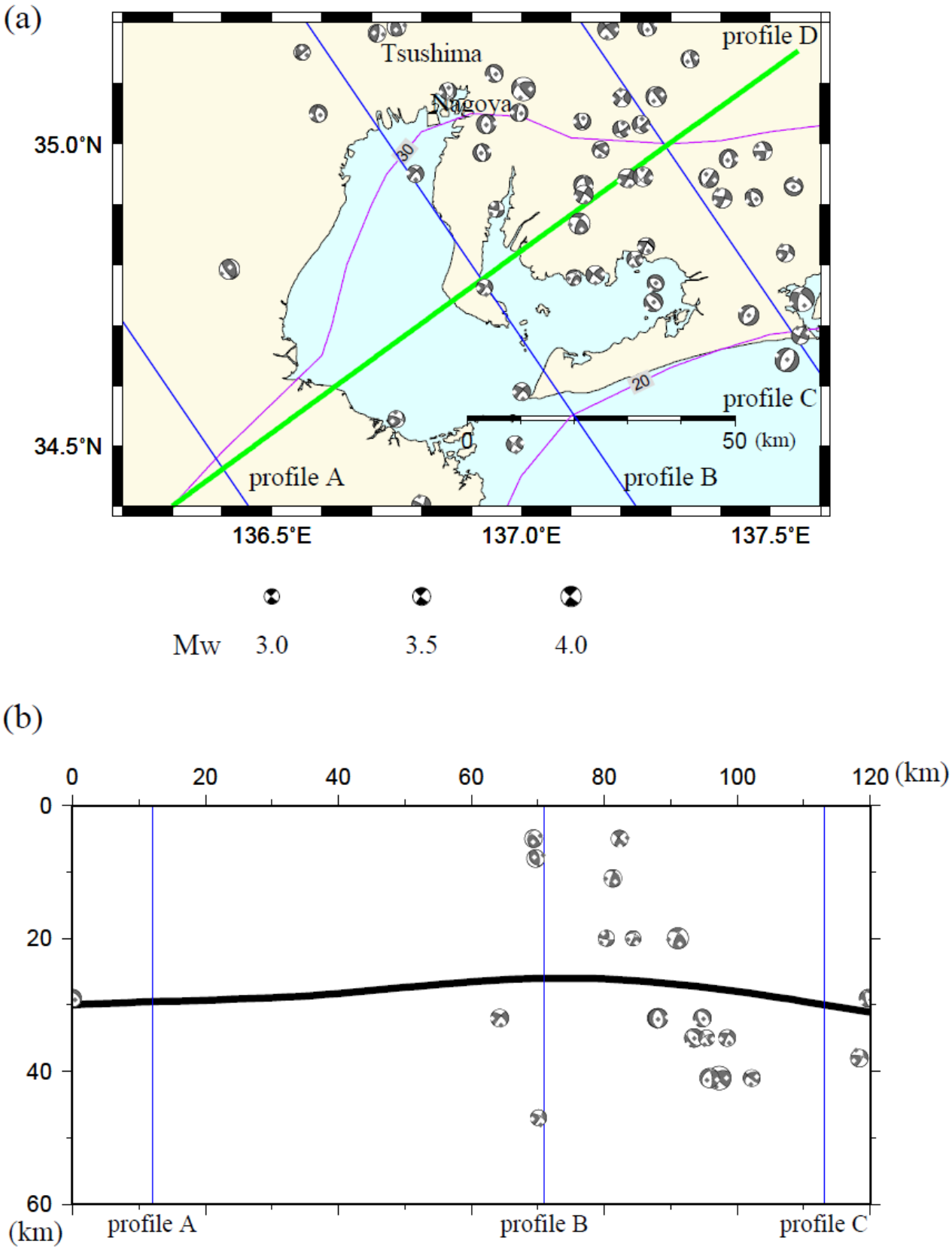
(a)
Tsushima
Nagoya
profile D
profile C
profile A
profile B
30
20
0
50 (km)
35.0°N
34.5°N
136.5°E
137.0°E
137.5°E
Mw 3.0 3.5 4.0
(b)
0 20 40 60 80 100 120 (km)
0
20
40
60
(km)
profile A
profile B
profile C

Figures (Part Ⅱ)

(Figure 2-1 ～ Figure 2-8)

Figure 2-1

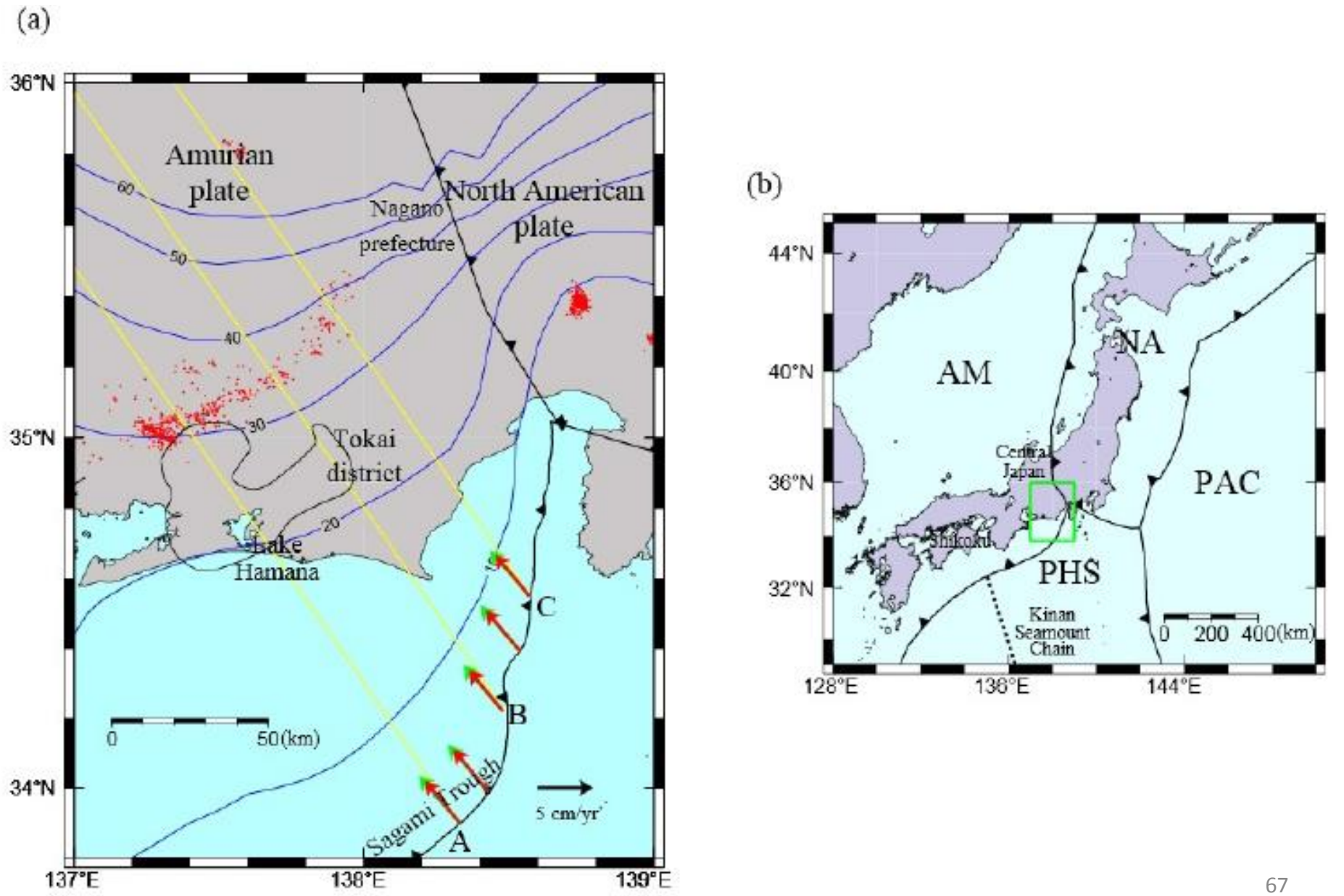
(a)
36°N
35°N
34°N
137°E
138°E
139°E
Amurian plate
North American plate
Nagano prefecture
Tokai district
Lake Hamana
60
50
40
30
20
0
50(km)
5 cm/yr
Sagami Trough
A
B
C
(b)
44°N
40°N
36°N
32°N
128°E
136°E
144°E
AM
NA
PAC
PHS
Central Japan
Shikoku
Kinan Seamount Chain
0 200 400(km)

Figure 2-2

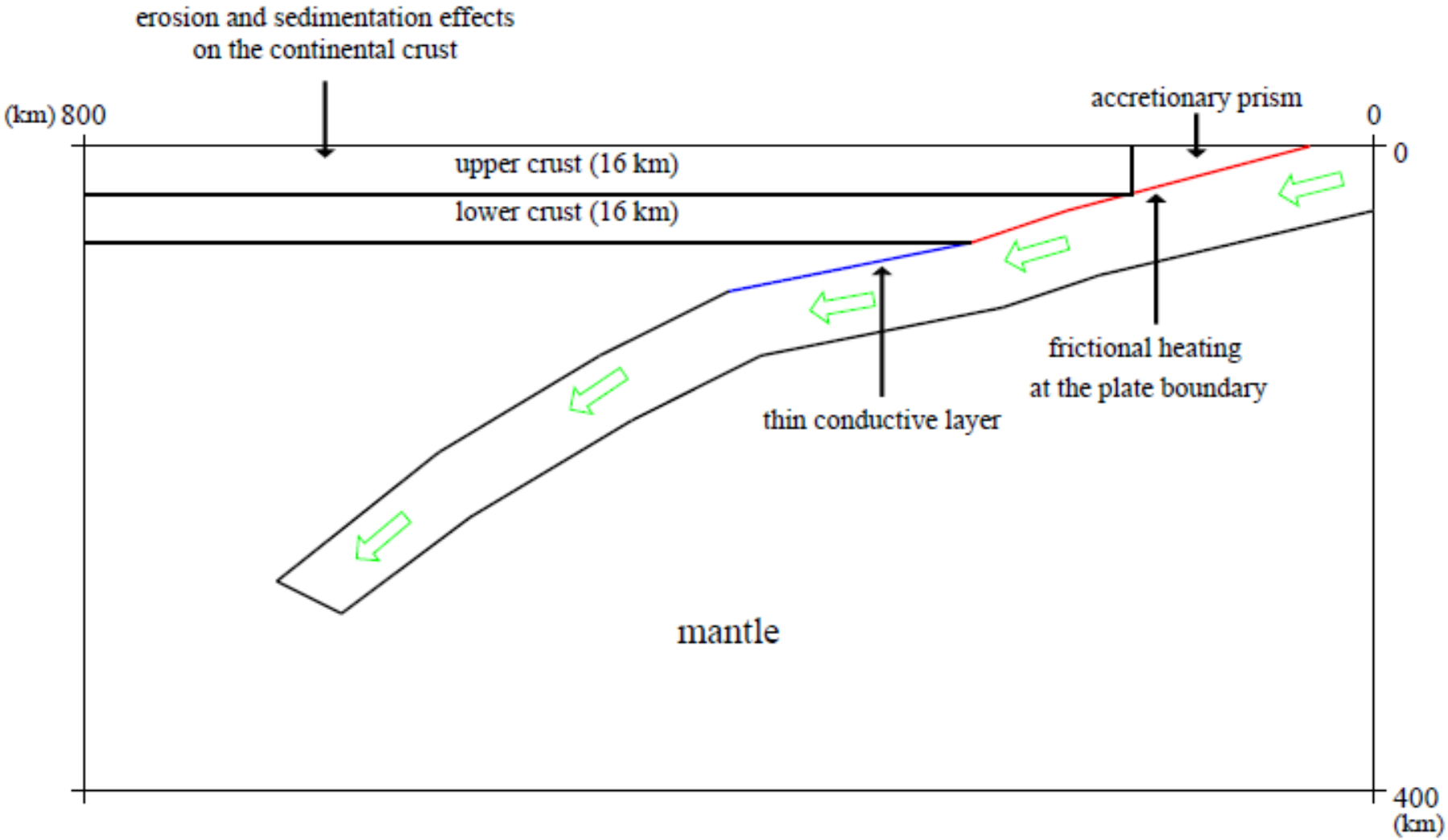
erosion and sedimentation effects
on the continental crust
(km) 800
accretionary prism
0
0
upper crust (16 km)
lower crust (16 km)
frictional heating
at the plate boundary
thin conductive layer
mantle
400
(km)

Figure 2-3

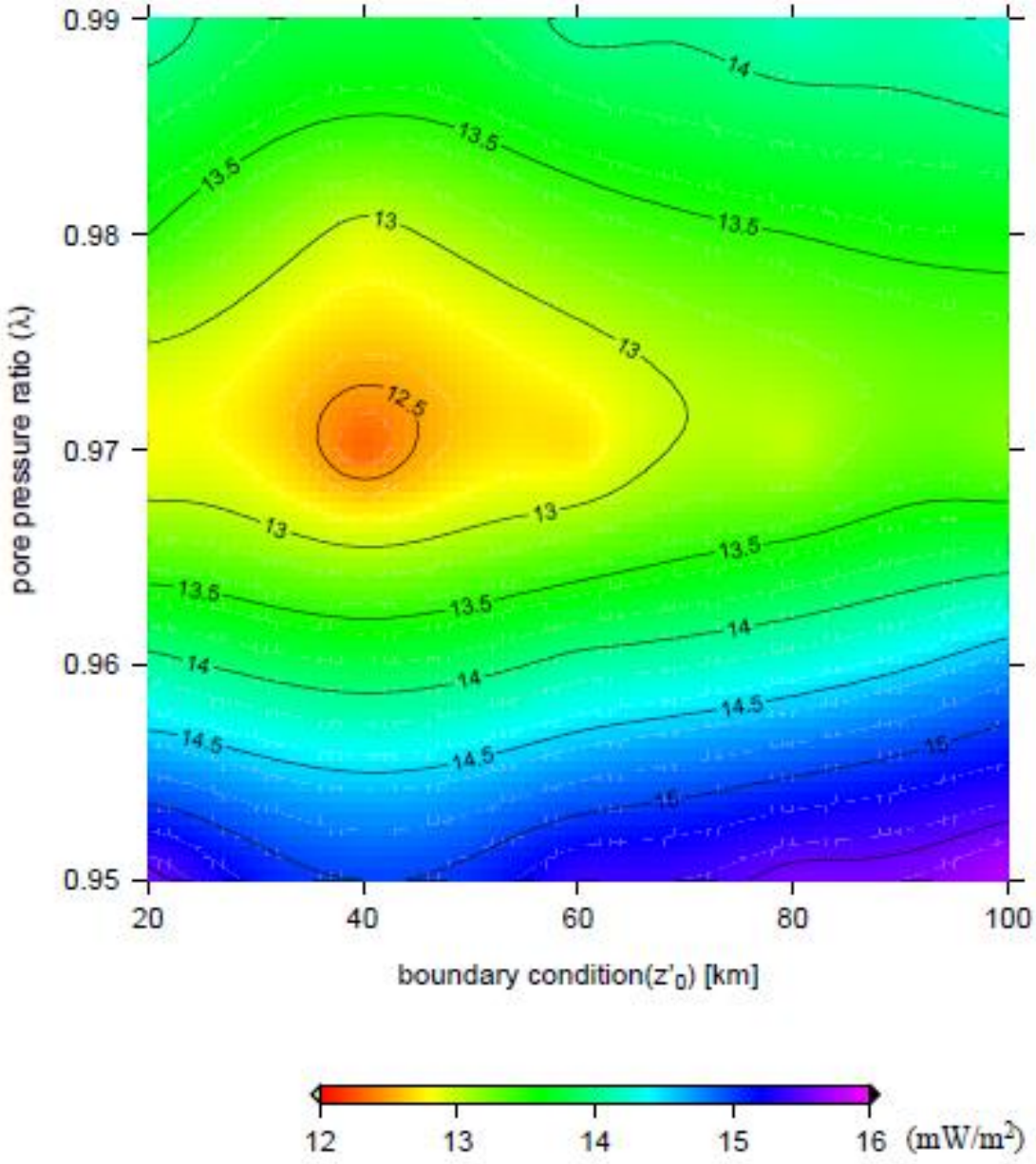
0.99
0.98
0.97
0.96
0.95
pore pressure ratio (λ)
20
40
60
80
100
boundary condition(z'0) [km]
14
13.5
13
12.5
14.5
15
12
13
14
15
16
(mW/m²)

Figure 2-4

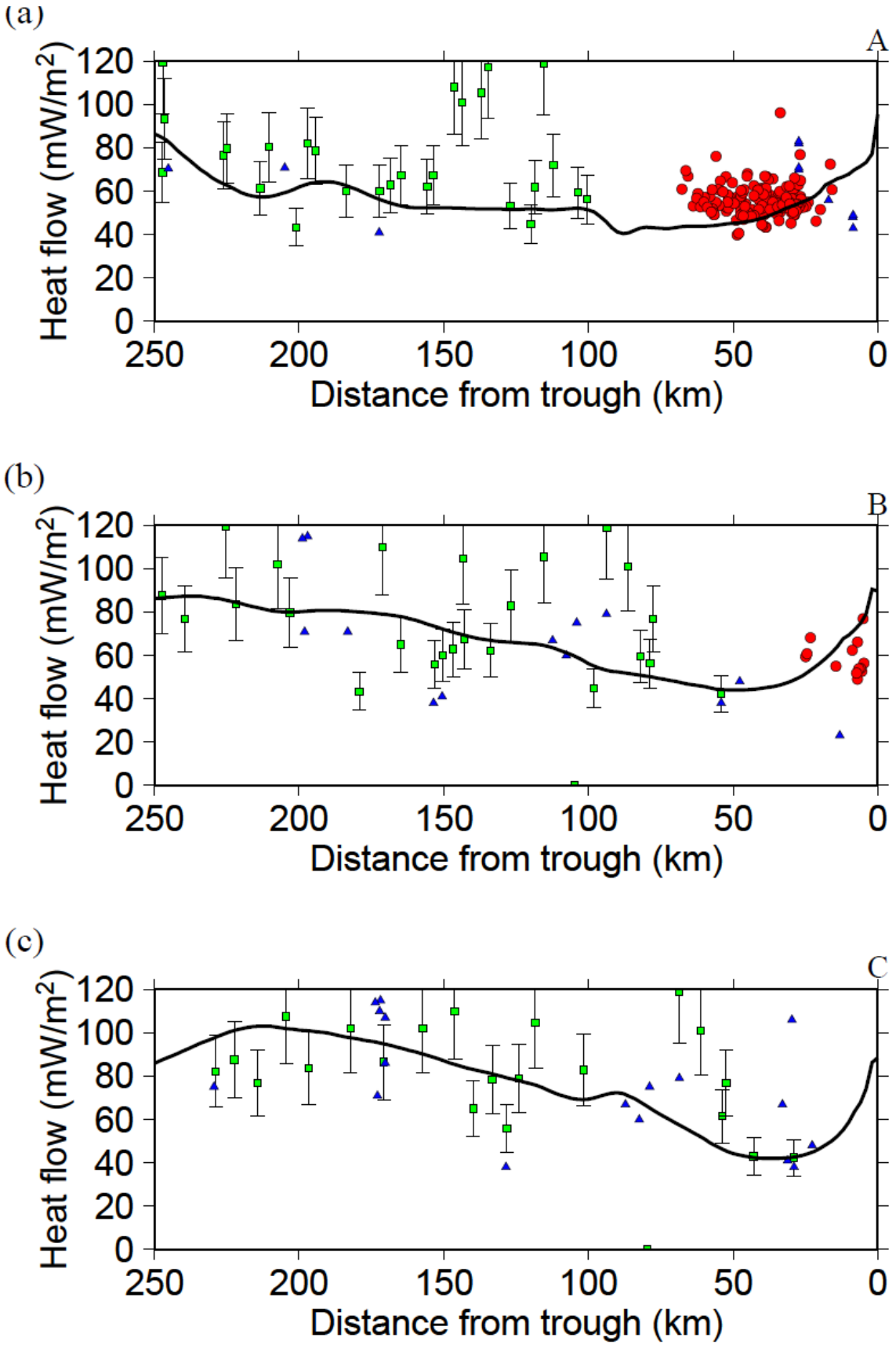
(a)
A
Heat flow (mW/m²)
120
100
80
60
40
20
0
250
200
150
100
50
0
Distance from trough (km)
(b)
B
Heat flow (mW/m²)
120
100
80
60
40
20
0
250
200
150
100
50
0
Distance from trough (km)
(c)
C
Heat flow (mW/m²)
120
100
80
60
40
20
0
250
200
150
100
50
0
Distance from trough (km)

Figure 2-5

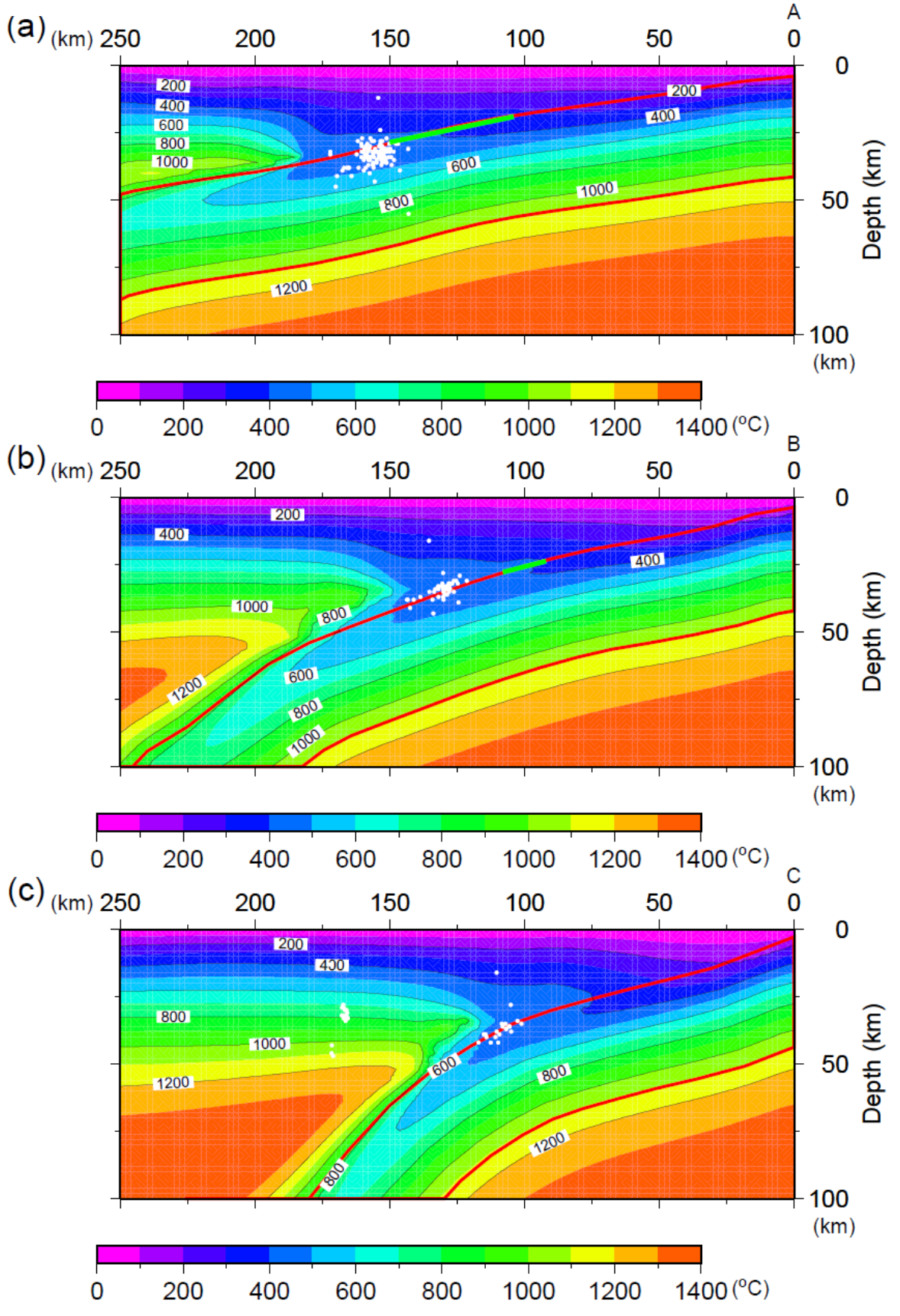
(a)
(km) 250
200
150
100
50
0
A
0
50
100
Depth (km)
(km)
200
400
600
800
1000
1200
0
200
400
600
800
1000
1200
1400 (°C)
(b)
(km) 250
200
150
100
50
0
B
0
50
100
Depth (km)
(km)
200
400
600
800
1000
1200
0
200
400
600
800
1000
1200
1400 (°C)
(c)
(km) 250
200
150
100
50
0
C
0
50
100
Depth (km)
(km)
200
400
600
800
1000
1200
0
200
400
600
800
1000
1200
1400 (°C)

Figure 2-6

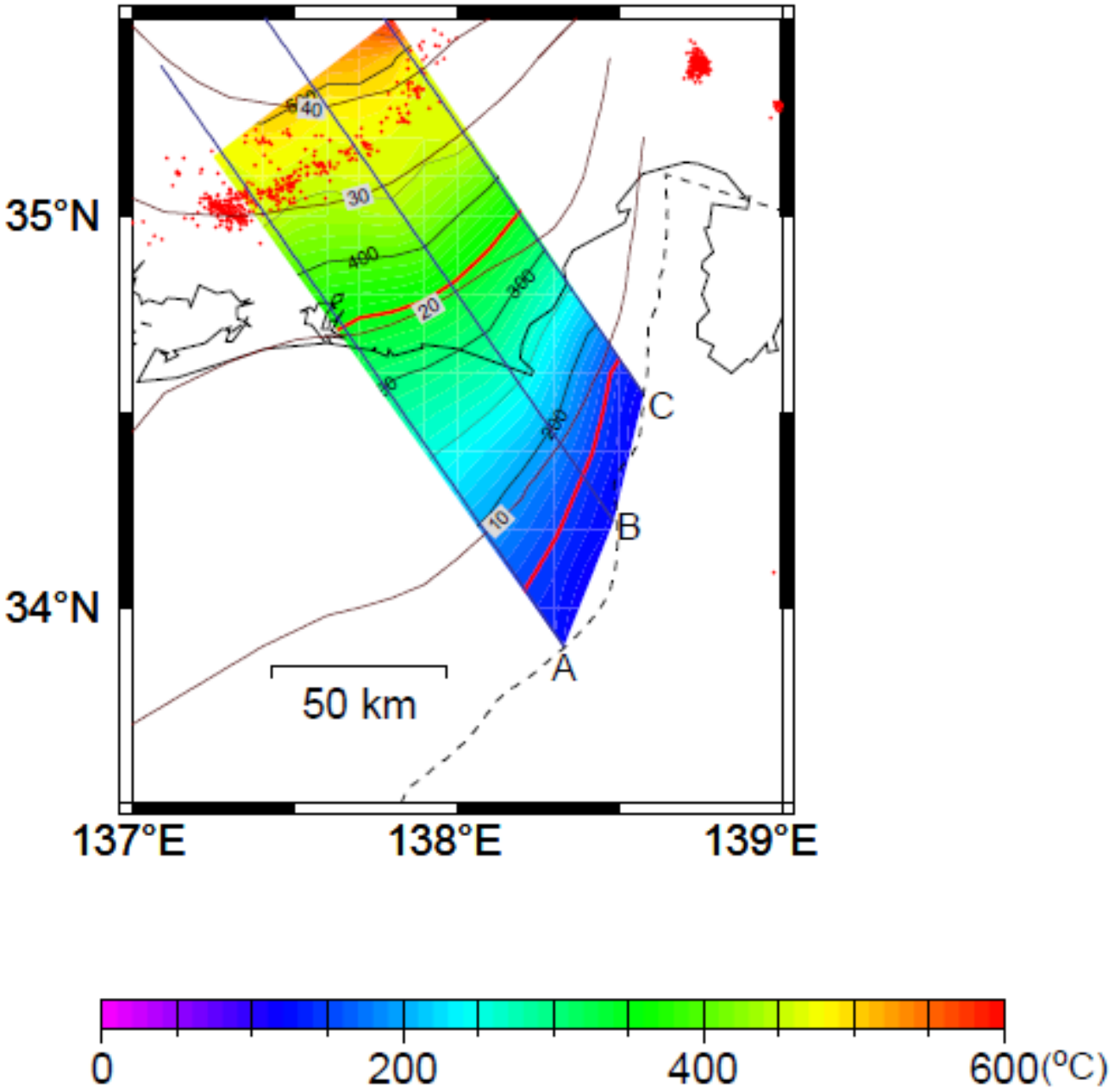
35°N
34°N
137°E
138°E
139°E
40
30
400
20
300
10
200
A
B
C
50 km
0
200
400
600(°C)

Figure 2-7

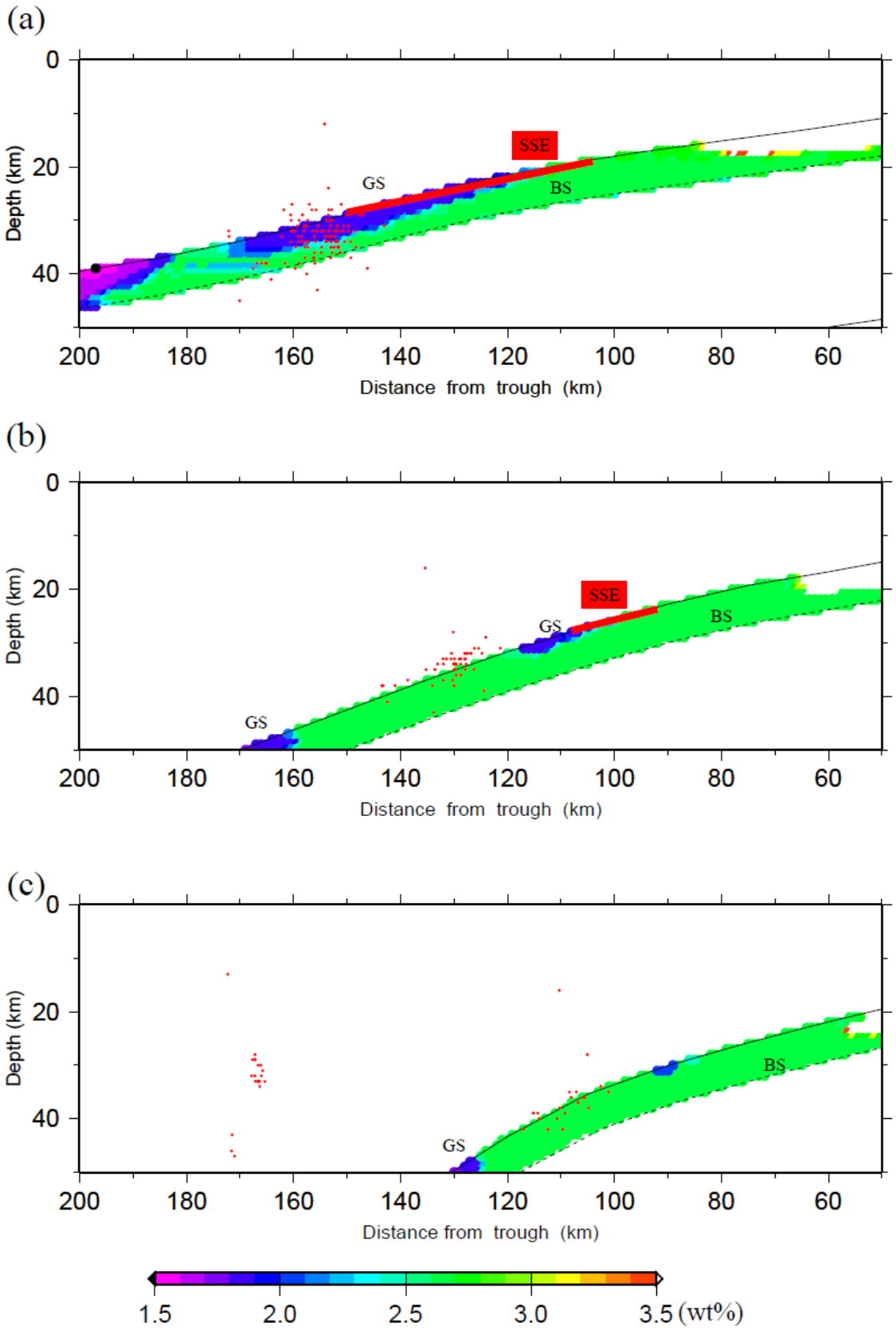
(a)
Depth (km)
0
20
40
SSE
GS
BS
200
180
160
140
120
100
80
60
Distance from trough (km)
(b)
Depth (km)
0
20
40
SSE
GS
BS
GS
200
180
160
140
120
100
80
60
Distance from trough (km)
(c)
Depth (km)
0
20
40
BS
GS
200
180
160
140
120
100
80
60
Distance from trough (km)
1.5
2.0
2.5
3.0
3.5 (wt%)

Figure 2-8

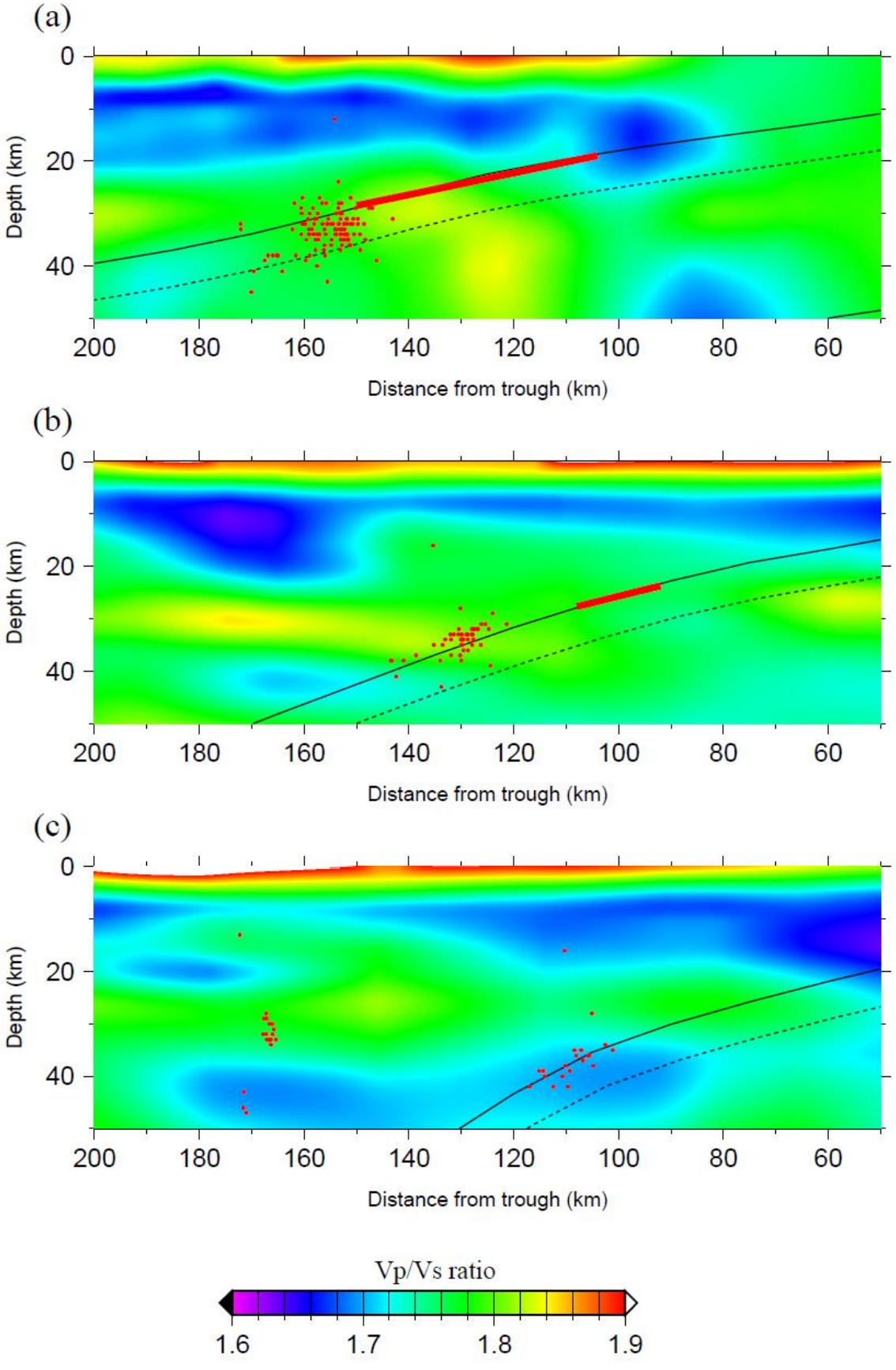
(a)
0
20
40
Depth (km)
200
180
160
140
120
100
80
60
Distance from trough (km)
(b)
0
20
40
Depth (km)
200
180
160
140
120
100
80
60
Distance from trough (km)
(c)
0
20
40
Depth (km)
200
180
160
140
120
100
80
60
Distance from trough (km)
Vp/Vs ratio
1.6
1.7
1.8
1.9

Figures (Part Ⅲ)

(Figure 3-1 ～ Figure 3-12)

Figure 3-1

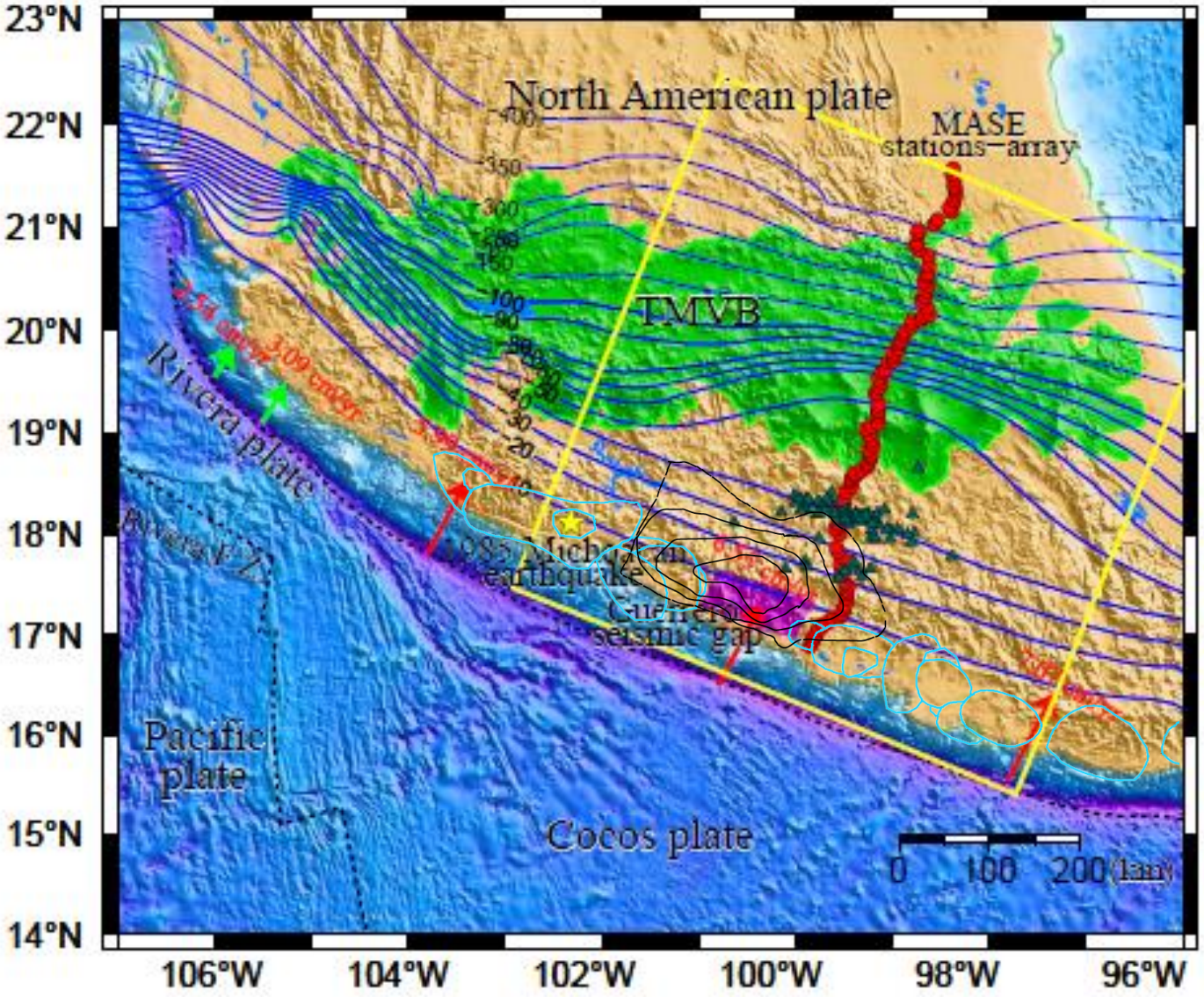
North American plate
MASE
stations—array
TMVB
Rivera plate
Pacific
plate
Cocos plate
seismic gap
0
100
200
23°N
22°N
21°N
20°N
19°N
18°N
17°N
16°N
15°N
14°N
106°W
104°W
102°W
100°W
98°W
96°W

Figure 3-2

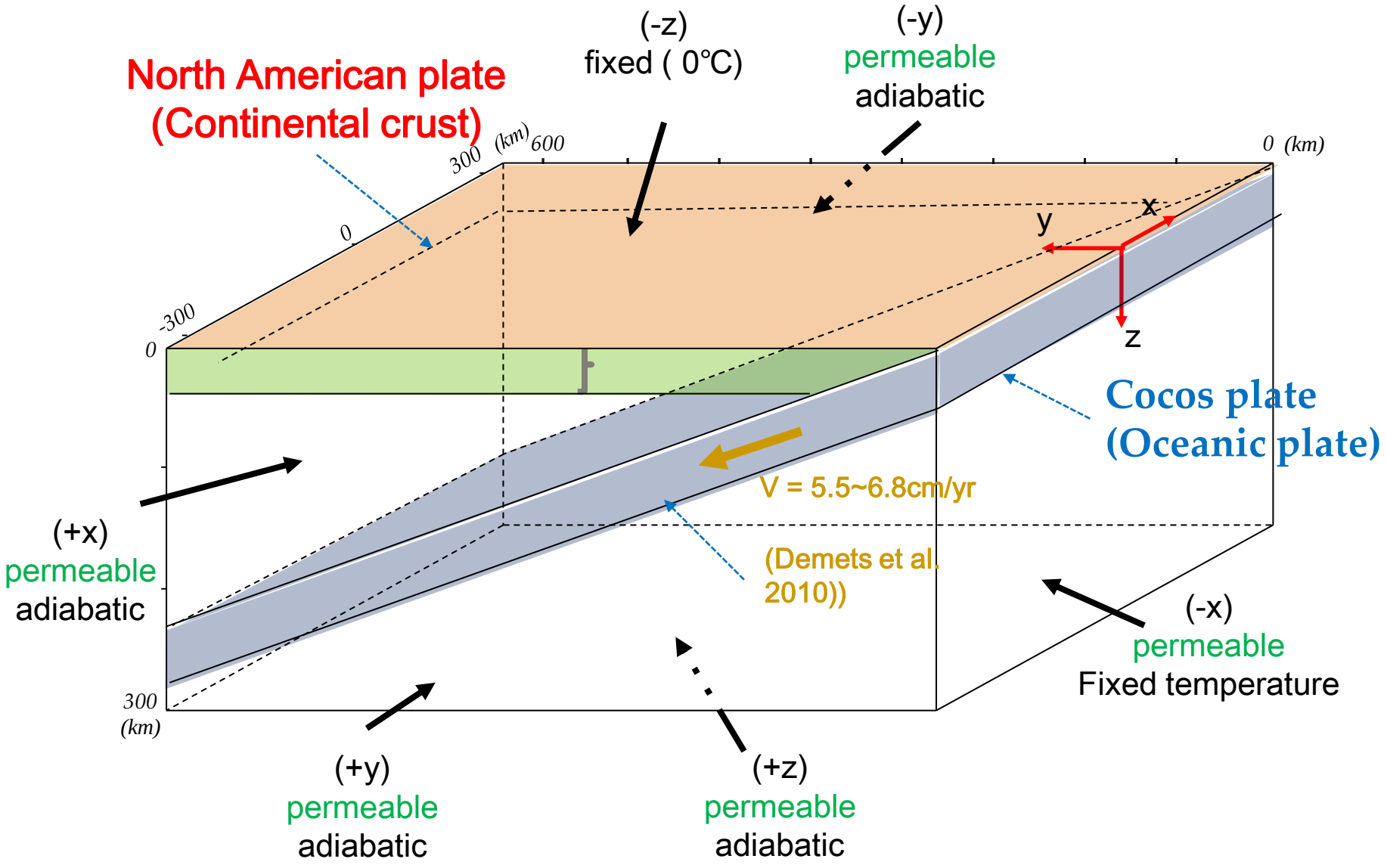
North American plate
(Continental crust)
(-z)
fixed (0°C)
(-y)
permeable
adiabatic
300
(km)
600
0
(km)
0
-300
0
x
y
z
Cocos plate
(Oceanic plate)
V = 5.5~6.8cm/yr
(Demets et al.
2010))
(+x)
permeable
adiabatic
300
(km)
(-x)
permeable
Fixed temperature
(+y)
permeable
adiabatic
(+z)
permeable
adiabatic

Figure 3-3

(a)

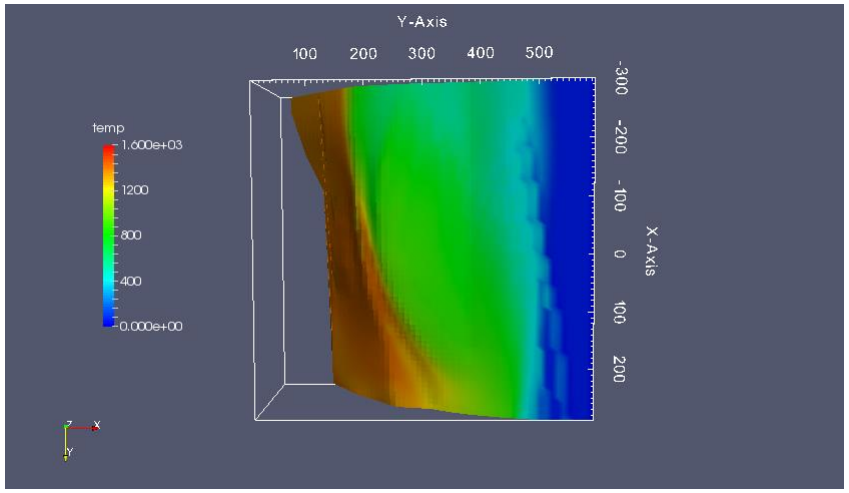

(b)

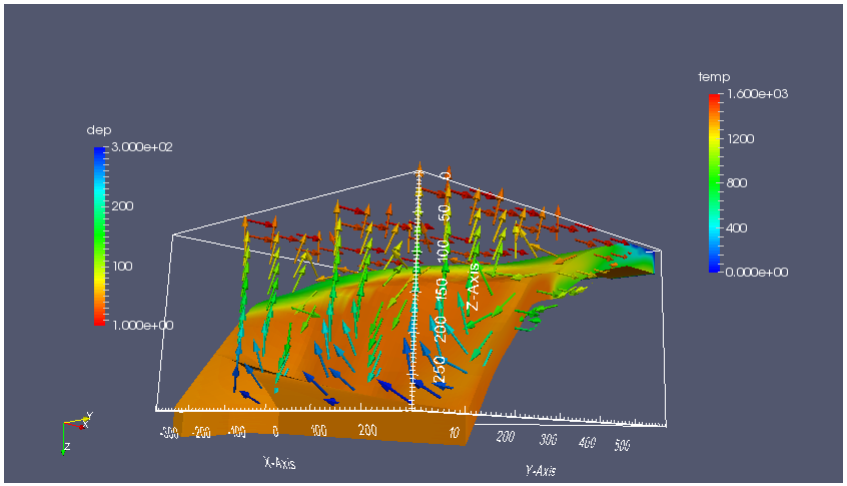

(c)

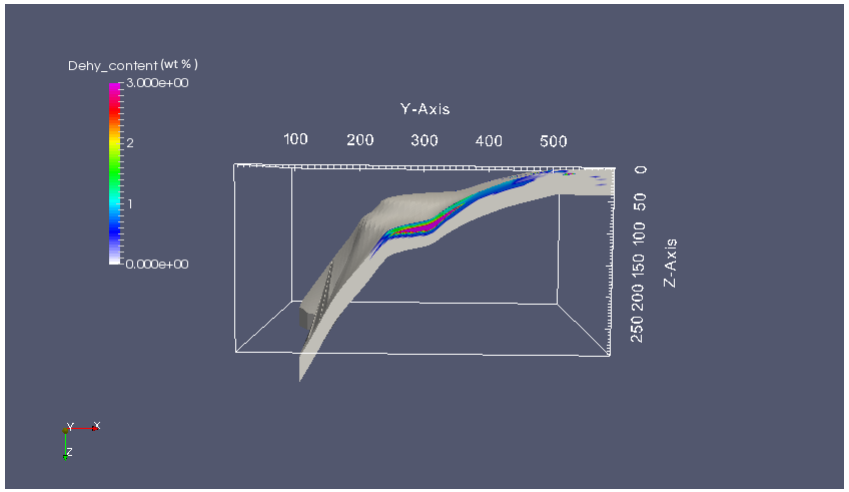

(d)

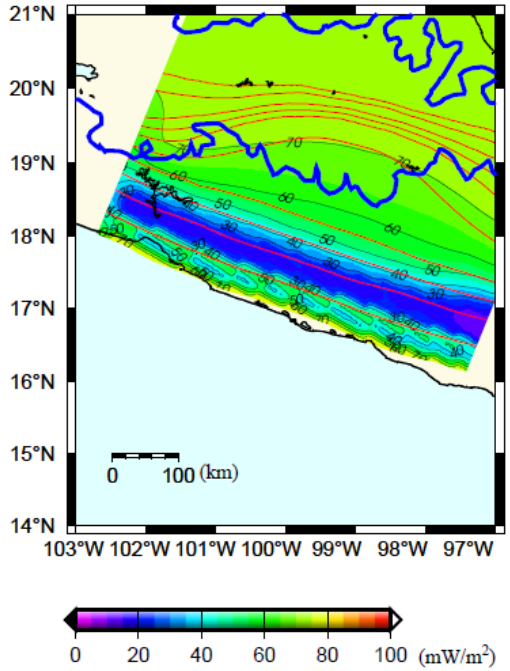

Figure 3-4

(a)

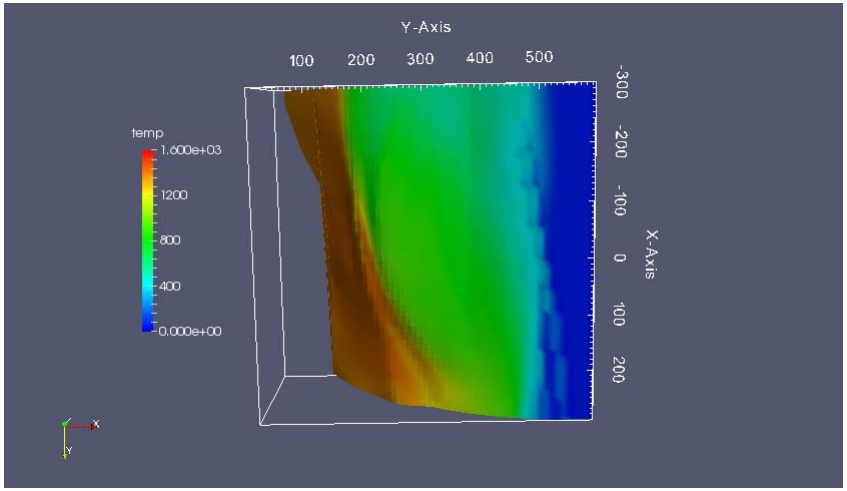

(b)

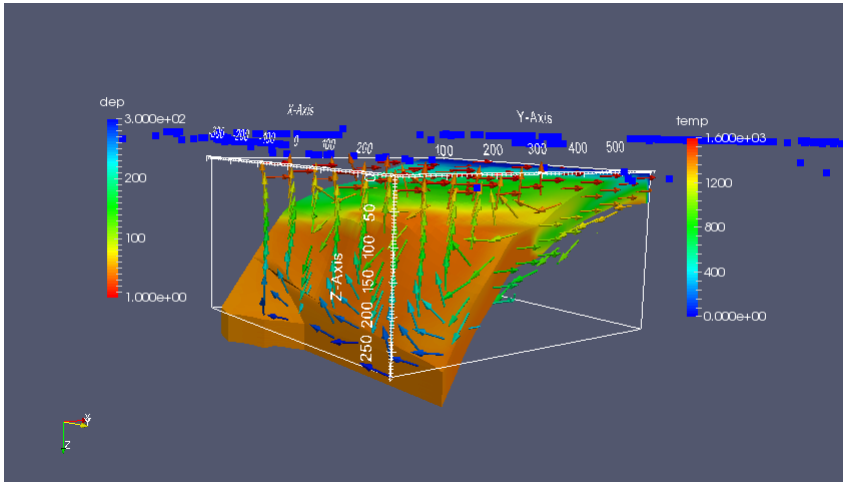

(c)

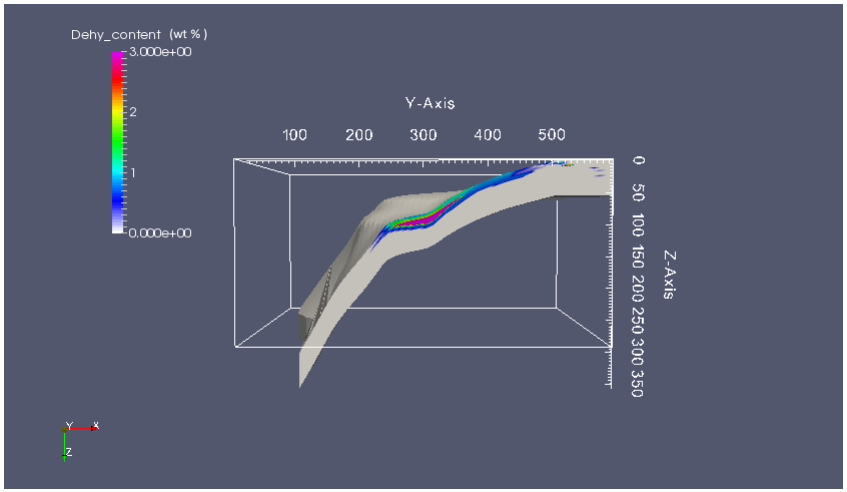

(d)

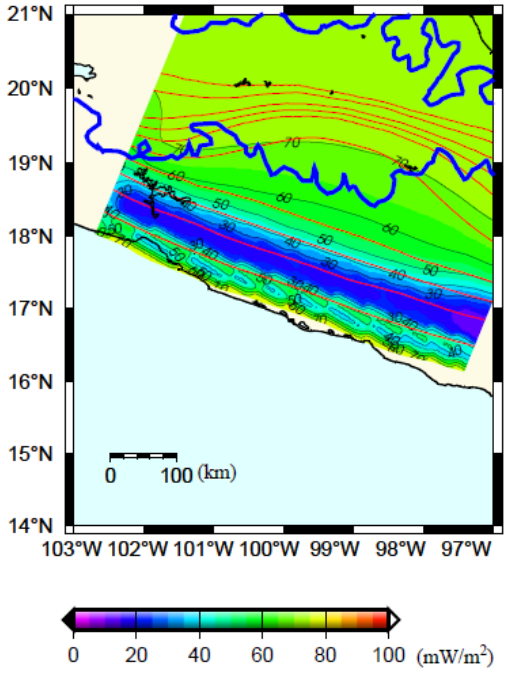

Figure 3-5

(a)

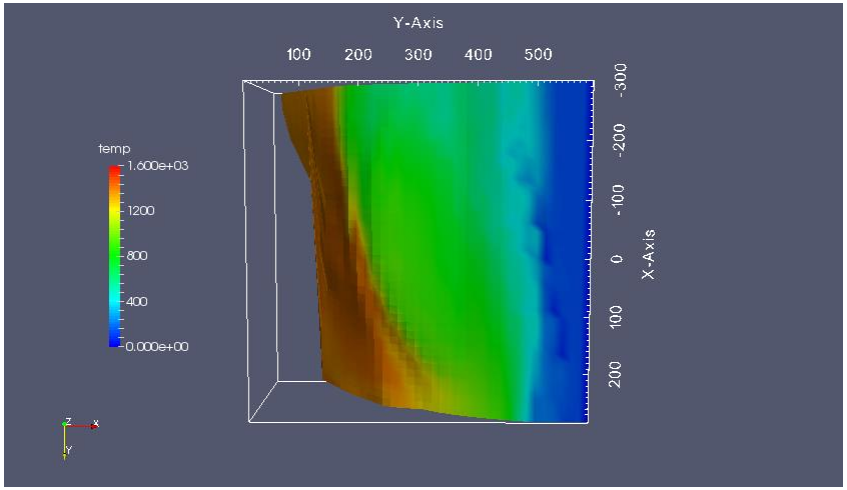

(b)

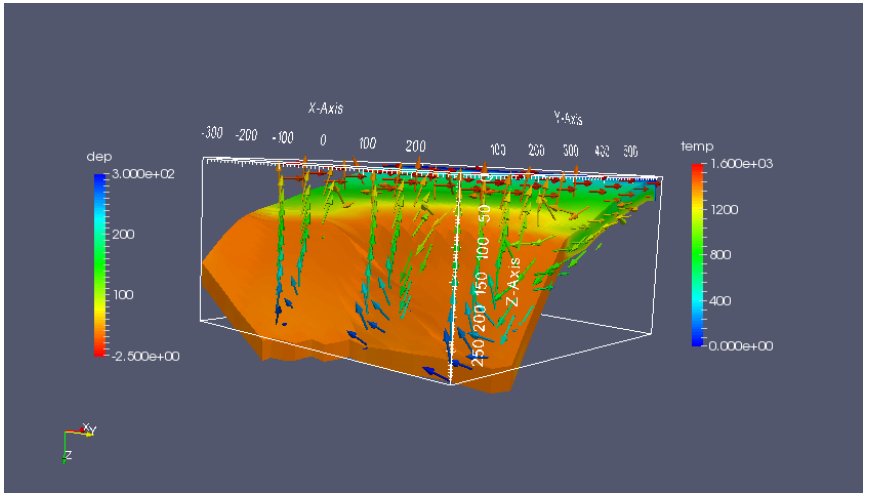

(c)

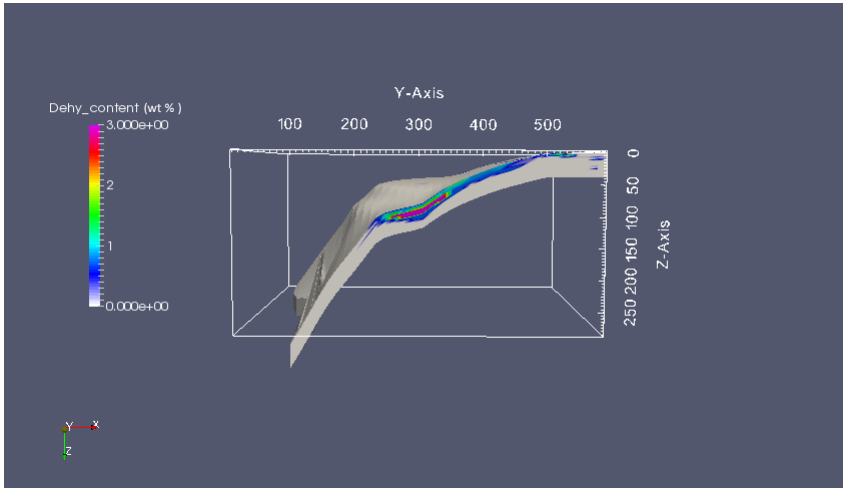

(d)

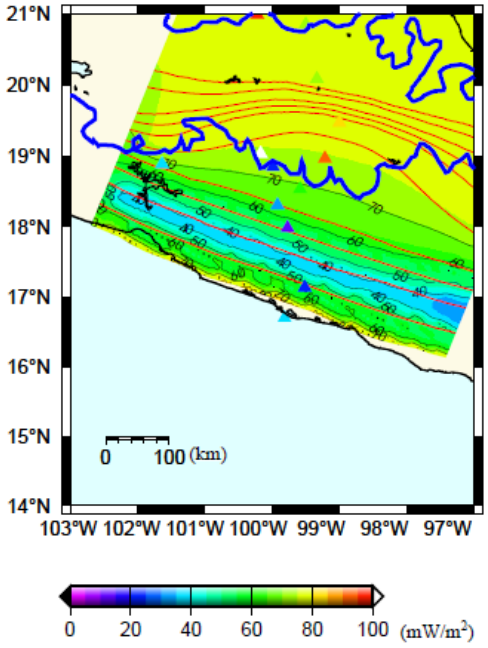

Figure 3-6

(a)

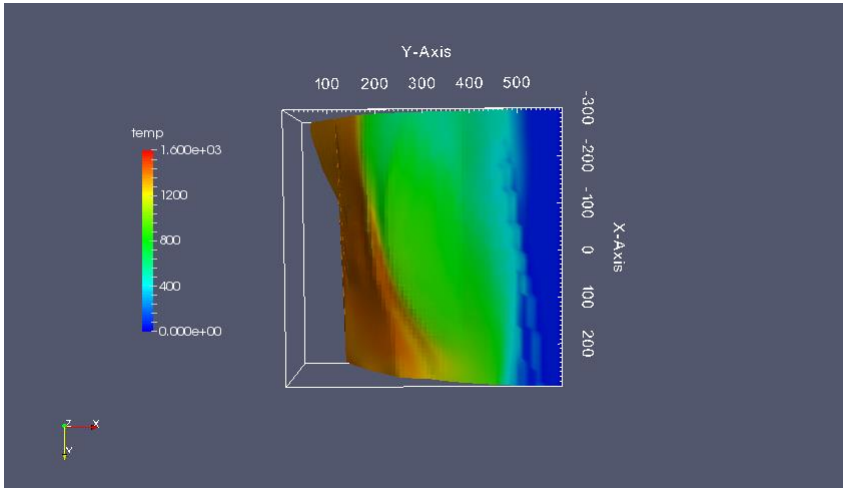

(b)

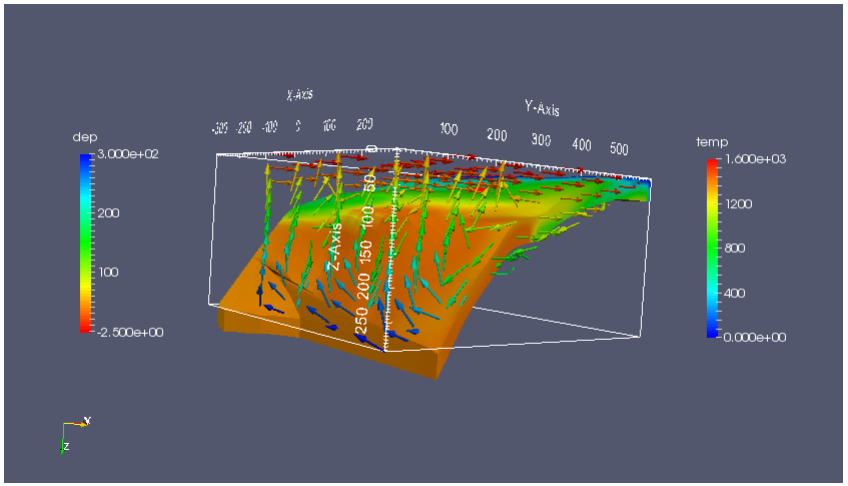

(c)

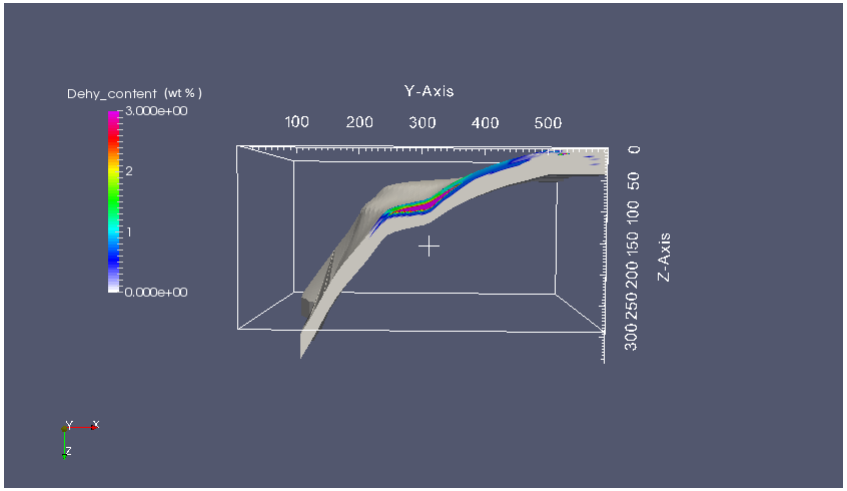

(d)

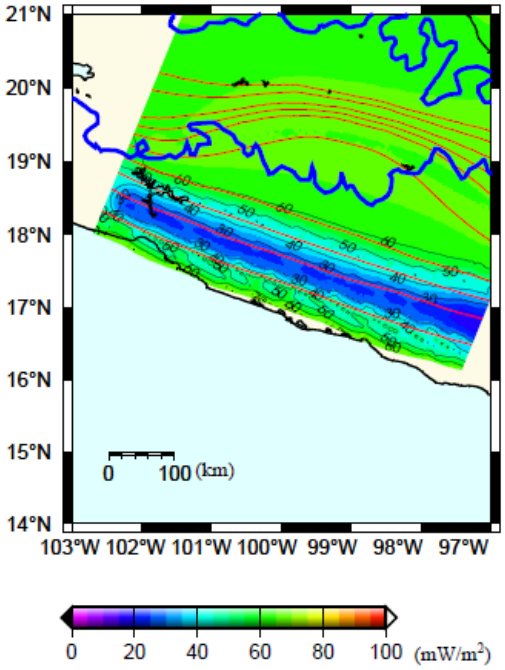

Figure 3-7

(a)

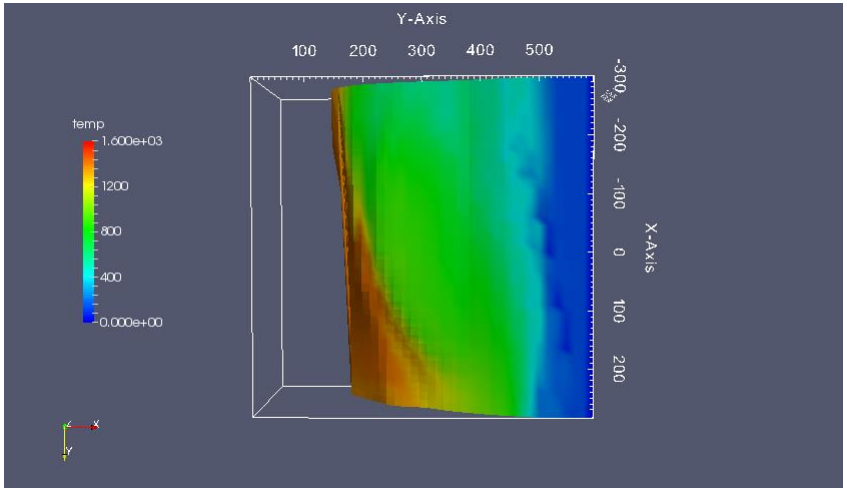

(b)

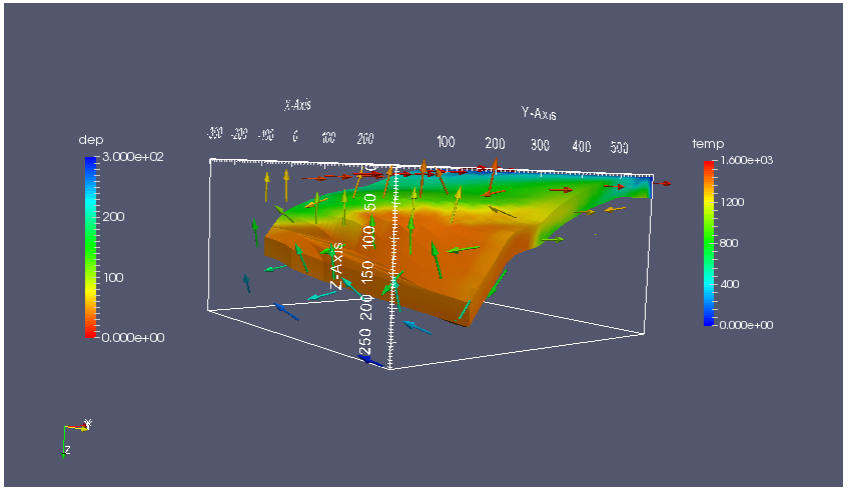

(c)

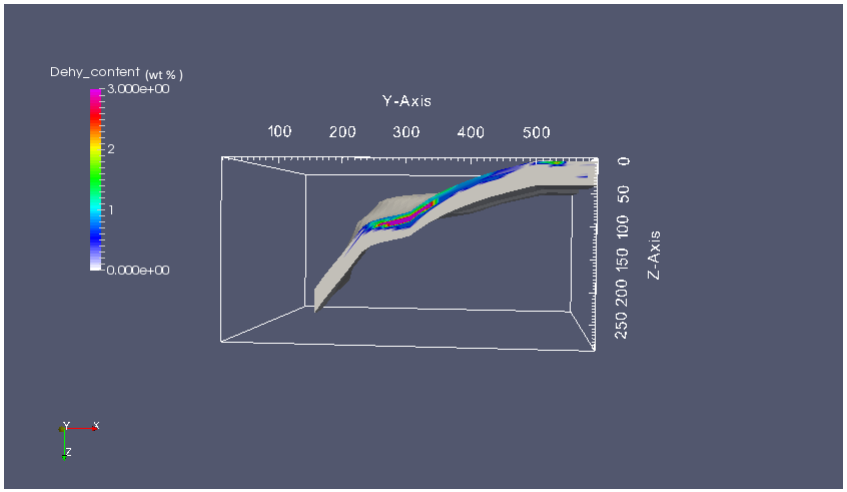

(d)

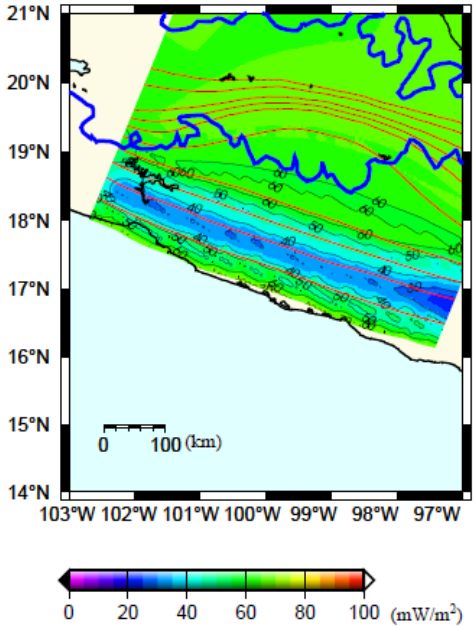

Figure 3-8

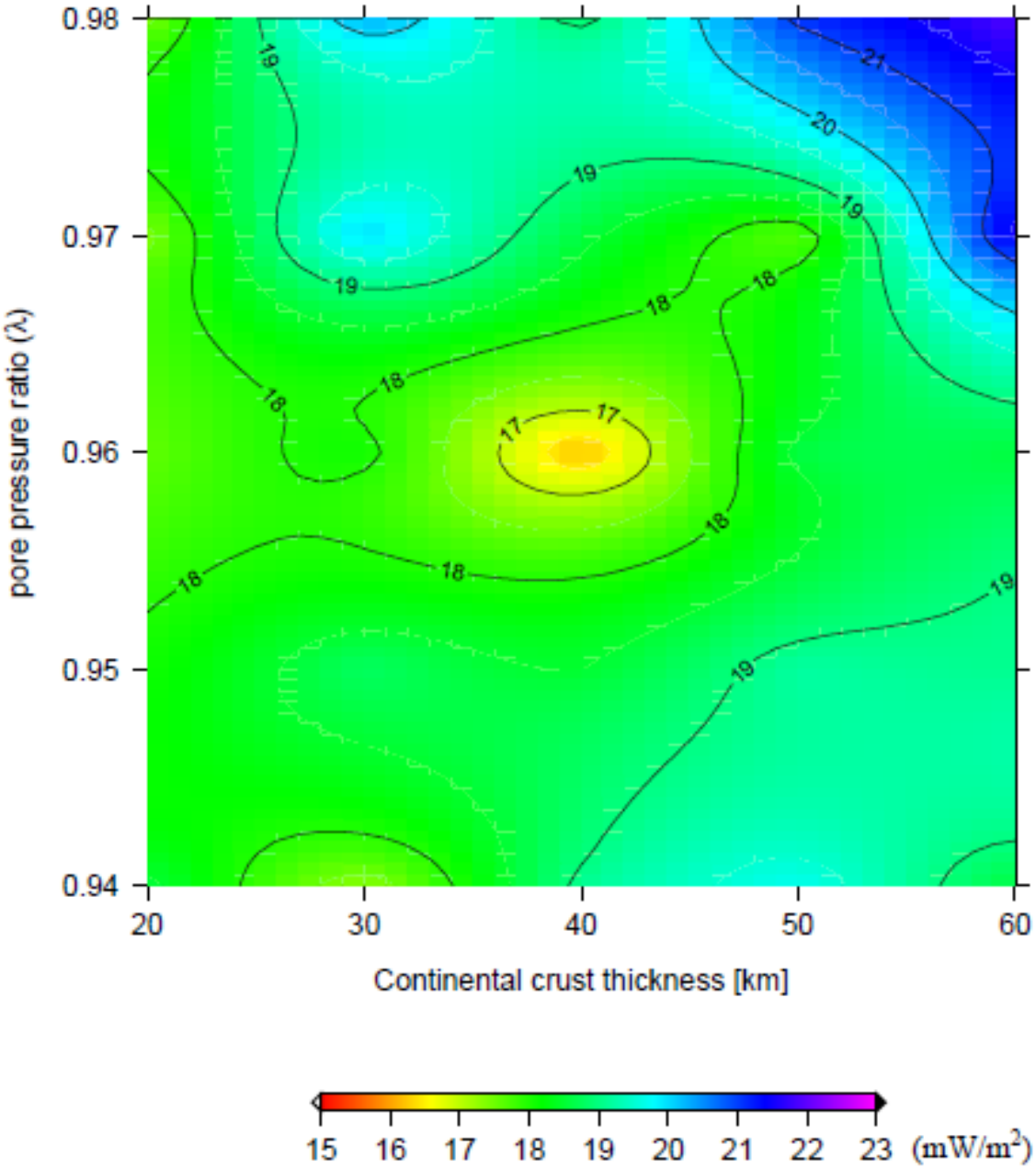
0.98
0.97
0.96
0.95
0.94
pore pressure ratio (λ)
20
30
40
50
60
Continental crust thickness [km]
19
21
20
19
19
19
18
18
18
18
17
17
18
18
18
19
19
15
16
17
18
19
20
21
22
23
(mW/m²)

Figure 3-9

(a)

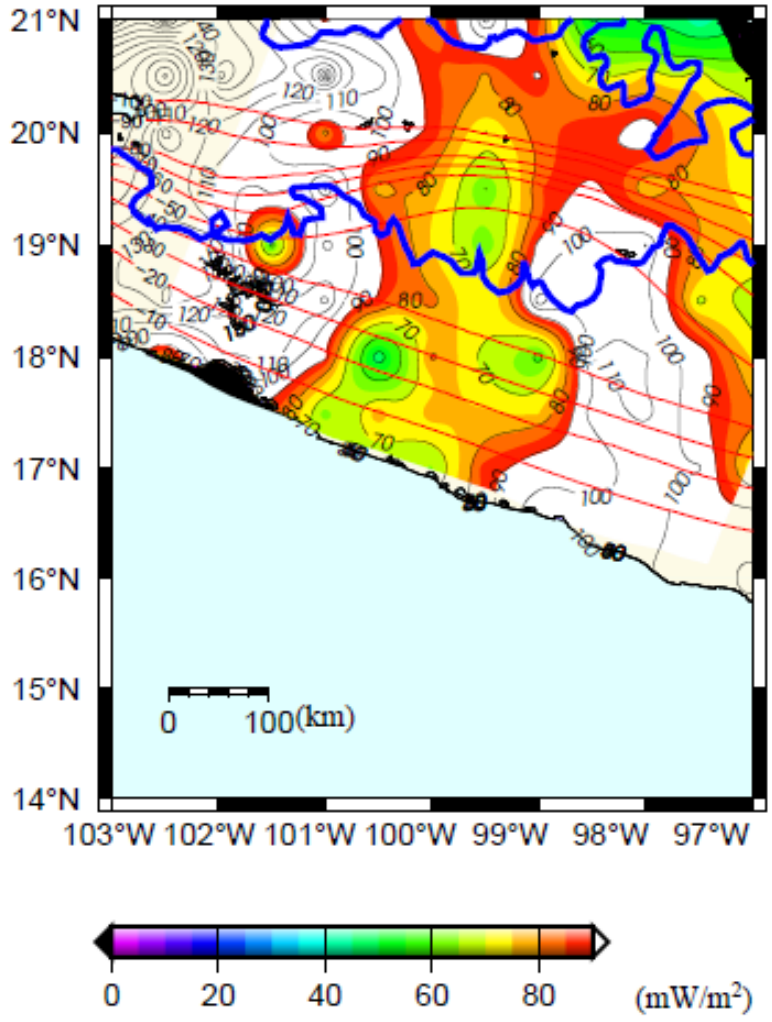
21°N
20°N
19°N
18°N
17°N
16°N
15°N
14°N
103°W 102°W 101°W 100°W 99°W 98°W 97°W
0 100(km)
0 20 40 60 80 (mW/m²)

(b)

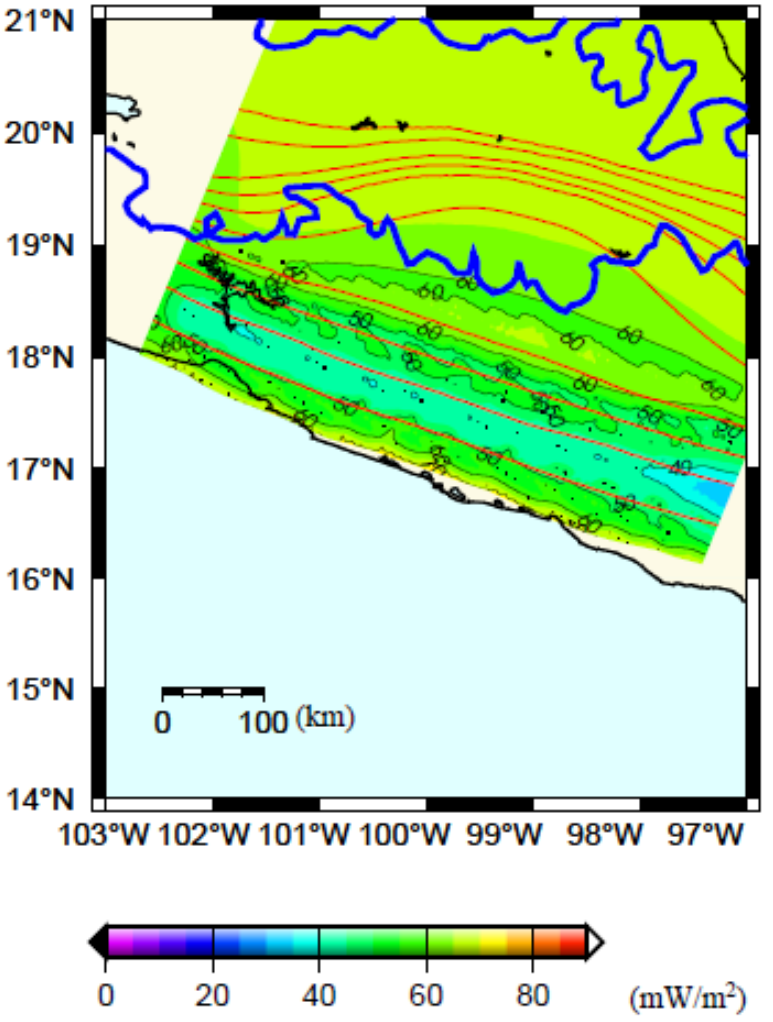
21°N
20°N
19°N
18°N
17°N
16°N
15°N
14°N
103°W 102°W 101°W 100°W 99°W 98°W 97°W
0 100 (km)
0 20 40 60 80 (mW/m²)

Figure 3-10

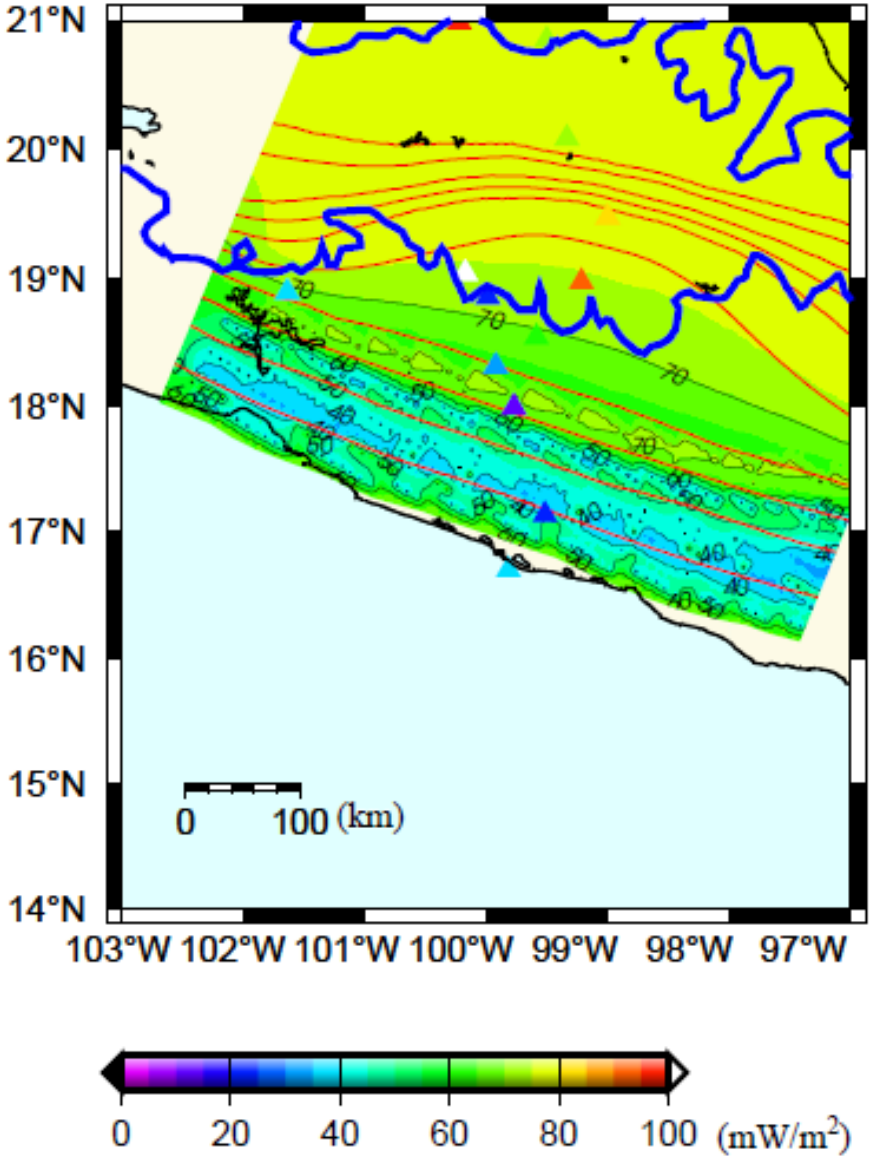
21°N
20°N
19°N
18°N
17°N
16°N
15°N
14°N
103°W 102°W 101°W 100°W 99°W 98°W 97°W
0 100 (km)
0 20 40 60 80 100 (mW/m²)

Figure 3-11

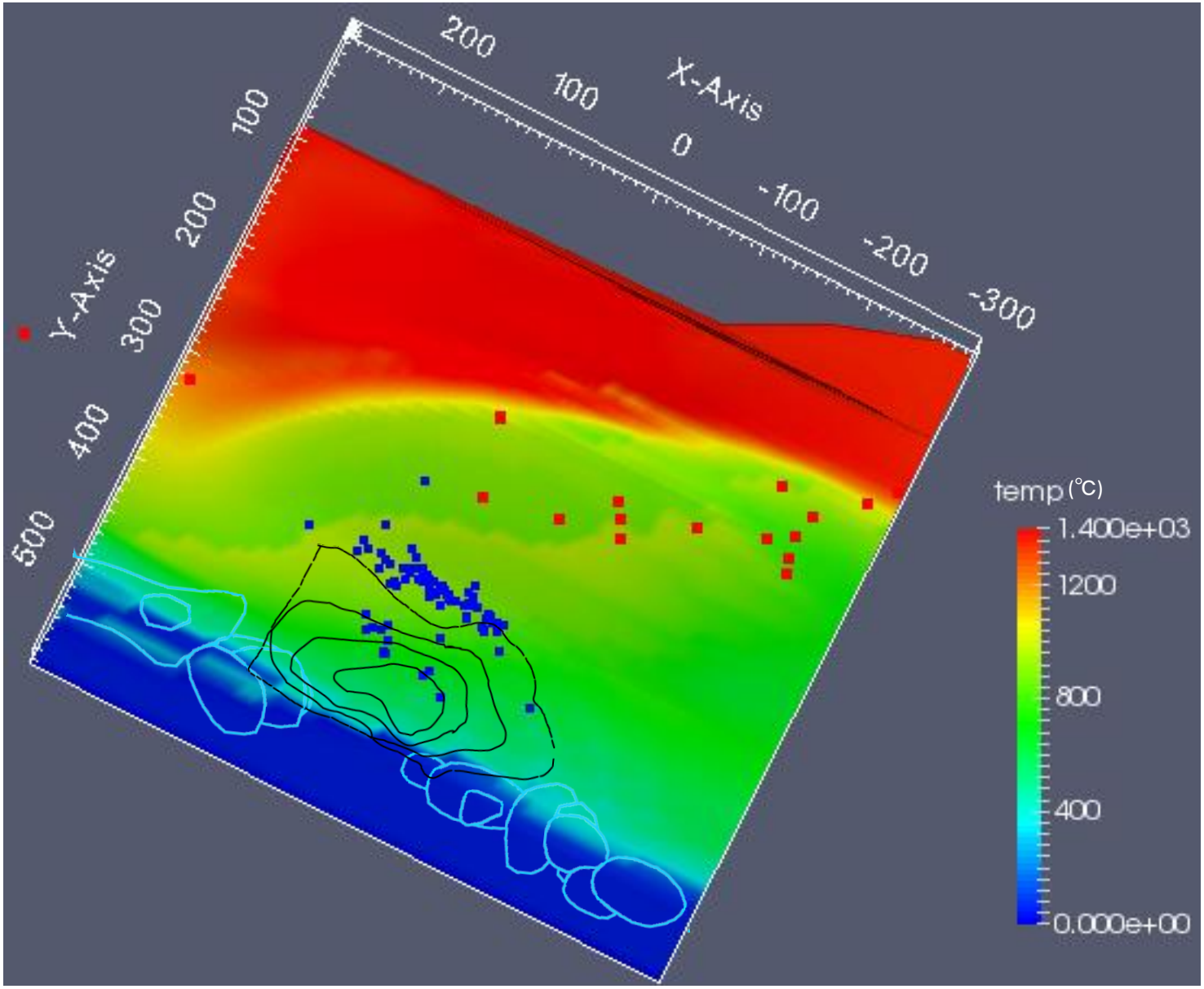
200
100
X-Axis
0
-100
-200
-300
100
200
Y-Axis
300
400
500
temp (°C)
1.400e+03
1200
800
400
0.000e+00

Figure 3-12

(a)

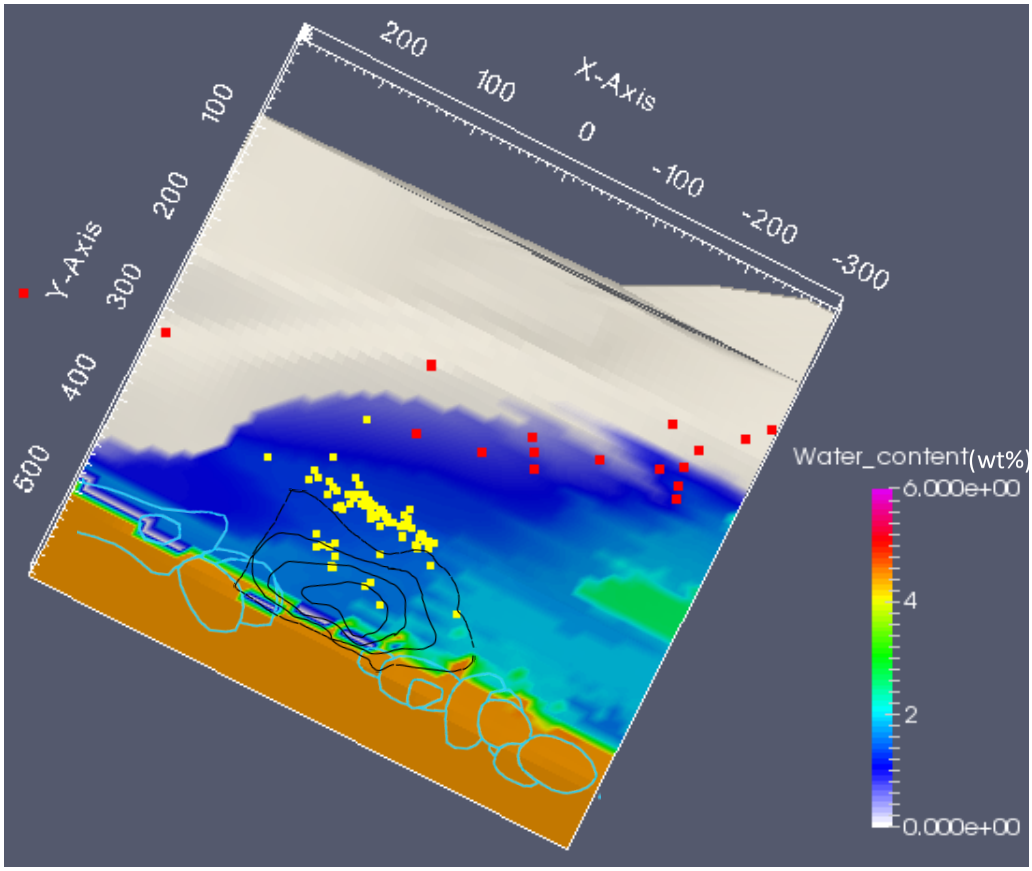

(b)

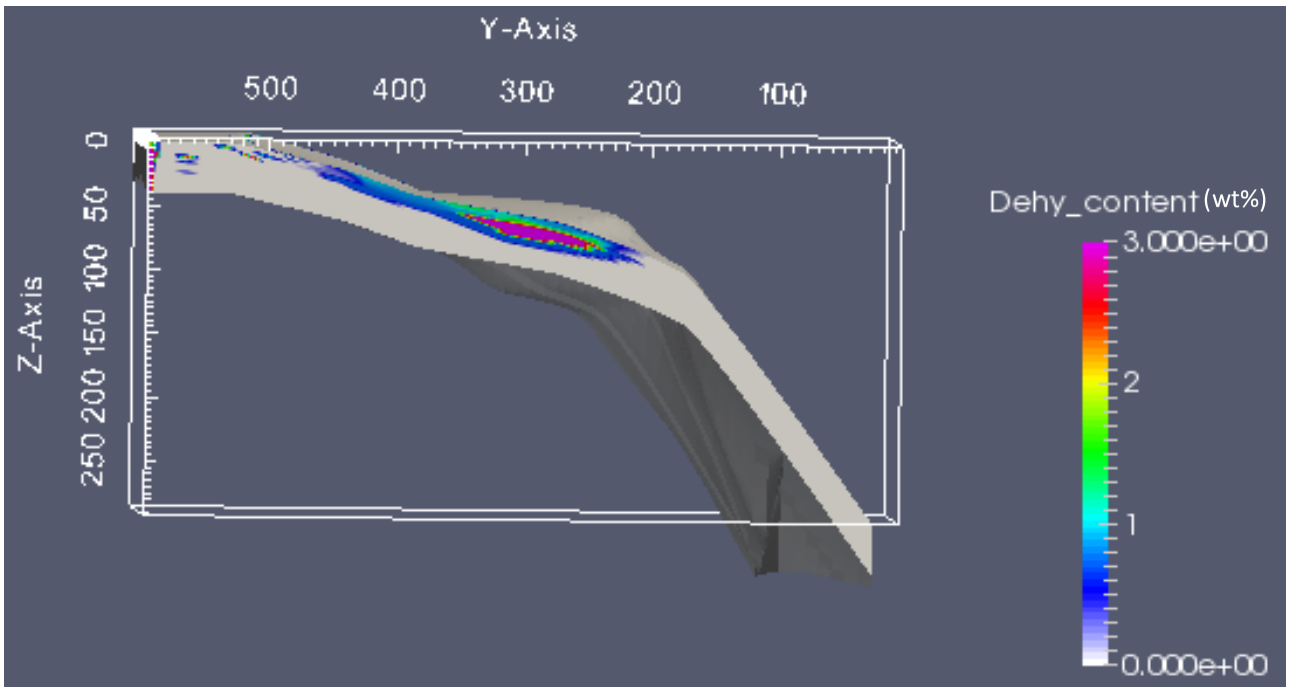

Figure Captions

Part Ⅰ

Fig. 1-1 Tectonic map of central Japan. Barbed grey lines denote plate boundaries at the Earth's surface. The purple solid lines represent isodepth contours of the upper surface of the subducting PHS plate (Nakajima and Hasegawa, 2007; Hirose et al., 2008). Red dots denote the distribution of the epicentres of LFEs during the period from October 1, 1997 to February 28, 2015. Blue lines denote profiles for the numerical simulations. The area enclosed by the red line in the lower right figure is the study area. In the inset, NA, AM, PAC, and PHS indicate the North American plate, the Amurian plate, the Pacific plate, and the Philippine Sea plate, respectively.

Fig. 1-2 (a) Distributions of the heat flow observation stations. Red circles, blue triangles, and green squares denote observation stations of BSR, the land borehole and marine heat probe, and Hi-net observation wells, respectively. (b) The spatial distribution of the observed heat flow obtained by spatial smoothing of the data, using a Bayesian information criterion (ABIC) (Akaike, 1980). Yellow lines denote profiles for the numerical simulations.

Fig. 1-3 (a) Spatial distribution of the uplift rate for the Quaternary period (the last two million years) calculated from the amount of uplift and subsidence for the period (The Research Group for the Quaternary Tectonic Map, 1968). Red lines denote profiles for the numerical simulations. (b) The uplift rate along profile A. (c) The uplift rate along profile B. (d) The uplift rate along profile C.

Fig. 1-4 Schematic figure of the 2-D box-type thermal convection model used in this study. Green letters denote boundary conditions for temperature fields, and blue letters denote the boundary conditions for flow fields.

Fig. 1-5 (a) Temporal change of the subducting velocity of the PHS plate along each profile for the last 15 Myr. Green, red, and blue lines represent subduction velocities at the trough for profiles A, B, and C, respectively. (b) Temporal change of the slab thickness of the PHS plate along each profile for the last 15 Myr. Green, red, and blue lines denote slab thickness at the trough for profiles A, B, and C, respectively.

Fig. 1-6 Contours of S (root mean square) values in Eq. (1-11) determined by combinations of three uncertain parameters. (a) The horizontal and the vertical axes are depths z_0 in Eq. (1-10) and pore pressure ratios λ on the plate interface, respectively. (b) The horizontal and the vertical axes are pore pressure ratios λ on the plate interface and radioactive heat generations H_0 in the accretionary prism, respectively. (c) The horizontal and the vertical axes are radioactive heat generations H_0 in the accretionary prism and depths z_0 in Eq. (1-10), respectively.

Fig. 1-7 Observed and calculated heat flows along the three profiles. The values of the pore pressure ratio and radioactive heat generation per unit volume in the accretionary prism, and the depth z_0 in Eq. (1-10) were obtained so as to minimize the sum of Eq. (1-11) for the three profiles. Black lines denote the calculated heat flows. Red circles, blue triangles, and green squares denote the observed heat flow of BSR, the land borehole & marine heat probe, and Hi-net observation wells, respectively. Observed data within a one-sided width of 20 km along one side of each profile are plotted. (a) Profile A. (b) Profile B. (c) Profile C.

Fig. 1-8 Vertical cross section of the temperature fields associated with subduction of the PHS plate along the three profiles at 0 Ma. Red lines denote the geometries of the upper and lower surfaces of the PHS plate along the profiles, which also correspond to the prescribed guides. White dots denote the hypocenter distributions of LFEs within a one-sided width of 10 km along of each profile during the period from October 1, 1997 to February 28, 2015. (a) Profile A. (b) Profile B. (c) Profile C.

Fig. 1-9 Spatial distribution of the calculated temperature of the upper surface of the subducting PHS plate. Black lines denote isotherms, and brown lines denote isodepth contours of the upper surface of the PHS plate. Blue lines denote profiles for the numerical simulations. Red lines denote the up-dip (150°C) and down-dip (350°C) limits of the thermal seismogenic zone estimated in our modeling. Red dots denote the distributions of the epicentres of LFEs during the period from October 1, 1997 to February 28, 2015.

Fig. 1-10 Vertical cross section of the calculated water content of hydrous MORB in the oceanic crust for the three profiles. Red small dots denote the hypocenter distributions of LFEs within a one-sided width of 10 km along of each profile during the period from October 1, 1997 to February 28, 2015. (a) Profile A. (b) Profile B. (c) Profile C.

Fig. 1-11 Spatial distributions of the V_p/V_s ratio obtained by seismic tomography for the three profiles. For 3-D seismic wave velocity data beneath the Japanese Islands, we used data provided by Matsubara and Obara (2011). Red dots denote the hypocenter distributions of LFEs within a one-sided width of 10 km along each profile during the period from October 1, 1997 to February 28, 2015. (a) Profile A. (b) Profile B. (c) Profile C.

Fig. 1-12 Focal mechanisms of earthquakes which occurred near the plate interface projected on the lower hemisphere by equal-area projection in central Japan. We used F-net observation data provided by the National Research Institute for Earth Science and Disaster Prevention (NIED) during the period from October 1, 1997 to February 28, 2015. We plotted focal mechanisms whose moment magnitude is greater than 3.0. (a) Spatial distribution of focal mechanisms in the model domain. Green line denotes a profile set to calculate Eqs. (1-15) and (16). (b) Vertical cross section of the upper surface of the PHS plate along green line (Fig. 1-12 (a)). Focal mechanisms projected on the lower hemisphere within a one-sided width of 30 km along the profile are plotted.

Part Ⅱ

Fig. 2-1 Tectonic map of the Tokai district, central Japan. Black lines with arrow heads denote plate boundaries. (a) Blue lines represent isodepth contours of the upper surface of the subducting PHS plate (in km) (Kodaira et al., 2004; Nakajima and Hasegawa, 2007; Hirose et al., 2008; Kato et al., 2010). Yellow lines denote three profiles for our 2-D numerical simulations of temperature and mantle flow. Surrounded region by the black line denotes the Tokai SSE region where the cumulative slip rate during the period from January 1, 2000 to November 30, 2002 exceeds 10 cm (Miyazaki et al. 2006). Red and green

arrows denote plate motion of the PHS plate with respect to the Eurasian and the Amurian plates, respectively (Demets et al. 2010). Red dots denote epicenter distribution of LFEs determined by the Japan Meteorological Agency (JMA) during the period from October 1, 1997 to February 28, 2015. (b) Tectonic map in and around the Japanese Islands. The study area is surrounded by the green lines. The dashed lines is the rough location of the Kinan Seamount Chain. AM, NA, PAC, and PHS represent the Amurian plate, the North American plate, the Pacific plate, and the Philippine Sea plate, respectively.

Fig. 2-2 Schematic figure of the 2D box-type thermal convection model used in this study. The red and blue lines denote the region where the frictional heating and thin conductive layer on the plate boundary were assigned, respectively.

Fig. 2-3 Contours of S (root mean square) values in Eq. (1-11) determined by combinations of two uncertain parameters of pore pressure ratio λ and the depth $z_0^{'}$ in Eq. (1-10).

Fig. 2-4 Observed and calculated heat flows along the three profiles at 0 Ma in Fig. 1(a). Blue triangles, red circles, and green squares denote observed heat flows measured by land borehole& marine heat probes, BSRs, and Hi-net observation wells, respectively. Observed data within one-sided width of 20 km along each profile are plotted. Thick black lines denote the calculated heat flows. (a) Profile A. (b) Profile B. (c) Profile C.

Fig. 2-5 Vertical cross section of the temperature fields associated with subduction of the PHS plate along the three profiles at 0 Ma. Red lines denote the geometries of the upper and lower surfaces of the PHS plate along the profiles, which also correspond to the prescribed guides. Green lines represent the region where the Tokai SSE occurred. White dots denote the hypocenter distributions of LFEs within a one-sided width of 20 km along each profile during the period from October 1, 1997 to February 28, 2015. (a) Profile A. (b) Profile B. (c) Profile C.

Fig. 2-6 Smoothed spatial distribution of the calculated temperature of the upper surface

of the subducting PHS plate. Black solid lines and black dashed lines denote isotherms (in °C) and plate boundaries, respectively. The two red thick lines are isotherms of 150 °C and 350 °C. Brown lines denote isodepth contours (in km) of the upper surface of the PHS plate. Blue lines denote profiles for the 2D numerical simulations of temperature and mantle flow. Red dots denote epicenter distributions of LFEs.

Fig. 2-7 Spatial distributions of the calculated water content of hydrous MORB in the oceanic crust in the vertical cross sections at 0 Ma. Red solid lines represent the region where the Tokai SSE occurred. Red dots denote hypocenter distributions of LFEs. (a) Profile A. (b) Profile B. (c) Profile C.

Fig. 2-8 Spatial distributions of the V_p/V_s ratio obtained by seismic tomography. For 3D seismic wave velocity data beneath the Japanese islands, we used data provided by Matsubara and Obara (2011). Black solid lines denote the upper and lower surfaces of the PHS plate, and the dashed line is the lower surface of the oceanic crust. Red solid lines represent the region where the Tokai SSE occurred. Red dots denote hypocenter distributions of LFEs. (a) Profile A. (b) Profile B. (c) Profile C.

Part Ⅲ

Fig. 3-1 Tectonic map of Mexico. Black dashed lines denote plate boundaries. Blue lines represent isodepth contours of the upper surface of the subducting Cocos plate (in km) obtained by Pardo and Suarez (1995), Pérez-Campos et al. (2008), Yang et al. (2009), Melgar and Pérez-Campos (2011). Purple and green shaded regions denote the Guerrero seismic gap and the Trans-Mexican Volcanic Belt (TMVB), respectively. Yellow star denotes the epicenter of the 1985 Michoacan earthquake. Red and green arrows denote plate motion vectors of the Cocos plate and the Rivera plate with respect to the North American plate, respectively (Demets et al., 2010). Red circles denote station distributions of MASE project. Surrounded area by yellow shaded line denotes the model region. Light blue contours denote aftershock distributions of the past megathrust earthquakes. Black contour lines denote the cumulative amount of slip of the last three SSEs, which occurred in 2001-2002, 2006, and 2009-2010 (Radiguet et al., 2012). Contour interval is 10cm. Green solid triangles denote

epicenters of NVTs.

Fig. 3-2 Schematic figure of the 3-D thermal convection model used in this study. Green and black letters denote boundary conditions for temperature and flow fieldsrespectively.

Fig. 3-3 Calculated results for the standard model. (a) Calculated interpolate temperature.(b) Calculated flow fields in the mantle wedge. Color of arrows represents depth. Color of the oceanic plate represents temperature. (c) Calculated dehydrated water content within the subducting plate. (d) Calculated heat flow distributions to be compared with those of Curie point depths (Manea and Manea, 2011a).

Fig. 3-4 Calculated results for the model when we only varied the age of the Cocos plate at the Middle American Trench from 15 Myr of the standard model to 30 Myr. (a) Calculated interplate temperature. (b) Calculated flow fields in the mantle wedge. Color of arrows represents depth. Color of the oceanic plate represents temperature.(c) Calculated dehydrated water content within the subducting plate. (d) Calculated heat flow distributions to be compared with those of Curie point depths (Manea and Manea, 2011a).

Fig. 3-5 Calculated results for the model when we only varied pore pressure ratio on the plate interface from 1.00 of the standard model to 0.95. (a) Calculated interplate temperature. (b) Calculated flow fields in the mantle wedge. Color of arrows represents depth. Color of the oceanic plate represents temperature. (c) Calculated dehydrated water content within the subducting plate. (d) Calculated heat flow distributions to be compared with those of Curie depths (Manea and Manea, 2011a).

Fig. 3-6 Calculated results for the model when we only varied continental crust thickness from 32 km of the standard model to 50 km. (a) Calculated interplate temperature. (b) Calculated flow fields in the mantle wedge. Color of arrows represents depth. Color of the oceanic plate represents temperature. (c) Calculated dehydrated water content within the subducting plate. (d) Calculated heat flow distributions to be compared with those of Curie depths (Manea and Manea, 2011a).

Fig. 3-7 Calculated results for the model when we varied subducting velocity of the Cocos plate for each grid to be half comparing with the standard model. (a) Calculated interplate temperature. (b) Calculated flow fields in the mantle wedge. Color of arrows represents depth. Color of the oceanic plate represents temperature. (c) Calculated dehydrated water content within the subducting plate. (d) Calculated heat flow distributions to be compared with those of Curie depths (Manea and Manea, 2011a).

Fig. 3-8 Contours of S values in Eq. (3-12) determined by combinations of two predominant parameters for calculated heat flows of pore pressure ratio and the thickness of the continental crust.

Fig. 3-9 Observed and calculated heat flows. Red lines denote isodepth contour lines. Blue line represents the location of Trans-Mexican Volcanic Belt (TMVB). (a) Observed heat flow data estimated from Curie point depths (Manea and Manea, 2011a). (b) Calculated heat flow of the most suitable model obtained in section 4-2. Heat flow is calculated, using temperature gradient between the surface and Curie point depths.

Fig. 3-10 Observed and calculated heat flows. Triangles denote observed heat flow data of Global Heat Flow Database (GHFD) (Jessop et al., 1976). Contours denote calculated heat flow for the most suitable model. Heat flow is calculated, using temperature gradient between the surface and depth of 5 km. Red lines denote isodepth contour lines. Blue line represents the location of Trans-Mexican Volcanic Belt (TMVB).

Fig. 3-11 Calculated interplate temperatures for the most suitable model. Surrounded regions by light blue lines denote rapture areas of the past megathrust earthquakes. Light blue contours denote aftershock distributions of the past megathrust earthquakes. Black contour lines denote the cumulative amount of slip of the last three SSEs, which occurred in 2001-2002, 2006, and 2009-2010 (Radiguet et al., 2012). Contour interval is 10 cm. Yellow solid squares denote epicenters of NVTs. Red solid squares denote volcanoes.

Fig. 3-12 Calculated water content and dehydrated water content from the subducting

Cocos plate. (a) Calculated water content distribution of MORB at the plate boundary as viewed from －z direction of the model. Light blue contours denote aftershock distributions of the past megathrust earthquakes. Black contour lines denote the cumulative amount of slip of the last three SSEs, which occurred in 2001-2002, 2006, and 2009-2010 (Radiguet et al., 2012). Contour interval is 10 cm. Blue solid squares denote epicenters of NVTs. Red solid squares denote volcanoes. (b) Bird's-eye view of dehydrated water content distribution as viewed from －x direction of the model.